Mechanical Metamaterials with Negative Extensibility: Nonlinear Analysis and Phase Diagram Calculation

by

John T. Klein
B.A. (University of Colorado Boulder) 2013

Thesis submitted in partial fulfillment of the requirements
for the degree of Master of Science in Materials Engineering
in the Graduate College of the
University of Illinois at Chicago, 2017

Chicago, Illinois

Defense Committee:
Eduard Karpov, PhD, Chair and Advisor
Craig Foster, PhD
Michael McNallan, PhD
Mustafa Mahamid, PhD
Sheng-Wei Chi, PhD

To my mom,

Jenny,

... and our dog (Nelly)

ACKNOWLEDGMENTS

I wish to thank all the wonderful professors I have had at UIC.

TABLE OF CONTENTS

TABLE OF CONTENTS (Continued)

CHAPTER **PAGE**

LIST OF TABLES

LIST OF FIGURES

LIST OF ABBREVIATIONS

MS	monostable
SE	superelastic
SP	superplastic
NESE	negative extensibility of the superelastic type
NESP	negative extensibility of the superplastic type
MEMS	microelectromechanical system
SMA	shape memory alloy

SUMMARY

Metamaterials exhibit properties not normally observed in nature. Properties are derived from an engineered internal structure rather than atomic composition. Major classes of metamaterials are electromagnetic, acoustic and mechanical. Mechanical metamaterials are characterized by their unnatural elastic properties. The shear modulus, elastic modulus, bulk modulus and Poisson's ratio are measures of rigidity, stiffness, inverse of the compressibility and ratio of longitudinal strain to contractile strain. Mechanical metamaterials may take on a negative value for one or more of these constants. Analysis is performed under quasistatic loading conditions.

The mechanical property under investigation is negative extensibility. A five element unit-cell structure is able to contract against the line of increasing tension. If uniaxial stiffness were to be measured during this contraction, the structure would appear to possess a negative stiffness. More accurately, it would be a negative 'incremental' stiffness since the slope of the stress-strain curve becomes negative after the load is applied. Negative extensibility is contrasted with other mechanical phenomena including negative compressibility, negative Poisson's ratio, stretch-densification and St.-Venant edge effect reversal.

The unit-cell structure is bistable. There exists two valid solutions of equilibrium for a given applied load. During a load-unload cycle, the response is hysteretic. The potential or strain energy function of the unit-cell is highly nonlinear due to geometry. Several distinct types of mechanical responses are possible depending on the choice of member stiffness and dimensions. After the potential is put into dimensionless form, a phase diagram is calculated. The phase

diagram is a function of dimensionless system parameters that represent the geometry and stiffness of elements. Regions of the diagram are associated with a distinct mechanical response achieved during a load-unload cycle. Boundary lines are the onset of a particular mechanical response.

Energy methods used in computational thermodynamics for the calculation of microstructural phase diagrams are re-purposed in order to map the mechanical response of the unit-cell structure. The critical boundaries that divide monostability from bistability are determined using a set of constraints, which are informed by the principles of catastrophe theory. Even within the bistable region it is possible to differentiate mathematically the nature of the hysteretic response. Of most significance is the existence of negative extensibility of the superelastic-type (NESE). The response is characterized by a 'pinched' hysteresis loop. The structure contracts intermittently against the applied external tension. It does negative work as load is applied. This is a condensation reaction.

The boundary lines delineating the NESE response are discussed in great detail. Conditions are developed for computing the intersections of boundary lines on the phase diagram. Analogous to thermodynamics, there exist singular 'triple points' where the system simultaneously satisfies conditions for three different states of mechanical equilibrium. The discussion ends with a brief presentation of how the unit-cell can be arranged into a periodic array. Periodic boundary conditions are developed that could be used to approximate the response of a larger system. Fabrication of a periodic structure designed to contract at a critically applied load remains an open question. Viability of the phenomenon in practice is evaluated.

CHAPTER 1

INTRODUCTION

In 1967, Russian physicist Victor Veselago showed analytically that a medium with simultaneously negative magnetic permeability μ and electric permittivity ε has a negative index of refraction [1]. Although theoretically possible by the laws of physics, at that time no natural or engineered material had been observed with this exotic electromagnetic property. It would not be until three decades later that Sir John Pendry laid the groundwork for synthesis of materials with negative permittivity [2] and permeability [3] by performing computations on low-frequency diffraction in composites made of metallic rods and copper split-ring resonators. Shortly thereafter, the optical phenomenon was realized experimentally when a team of American physicists fabricated an interlocking lattice of copper split-ring resonators and copper wire strips, which exhibited simultaneous negative permittivity and permeability in the microwave range [4]. Materials with a negative refractive index show a reversal of many physical properties such as Snell's Law and the Doppler effect [5, 6]. This new category of material was coined as a "metamaterial,"—it possesses properties not normally observed in nature.

1.1 Electromagnetic metamaterials and the metamaterials paradigm

The first metamaterials discovered were electromagnetic. Applications being investigated include superlensing—the ability to resolve light below the diffraction limit [7], an "invisibility cloak" [8–10], antennae and wireless telecommunication devices [11–13], sensors [14] and

photo-voltaic and catalytic cells [15]. Metamaterials represent not only a new class of materials extending the design space to negative ranges for material constants, but perhaps more importantly, they represents a new framework to conceptualize about materials. Metamaterials are quite diverse with acoustic and mechanical being the other two major types of metamaterials. Engineered metamaterials may gain their properties from an array of repeating small-scale units or "elements" embedded in a larger matrix [16, 17]. In the case of double negative electromagnetic metamaterials, the scale of these structural units is small relative to wavelength of incident radiation. The constituent materials themselves do not have the same properties as the composite metamaterial. It is the engineered internal structure rather than the chemical composition that is responsible for an effective negative value for a physical property. In the literature this is referred to as an "effective medium description" [18]. In other words, the macroscopic response of the mixture is distinct from those of the ingredients [19]. However, this distinction is not so clear when considering that for certain chemical compounds hierarchical order starting from the level of the microstructure and down to the level of the atomic structure are factors contributing to metamaterial properties, especially in the domain of mechanical metamaterials [20, 21].

1.2 Acoustic metamaterials

Properties of acoustic metamaterials, including an effective negative compressibility (inverse of the bulk modulus K) and effective negative dynamic mass density, are based on the dynamics of sonic wave propagation through the medium [22, 23]. Parallels between acoustics and electromagnetism are readily seen when comparing the Helmholtz equation for acoustic pressure

to the electromagnetic wave equation [24]. Double negativity in the dynamic bulk modulus and dynamic density is the acoustic analogue of double negativity in the permeability and permittivity in electromagnetism [25]. The metamaterials paradigm is the same for acoustics as it is for electromagnetism in that an unconventional macroscopic response such as effective negative refraction is achieved through the periodicity of locally resonant elements, known as Helmholtz resonators [26]. However, other types of composite acoustic metamaterials do not make use of inertial resonance effects to achieve a negative bulk modulus; rather, this property as well as other phenomena such as extreme damping [27] and extreme stiffness [28] are the result of negative stiffness inclusions constrained within a viscoelastic matrix. The observation of negative effective material properties is permissible by the laws of thermodynamics because the system either is being dynamically excited, exists in a thermodynamically open state, or only one constituent of the composite material bears this property [29, 30]. Potential applications of acoustic metamaterials include acoustic lensing—focusing of acoustic waves below the diffraction limit for ultra-sound imaging [31, 32], acoustic cloaking—the ability to hide objects from sound [33, 34], acoustic shielding (a perfect mirror)—total reflection of sound waves over specific frequency bands [35, 36] and earthquake engineering [37]. Like electromagnetic metamaterials, these effects act over a specific frequency range, stopband or band gap.

1.3 Mechanical metamaterials

Mechanical and structural metamaterials, often analyzed under quasistatic conditions, encompass a range of materials with non-natural elastic constants such as the shear modulus G, elastic modulus E, bulk modulus K and Poisson's ratio ν, which respectively, are measures of

the rigidity, stiffness, inverse of the compressibility and ratio of contractile strain to longitudinal strain [38]. Mechanical metamaterials can be characterized by an artificially designed structure, which is often made up of simple microstructural spring and bar elements [39, 40]. Properties are derived from the deliberate structuring of elements, and thus, these properties are distinct from those of the bulk materials that comprise the structure [41]. Structures may be fabricated using rapid prototyping techniques such as 3D printing [42]. For some mechanical metamaterials, the chemical makeup of the bulk material is at least in part responsible for an unusual property—e.g., black phosphorus as well as certain plastically deformed polymeric and metallic foams. These highly anisotropic materials possess a negative Poisson's ratio and are known as auxetic materials [43, 44]. Auxetic foams exhibit unit-cell geometry that is idealized as a symmetrically collapsed 24-sided polyhedron, which facilitates lateral expansion when stretched uni-axially [45].

Ultimately, it is the structure that governs the mechanical response. The interesting mechanical properties stem from the fact that there are a finite number degrees of freedom in the system constraining the allowed movements. The aggregate effect of many unit-cells together leads to strange, unnatural effects such as in the case of pentamode metamaterials, which are defined by an extremely large bulk modulus to shear modulus ratio [46]. Pentamode metamaterials behave much like a fluid in that they mold to fit the shape of objects. The solid lattice structure shears or deforms easily. At the same time the lattice is extremely hard to compress [47].

A common motif encountered in metamaterials research is that properties are 'tunable.' For instance, the permeability of light through electromagnetic metamaterials can be altered

such that over the same band gap the material may switch between reflecting, transmitting and absorbing light—i.e., the response can be tuned to a specific frequency [48]. Mechanical metamaterials may have multiple stable states of equilibrium. Here, tuning capabilities are achieved during the process of state switching, which often occurs by reconfiguration of the lattice or unit-cell geometry [49]. Origami-based mechanical metamaterials serve as a prime example. The Miura-ori tessellation is the basic pattern that is used to mesh a flat sheet into creases [50]. Because a single Miura fold can be reversibly switched between two states—one soft and one stiff—a sheet with many creases can be re-folded into an entirely new three-dimensional shape with a totally different set of mechanical properties than the original configuration [51]. Related to the concept of programmable matter, physical properties of Origami-inspired metamaterials are said to be dynamically re-configurable [52,53]. The defect structure in Origami, analogous to a crystal lattice, plays a fundamental role in controlling physical properties [54]. Computational Origami borrows the terms vacancy, dislocation and grain boundary to pertain to specific features in the crease pattern that alter how the paper can be folded [55]. Applications of Origami-based metamaterials include self-folding polymeric systems [56], self-folding robotics systems [57] and soft robotics applications such as pneumatic and biomorphic actuators [58, 59].

CHAPTER 2

BISTABLE SYSTEMS

Before presenting the metamaterial property of negative extensibility, the fundamental concept of mechanical bistability must be discussed in greater depth. In mechanics, bistability occurs when the total potential or strain energy function of the system generates two valid equilibrium configurations for a single loading condition. Oftentimes, during loading there exists a critical force where the structure jumps discontinuously from one state to another. For instance, a beam may buckle, a switch may flip or a truss may snap-through. In the literature prominent examples of mechanical bistability include the von Mises truss [60, 61], machinery in microelectromechanical systems (MEMS) [62–64], piezoelectric oscillators and switches [65, 66], shape memory alloys and thin film actuators [67, 68].

2.1 Two-bar truss

A single-degree-of-freedom two-bar truss coupled to a spring shown in Figure 1 is a model system used to illustrate several fundamental concepts regarding bistability. A quasistatic analysis is performed in order to generate a force-response curve, which plots the equilibrium displacement of the truss u as a function of the applied load F. To begin the analysis, a balance of energy over the system is performed where the stored energy U in the two bars k_1 and spring k_2 are subtracted from the energy of the external load V.

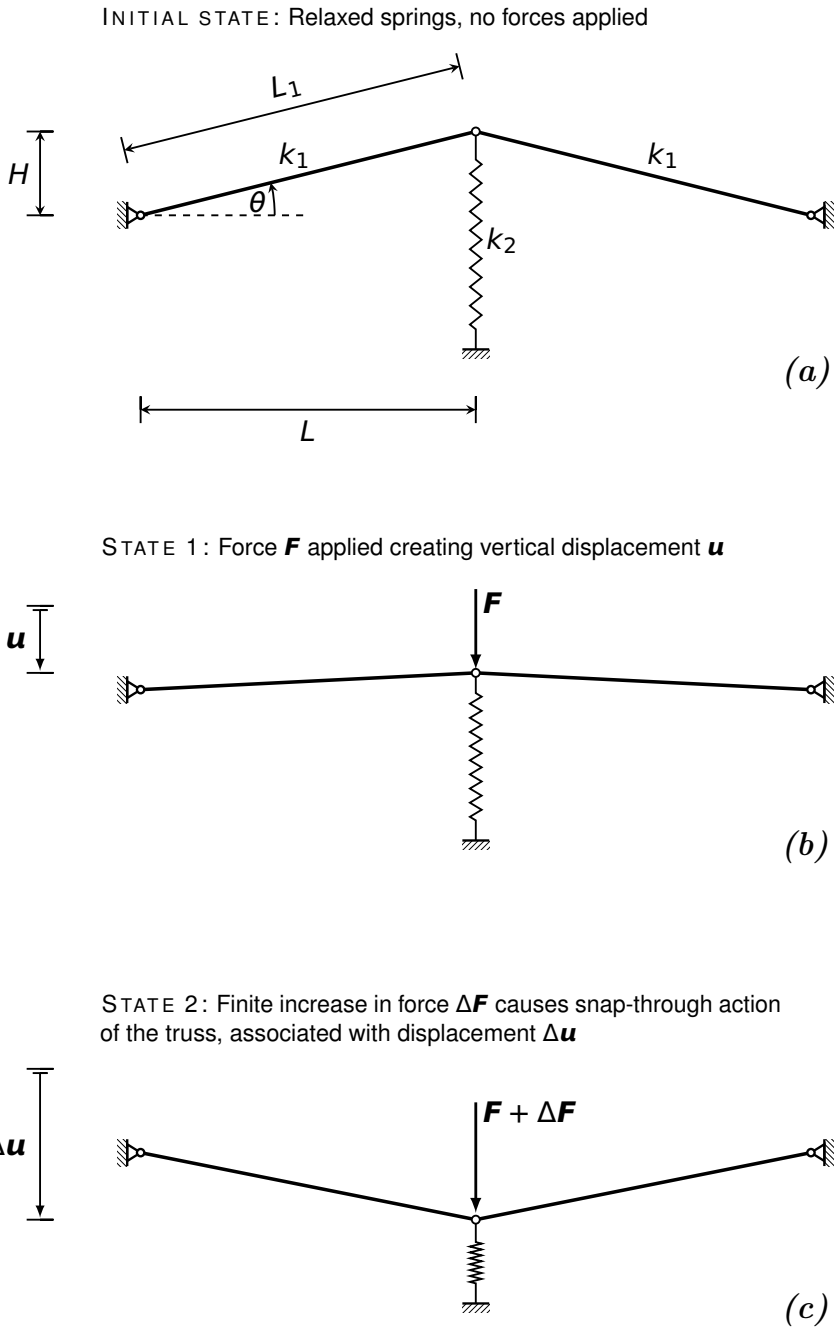

Figure 1: Two-bar truss coupled to a spring. (a): Relaxed bars and spring are initially in state 1. (b): Application of force $\boldsymbol{F}$ at the midpoint causes displacement $\boldsymbol{u}$ while still remaining in state 1. (c): At a critical force the structure 'snaps-through' to state 2 reaching a new equilibrium after an intermittent displacement $\Delta\boldsymbol{u}$.

Balance of energy:

$$\Pi = U - V \tag{2.1}$$

$$= \frac{1}{2}k_1(\Delta l_1)^2 + \frac{1}{2}k_1(\Delta l_1)^2 + \frac{1}{2}(\Delta l_2)^2 - Fu \tag{2.2}$$

$$= k_1\left(\sqrt{L^2 + (H-u)^2} - \sqrt{L^2 + H^2}\right)^2 + \frac{1}{2}k_2u^2 - Fu \tag{2.3}$$

Equilibrium conditions require that the first derivative of the potential with respect to the degree of freedom u must be equal to zero

$$\frac{d\Pi}{du} = -F + k_2u - \frac{2k_1(H-u)\left(\sqrt{(L^2 + H - u)^2} - \sqrt{L^2 + H^2}\right)}{\sqrt{L^2 + (H-u)^2}} = 0 \tag{2.4}$$

Because the system has just one degree of freedom, the displacement u, an analytic solution for the force F as a function of u is possible by placing the force F on the other side of the equilibrium equation (Equation 2.4). Alternatively, the displacement u can be solved as function of F numerically by a Newton-Raphson approach. In this case, F is used as a running variable and the displacement u is solved for at discrete values of F. To get a smooth response curve as force is increased, a small enough step size ΔF is required.

For this simple truss system, there exists only three qualitatively distinct types of force-response curves, each of which are graphed in Figure 2:

1. monostability (MS)
2. superelasticity (SE)
3. superplasticity (SP)

Although the material laws are all linear elastic, the strain energy function (Equation 2.3) is highly nonlinear as a consequence of the geometry. Because of this nonlinearity, for certain

combinations of element stiffnesses and dimensions it is possible for the solution to bifurcate or split such that two stable states of equilibrium exist for a single loading condition. The result is hysteretic bistability. Using principles from catastrophe theory[1] it is possible to define the set of all points corresponding to the onset of bistability. A hysteresis loop—i.e., bistability, is observed for the superelastic (SE) and superplastic (SP) response curves. The monostable (MS) response, although nonlinear, is a smooth, continuous expansion and contraction of the elastic members during load-unload cycles.

During loading, the surroundings are doing work onto the system. Compression of the bars and spring results in the absorption of strain energy linearly proportional to the change in length. The displacement is in the direction of the applied force so work is defined as positive $W_{load} \equiv +$. During unloading, the system does work onto the surroundings as it releases stored strain energy. $W_{unload} \equiv -$ since the displacement opposes the direction an applied force. For the superelastic hysteresis of the truss in Figure 2, integrating over the cycle reveals that the net work is positive $W_{cycle} \equiv +$. Work is $F \cdot du$ so that the x-axis (force F) is integrated over the y-axis (displacement u). The energy absorbed during loading exceeds the energy released during unloading. Viscoelastic materials such as shape memory alloys show qualitatively a similar hysteresis effect [69]. The stress-strain curve in loading is located above the unload curve—i.e., under forward loading a greater applied stress is required to reach the same level of deformation during unloading. The net work in a cycle is positive. Most of the energy absorbed

---

[1]Catastrophe theory is a branch of applied math derived from topology that studies how the shape of smooth surfaces of equilibrium are affected when sudden, discontinuous catastrophic singularities occur.

in the cycle will be lost primarily due to heat. Heat loss occurs due to friction between slip planes as a material deforms, which is called hysteretic or material damping [70].

2.2 Superelasticity

Superelasticity is the ability of a structure to accommodate large applied strains and recover to its original configuration when the load is removed. The superelastic response of the truss system, shown in blue in Figure 2, is characterized by a forward phase transformation $1 \rightarrow 2$ during loading and a reverse transformation $2 \rightarrow 1$ during unloading. The critical force for the forward transformation marks the onset of destabilization and snap-through action of the truss as it re-equilibrates to a new configuration. Using Newton-Raphson to solve for the equilibrium displacement reveals a vertical discontinuity in the strain. The forward superelastic transformation is accompanied by the absorption of energy by the system, raising its internal energy. Thermodynamically, this is comparable to a vaporization reaction. During load removal, a reverse transformation $2 \rightarrow 1$ will occur but at a lower critical force than the forward transformation. The structure destabilizes and re-equilibrates at a lower strain corresponding to its original state 1. The reverse superelastic reaction is analogous to condensation; energy is released from the system to the surroundings. During cycles of load-unload, the energy dissipated in the process is proportional to the area enclosed by the hysteresis loop [71].

Shape memory alloys such as nickel titanium were the first discovered materials capable of undergoing large, reversible deformation [72]. At a critically applied tension, these metals expand in volume as a result of a stress-induced martensitic phase transformation [73]. Provided temperature is great enough, when the load is removed the inverse reaction proceeds, thereby

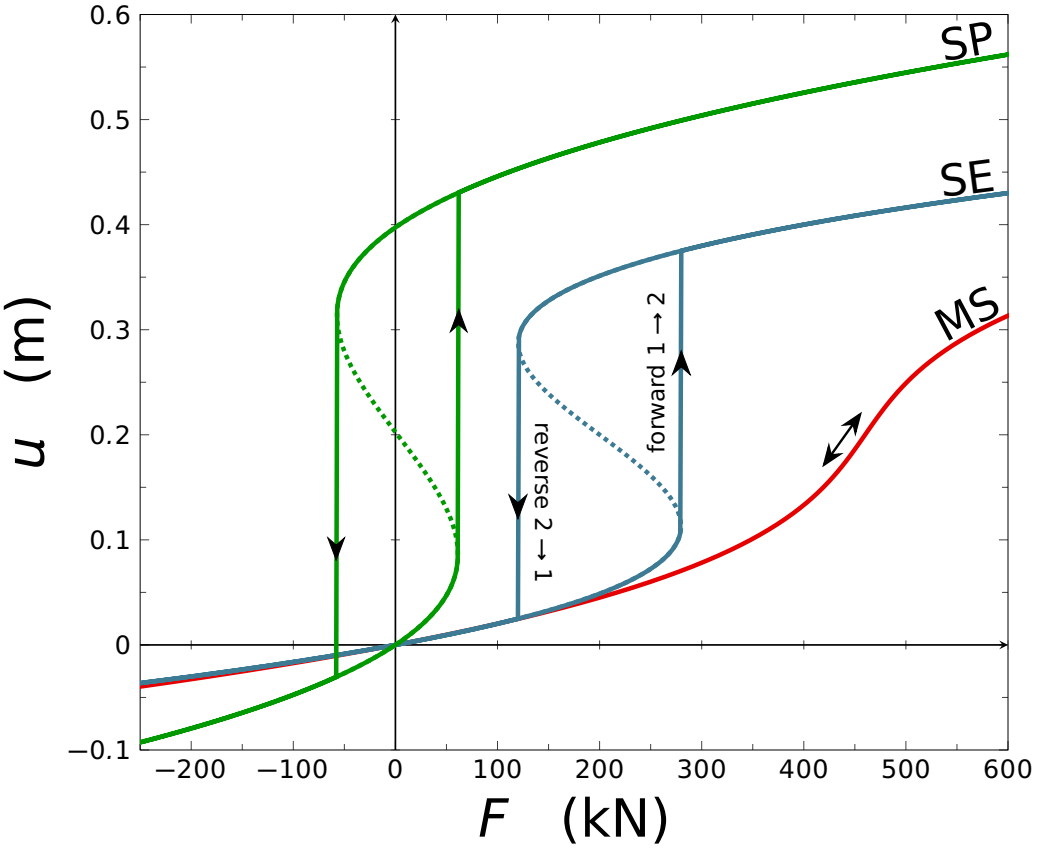

Figure 2: Three classes of force-response curve for the single-degree-of-freedom two-bar truss coupled to a spring. The type of response depends on the stiffness of the bars k_1 and spring k_2 and initial dimensions L and H. Curves are generated using $L = 1.0$ m, $H = 0.2$ m. Monostable (MS) response (red), shown for $k_1 = 4\text{E}4$, $k_2 = 2.3\text{E}3$ kN/m. Superelastic (SE) response (blue), shown for $k_1 = 1\text{E}4$, $k_2 = 2.0\text{E}3$ kN/m. Superplastic (SP) response (green), shown for $k_1 = 2\text{E}4$, $k_2 = 1$ kN/m. Under normal loading conditions the 'S' shaped inner curve, which comprises the analytical solution $F(u)$ will not be accessed.

restoring the alloy to its original position. Alloys with stress-induced transformations are hysteretic, a defining feature of superelasticity. Alternatively, if the metals are stressed beyond a certain threshold or the temperature is too low, during load removal the inverse reaction may not proceeded to completion. The larger volume martensitic phase persists. In this state, the alloys are referred to as 'superplastic' since during loading the material underwent the forward (expansion) reaction but during unload the reverse (contraction) reaction either failed to occur or failed to proceed to completion. However, if shape memory alloys—now in the superplastic state—are heated then the inverse transformation is driven to completion and the initial shape is restored. The shape memory effect is the recovery of superplastic metals with heat. Temperature and applied stress play comparable roles in driving the transformation [74]. The austenitic phase is stable at high temperatures and low stresses. The martensitic phase is stable at lower temperatures and higher stresses. Due to their extreme ductility, light weight and high strength shape memory alloys see applications in the aerospace industry, often forming complex, irregular shapes [75].

2.3 Superplasticity

As discussed, superplasticity occurs when a structure accommodates large applied strains and remains in this highly deformed state after load removal. Superplastic materials usually accommodate strains well beyond their normal breaking point. For some materials tensile elongation exceeds 2000 % [76]. Large flow stresses and the shape memory effect are two important features of superplastic shape memory alloys [77]. Superplasticity is observed in fine-grained metal and ceramic systems [78, 79]. Fine-grained and nanocrystalline structures

are amenable to superplasticity owing to the mechanism of plastic deformation, described as grain boundary-diffusion, -sliding and -rotation [80]. Cold-rolled nano-crystalline copper was elongated by 5100 % whereas coarse grained copper usually breaks around 800 % [81]. The term 'superplastic extensibility' is used to describe the extreme elongation of nanocrystalline metals [82].

The superplastic response of the two-bar truss, depicted as the green curve in Figure 2, reveals a hysteresis loop. Like the superelastic response, during loading at a critical force there is an abrupt forward $1 \rightarrow 2$ phase transformation. However, the main difference between superelasticity and superplasticity is the location of critical force for the reverse transformation $2 \rightarrow 1$. When the load is removed from the superplastic truss it remains plastically deformed in state 2. Under tension, the structure in state 2 would appear to have a different stiffness than state 1. For this reason, the two states are considered structural polymorphs. In order to restore the truss to its original configuration the load must be applied in the opposite (negative) direction. Only then will the structure be able to overcome an energy barrier, which allows it to snap back to its original state.

2.4 Cusp catastrophe

Catastrophe theory is particularly useful in understanding systems that undergo discrete, non-smooth transitions such as the transition between monostability and bistability in a plane truss when element stiffnesses, dimensions and load are altered [83]. The simplest 'elementary catastrophe' is the fold catastrophe, which is graphed in Figure 3 (a) and the underlying function shown in Table 1. In physics, the curve represents an energy minimum—i.e., solutions of static

TABLE 1: Seven elementary catastrophes

	Catastophe	Control dimensions	Behavior dimensions	Function	First derivative
Cuspoids	Fold	1	1	$\frac{1}{3}x^3 - ax$	$x^2 - a$
	Cusp	2	1	$\frac{1}{4}x^4 - ax - \frac{1}{2} - bx^2$	$x^3 - a - bx$
	Swallotail	3	1	$\frac{1}{5}x^5 - ax - \frac{1}{2}bx^2 - \frac{1}{3}cx^3$	$x^4 - a - bx - cx^2$
	Butterfly	4	1	$\frac{1}{6}x^6 - ax - \frac{1}{2}bx^2 - \frac{1}{3}cx^3 - \frac{1}{4}dx^4$	$x^5 - a - bx - cx^2 - dx^3$
Umbilics	Hyperbolic	3	2	$x^3 + y^3 + ax + by + cxy$	$3x^2 + a + cy$ $3y^2 + b + cx$
	Elliptic	3	2	$x^3 - xy^2 + ax + by + cx^2 + cy^2$	$3x^2 - y^2 + a + 2cx$ $-2xy + b + 2cy$
	Parabolic	4	2	$x^2y + y^4 + ax + by + cx^2 + dy^2$	$2xy + a + 2cx$ $x^2 + 4y^3 + b + 2dy$

equilibrium. The 'behavior' axis is a dependent variable. The behavior is a function of the control parameter a. If the dependent variable is position x, then the control parameter may be the input force. The fold catastrophe is defined by a singular point where the two branches meet. This point is the onset of solution splitting.

The fold catastrophe is a transversal projection of the cusp catastrophe, graphed in Figure 3 (b) and (c) with the function in Table 1. The cusp catastrophe is a three-dimensional figure with two control parameters a and b and a third dimension for the behavior axis. The two control

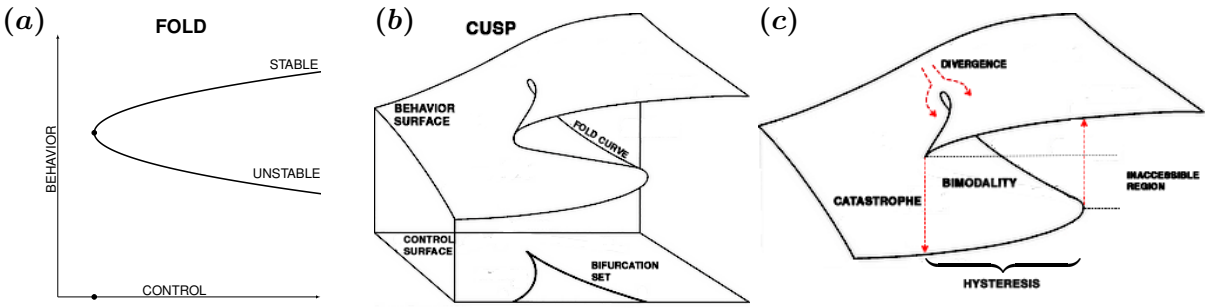

Figure 3: (a): Fold catastrophe, (b): Cusp catastrophe, (c): Five properties that distinguish systems modeled using the cusp catastrophe. Image (a) is original while images (b) and (c) are modified from a Public Domain image from the Wikipedia Commons.

parameters are two independent variables or inputs into the system. The distinctive shape of a cusp—two lines meeting sharply at a point, is projected onto the control surface in Figure 3 (b). The set of control parameters that comprise the cusp is referred to as the 'bifurcation set.' The bifurcation set marks the boundary of bimodal, hysteretic behavior. Inside the cusp region, there will be two valid solutions of equilibrium for a single pair of control parameters. Bimodal systems modeled with a cusp catastrophe include the buckling of an Eulerian beam, the transformation from liquid to gas and stick vs. slip modes of dry friction [84, 85].

The cusp catastrophe is characterized by five properties:

1. Bimodality: There are two possible states in the system.
2. Catastrophic jumps: Transitions between two states of equilibrium are sudden and discontinuous.
3. Hysteresis: The location of the transition from the bottom sheet to the top sheet occurs at a different position than the transition from the top sheet to the bottom sheet, an effect called hysteresis.
4. Inaccessible zone: The middle sheet (fold curve) that connects the top and bottom sheets (shown in Figure 3 (b) but omitted in Figure 3 (c)) is the least likely response and often physically inaccessible.
5. Divergence: Prior to the onset of bifurcation, a small perturbation in the system may have a large downstream effect. Depending on the direction of perturbation, the final state may end up on either the top or the bottom sheet.

René Thom, the founder of catastrophe theory, demonstrated that for processes governed by no more than four factors there exists only seven elementary catastrophes [86]. These are presented in Table 1. Higher-dimensional catastrophes cannot be drawn in their entirety. The behavior surfaces and solution splitting regions are often projected as three- and two-dimensional figures. In Chapter 5, an understanding of the basic principles of catastrophe theory will greatly aid the analysis of a two-degree-of-freedom (2 behavior axes) elastic structure whose response is dictated by a total of five independent parameters. The potential function of this system is concave, non-harmonic and consequently highly nonlinear. The ability to compute the location of all cusp singularities—the bifurcation set—is a powerful tool in mapping the response of the system since this is the crucial boundary between monostability and hysteretic bistability. Computation of bifurcation points been successfully applied in different systems including optimizing landing gear [87] and power systems [88], predicting climate transitions [89] and predator-prey relationships [90] and analyzing compressor flow stability [91].

CHAPTER 3

MECHANICAL PROPERTIES AND THEIR REVERSAL

Mechanical metamaterials under certain circumstances see a reversal of the usual mechanical properties typical to most engineering and natural materials. For instance, mechanical metamaterials may experience: (1) a decrease in length along the line of increasing applied tension (negative extensibility), (2) a decrease in hydrostatic stress under volume compression (negative compressibility), (3) a lateral expansion when stretched axially (negative Poisson's ratio), (4) a decrease in volume when stretched axially (stretch-densification) and (5) fast decay of coarse strain fluctuations with distance (reversal of St.-Venant edge effects).

3.1 Negative extensibility

Extensibility will be defined as the change in length ΔL of a material, which occurs along the direction of an increasing applied external force $F + \Delta F$. Normal materials expand in the direction of an applied tension. In contrast, a mechanical metamaterial with a negative extensibility transition will contract at a critical force so as to oppose the direction of an increasing external tension. To be clear, this definition does not take into account how the material deforms transversely or any other volumetric effects. All that is taken into account is the response in the longitudinal direction when a linear force such as a tension is applied. It follows that if the uniaxial stiffness were to be measured during this contraction against an

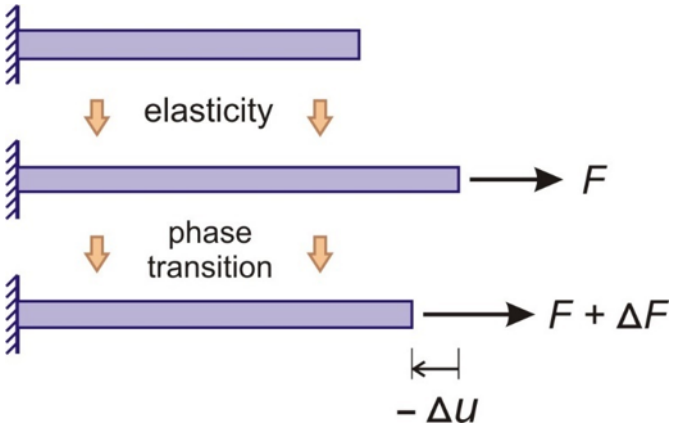

Figure 4: Definition of negative extensibility. At a critically applied load $F+\Delta F$ the structure displaces $-\Delta u$ so as to contract against the line of increasing tension.

applied tensile force $F + \Delta F$, the result would be a negative spring constant k. The definition is written as

$$\text{Extensibility:} \quad \Delta L = \frac{\Delta F}{k} \tag{3.1}$$

A negative extensibility transition is shown in Figure 4.

If the slope of the force-displacement curve shifts negative after the force is applied, it is said to be 'non-monotonic.' The transition from a positive to a negative slope represents a "negative incremental stiffness" [92]. Negative incremental stiffness has been observed in post-buckled rubber tubes and single-cell foam structures constrained under displacement control [93, 94]. Constraint is a necessary condition for these structures to exhibit negative incremental stiffness. When multiple foam cells are tested under uniaxial compression, the constrain becomes insufficient and the effect is no longer observed [94]. Negative extensibility should be distinguished from other effects discussed in the literature including: negative compressibility, negative Poisson's ratio, stretch densification and St.-Venant edge effect reversal.

3.2 Negative compressibility

The isothermal compressibility β quantifies the change in volume of the material in response to a change in hydrostatic pressure

$$\beta = -\frac{1}{V}\frac{\partial V}{\partial p} = \frac{1}{K} \tag{3.2}$$

Normal materials compress axially in all directions in response to an increase in hydrostatic pressure and expand axially in all directions in response to a decrease in hydrostatic pressure, resulting in a positive value for the compressibility [95]. Metamaterials with negative compressibility may see a reversal of this behavior in one or more axial dimensions [96]. The bulk modulus K is the inverse of the compressibility. Therefore, the property of negative compressibility always corresponds to a negative bulk modulus.

Negative incremental bulk modulus is the situation when increasing hydrostatic strain results in a decrease in hydrostatic stress. In an experiment with a type of foam, an applied compressive volumetric strain causes an increase in hydrostatic stress until a point is reached where the hydrostatic stress starts to decrease even though the volume continues to shrink [92]. Over this region the foam possesses a negative bulk modulus and equivalently, a negative compressibility. In this case, the independent variable is the volumetric strain (displacement-controlled) while the dependent variable is the hydrostatic stress.

Negative compressibility is related to and often coincides with a negative elastic modulus or negative stiffness, depending on the context. For instance, certain composite materials when dynamically excited show an effective negative compressibility, which is achieved in part because

of pre-strained, negative stiffness phases that are constrained in a viscoelastic matrix [27, 97]. A unifying property that ties materials with a negative incremental bulk modulus and inclusions with a negative stiffness is that these states are stabilized through surface constraints [28].

Previous work by Lakes and Wojciechowski [98] explored the notion that although thermodynamic considerations require positive compressibility, there exist certain assumptions in this claim that must be examined. At the crux of their argument was that "the continuum has a non-denumerable infinite number of degrees of freedom, while a solid made of atoms has a finite, albeit large, number of degrees of freedom" [98]. Moreover, since atoms are vibrating due to nonzero temperature they experience a degree of freedom which is absent from the continuum. Elasticity theory does allow for negative compressibility, in particular when the object is constrained [43]. However, thermodynamics requires that the strain energy density function be positive definite, which forbids negative compressibility [99]. Motter and Nicolaou [39] similarly explored this notion and concluded that negative compressibility is prohibited in thermodynamically closed systems. If it does occur then the original configuration is necessarily unstable. However, the researchers stated that an implicit assumption of thermodynamics is that changes in force are small and that equilibrium survives this loading, i.e.—a quasistatic process. The researchers concluded that if force changes by a finite amount as in real physical scenarios then it is possible that equilibrium may destabilize leading to a new stable equilibrium. This would permit a negative compressibility transition.

Under conditions of increasing hydrostatic pressure, there are multiple instances of only one axis of a material expanding under increasing hydrostatic pressure while the other two axes be-

have with the usual positive compressibility. The effect is termed negative linear compressibility and occurs in tetragonal networks of beam structures [100], crystal phase materials [101, 102], biological materials [103] and polymeric systems [104]. Even more rare is when changes in hydrostatic pressure induce two perpendicular dimensions of a material to show negative compressibility while the third dimension behaves with the usual positive compressibility. This effect is called negative area compressibility and has been observed in crystal structures [105] and biologic membranes [106]. The most exotic effect—negative compressibility in all axial directions—has been realized in a mechanical metamaterial model, which is able to contract in all directions when subjected to an isotropic tension [39, 40]. An expansion in volume under increasing pressure is achieved through the nonlinear interaction of force potentials between particle constituents [107].

3.3 Negative Poisson's ratio

Poisson's ratio ν is defined as the signed ratio of lateral strain to axial strain along the direction of applied tension

$$\nu = -\frac{\varepsilon_{lateral}}{\varepsilon_{axial}} \tag{3.3}$$

Most materials grow thicker along their cross-section when compressed in a vice and stretch thinner when pulled apart. Materials with a negative Poisson's ratio expand laterally in tension and diminish laterally in compression. The first observed materials with a negative Poisson's ratio were metallic and polymeric foams [20, 43]. Later the phenomenon was seen in anisotropic composites [108], laminates [109], naturally occurring rocks [110], inorganic single crystals [111]

and engineered structures such as micro-porous cellular structures [112]. Before the discovery of this class of material, referred to as auxetics, all known materials exhibited a Poisson's ratio ranging from nearly 0 (no lateral strain change, seen in cork) to nearly 0.5 (perfectly incompressible, seen for rubbery solids). Auxetics comes from the Greek word *auxetos*, meaning "that which may be increased" [113].

For isotropic materials, those without a preferred orientation, thermodynamic arguments regarding stability restrict allowable ranges for Poisson's ratio to be $-1 < \nu < 0.5$. Over this range, both the bulk modulus K and shear modulus G are positive [114]. A Poisson's ratio approaching 0.5 is the situation where the bulk modulus is much greater than the shear modulus, $K >> G$, and the material is nearly incompressible. A Poisson's ratio approaching -1 is the situation where the material is highly compressible but difficult to shear $G >> K$. Auxetic foams and composites are inhomogenous and anisotropic. Additionally, properties are derived from the twisting and bending moments transmitted through fibers and cell ribs with a 'characteristic length' comparable to the micro-cellular structure [115]. These considerations raise doubts on the utility of the continuum theory of elasticity for auxetic materials.

A Poisson's ratio of -0.8 was observed in a copper foam [116] and for highly anisotropic micro-porous polyethylene the Poisson's ratio reached as low as -1.2 in some directions [117]. Poisson's ratio for cubic materials can theoretically range from -1 to 2 although there is no theoretical limit for crystals having less intrinsic symmetry [118]. Few crystals exhibit a negative ν for all directions. Because ν is defined as a 'cross property' with no specific energy coupled to it, it does not have to be positive [98]. Moreover, negative Poisson's effects can be achieved by

structuring a composite material with viscous and elastic components such that the effective response—increasing or decreasing Poisson's ratio with time $\nu(t)$—can be altered dynamically [119].

3.4 Stretch-densification

Using the terminology of Baughman, materials with Poisson's ratio $\nu > 0.5$ in both transverse directions are termed "stretch-densifying" [120]. The change in volume due to the thinning of the cross-section, which occurs over two transversal dimensions, outweighs the change in volume due to the elongation thereby increasing the density of the material. Cellular structures including hexagonal honeycombs are known to exhibit a Poisson's ratio of 1 in certain directions [121]. Stretch-densification is realized in certain foams after they are plastically stretched along one axis. This leads to an enhanced axial, anisotropic stiffness and an increased Poisson's ratio $\nu > 1$ [122]. The processing here is different from the processing required to achieve foams with a negative Poisson's ratio. For negative Poisson's ratio foams, permanent triaxial compression produces a 're-entrant' structure where the cell is transformed from a convex polyhedral shape to a concave shape [43].

The above definition of stretch-densification based on a Poisson's ratio $\nu > 0.5$ is not general enough since there exist a class of extremely rare crystalline and polymeric materials that when stretched exhibit a negative Poisson's ratio and a simultaneous increase in density [96]. The increase in density occurs when these solids are stretched along an axis of negative linear compressibility [123]. When compressed hydrostatically, these materials stretch along one axis and see an increase in surface area—thereby exhibiting negative linear compressibility.

When subjected to tension along this axis, a considerable lateral expansion occurs (associated with a negative Poisson's ratio) as well as a simultaneous lateral inward shift of a different plane of atoms causing an increase in an density (corresponding to a positive Poisson's ratio) [118]. Baughman states that the density increase is made thermodynamically possible precisely as a consequence of the negative Poisson's ratio. The relationship between negative ν and stretch-densification is reconciled through the extreme anisotropy of cubic phase crystals and micro-porous polymers. In one transversal direction they show the greatest positive Poisson's ratio while in the second transversal direction they show the most negative Poisson's ratio [120].

3.5 St.-Venant edge effect reversal

The St.-Venant edge effect is the local concentration of stress in the region of an applied load or boundary condition. As one moves from the surface of the material where the load is applied towards the interior, the stress distribution becomes more uniform. In isotropic materials, fine fluctuations of strain (edge effects) decay rapidly with distance from the surface [124]. Typically, the influence of the boundary condition extends a distance comparable to the specimen width [125]. However, anisotropic materials including sandwich panels [126], fiber-reinforced composites [127, 128] and polymeric micro-composites [129] experience a slow decay of end effects, warranting careful consideration over which systems it is appropriate to invoke St.-Venant's principle. Edge effects in anisotropic materials can be transmitted on the order of several specimen lengths, which is significantly greater than for homogeneous, isotropic materials with identical geometry and boundary conditions [130]. Lakes examined analytically the effect of Poisson's ratio on the decay of edge effects. He found that as ν approaches 0.5 this

induces slow decay of end stress in an axisymmetric cylinder but in other conditions such as the plane sandwich panel an increasingly negative Poisson's ratio results faster decay than it would be otherwise [131]. No firm decay rate-to-Poisson's ratio (γ-to-ν) dependence was established.

Recently, Karpov developed a class of mechanical metamaterials structured as a discrete, two-dimensional lattice of linear elastic small-strain bar elements, and observed that for some configurations there was a marked acceleration of edge-effect decay and even blocking edge effects altogether [132]. The analysis was carried out in the frequency domain to access spectral information about the exponential decay of sinusoidal strain fluctuations at material points. Lattice networks with a high degree of non-local connections—i.e., elastic connections extending beyond only nearest neighbors on the nodal grid, exhibited a fast decay of coarse surface fluctuations versus fine surface fluctuations. This opposes the behavior of continuum solids where coarse patterns of surface strain dissipate over longer distances compared to fine patterns of surface strain. In addition to this inverse reaction to the applied pattern of deformation, highly non-locally interacting lattice structures showed other anomalous effects in response to surface excitation including near-surface deformation arrest or blocking, filtering and phase shifts. None of these effects are seen in continuous solids or even simpler two-dimensional lattice structures [133, 134]. Applications of materials with these spectral properties includes static deformation cloaking, filtering and processing but more generally, the materials could be used to modify or detect significant surface stress fluctuations.

CHAPTER 4

NEGATIVE EXTENSIBILITY UNIT-CELL

Here begins a novel, systematic approach in the analysis of unit-cell structure capable of undergoing a negative extensibility transition. Although the methodology presented here is particularly well-suited in understanding the mechanical response of this elastic structure with two independent degrees of freedom, the approach can be extended to many other types systems whose response is governed by a nonlinear potential.

4.1 Negative extensibility unit-cell

Figure 5 is the unit-cell structure capable of undergoing a negative extensibility transition. It is composed of five linear elastic elements: a middle bar of stiffness k_1, top and bottom bars of stiffness k_2 and springs on either side of stiffness k_3. The initial dimensions are uniquely determined by a horizontal length L, vertical height H and skewness h. The skewness is the degree of offset from the horizontal. At $h = 0$ the structure is rectangular. The structure is pinned at the midpoint of the center bar. Due to symmetry there exists only two independent degrees of freedom, the displacements u and v. Rollers constrain their movement along the vertical direction. The displacement u is the external degree of freedom since the force F is applied at this node. Mechanical work is being done over this node. The displacement v is the internal degree of freedom. No work is being done at this node.

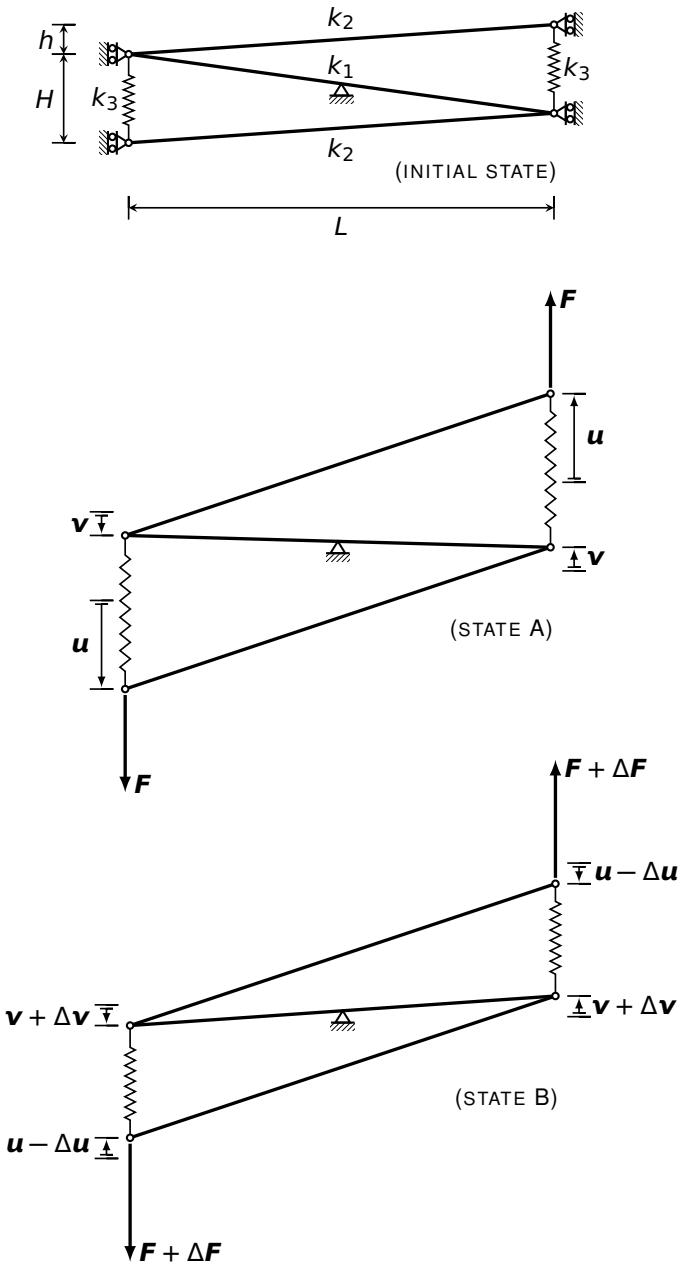

Figure 5: Negative extensibility unit-cell. Structured as five linear elastic elements: middle bar with stiffness k_1, top and bottom bars with stiffness k_2 and springs on the side with stiffness k_3. Dimensions are uniquely defined by length L, height H and skew offset h. There are two independent degrees of freedom, u and v. Displacement boundary conditions are shown in the initial state. Applied forces and resulting displacements are shown in states A and B. During the $A \rightarrow B$ transformation, a contraction $-\Delta u$ over the external degree of freedom u is observed.

4.1.1 Potential function

Two separate formulations for the strain energy function (also called the potential) of the unit-cell structure will be presented:

1. *Green's strain potential:* the Green strain approximation is used for the middle bar with stiffness k_1 and top and bottom bars with stiffness k_2.
2. *Engineering potential:* the true potential with no approximations for any elastic member.

In general, using a Green strain approximation for the strain in a bar element works well at moderate strains (< 0.05) [135]. Later on it will be demonstrated that the Green strain potential is in fact the limiting case of the true potential for the flat unit-cell—that is, when the horizontal length is much greater than the vertical height $L >> H$. The aspect ratio is to be defined $r = \frac{H}{L}$. The Green strain potential is the situation when $r \to 0$. In the analysis, both the Green and engineering potential functions will be put into dimensionless form in order to reduce the number of independent system parameters.

4.2 Green strain potential

4.2.1 Basic definitions

The following definitions are relevant:

$$\text{stiffness: } k = \frac{EA}{l_0} \tag{4.1}$$

$$\text{strain energy: } U = \frac{EA(l_f - l_0)^2}{2l_0} = \frac{1}{2}k\Delta l^2 \tag{4.2}$$

$$\text{Cauchy strain: } \varepsilon_c = \frac{l_f - l_0}{l_0} \tag{4.3}$$

$$\text{Green strain: } \varepsilon_G = \frac{l_f^2 - l_0^2}{2l_o^2} = \frac{1}{2}\left(\frac{l_f^2}{l_o^2} - 1\right) = \varepsilon_c + \frac{1}{2}\varepsilon_c^2 \tag{4.4}$$

$$\text{strain energy: } U \approx \frac{1}{2}kl_0^2\varepsilon_G^2 \quad \text{(after substitution of } k \text{ and } \varepsilon_G) \tag{4.5}$$

4.2.2 Strain energy of each element

The stored strain energy in the middle bar with stiffness k_1 using the Green strain approximation (Equation 4.5)

$$\pi_1 = \frac{1}{2}k_1 l_0^2 \varepsilon_{G_1}^2 \tag{4.6}$$

$$= \frac{1}{2}k_1\left(\sqrt{L^2 + (H-h)^2}\right)^2\left(\frac{2v(v-H+h)}{L^2 + (H-h)^2}\right)^2 \tag{4.7}$$

$$= \frac{2k_1}{L^2 + (H-h)^2}v^2(v-H+h)^2 \tag{4.8}$$

The stored strain energy in the top and bottom bars with stiffness k_2 using the Green strain approximation

$$\pi_2 = \frac{1}{2}k_2 l_0^2 \varepsilon_{G_1}^2 \tag{4.9}$$

$$= \frac{1}{2}k_2 \left(\sqrt{L^2+h^2}\right)^2 \left(\frac{\left(\sqrt{L^2+(h+u+v)^2}\right)^2 - \left(\sqrt{L^2+h^2}\right)^2}{2\left(\sqrt{L^2+h^2}\right)^2} \right)^2 \tag{4.10}$$

$$= \frac{k_2}{8(L^2+h^2)}(u+v)^2(u+v+2h)^2 \tag{4.11}$$

The stored strain energy in the left and right springs with stiffness k_3 using no approximations

$$\pi_3 = \frac{1}{2}k_3(\Delta l)^2 \tag{4.12}$$

$$= \frac{1}{2}k_3 \left(u-v\right)^2 \tag{4.13}$$

4.2.3 Balance of energy

The potential takes into account the collective strain energies U of all elastic elements and the energy of the external load V

$$\Pi = U - V = \pi_1 + 2(\pi_2 + \pi_3 - Fu) \tag{4.14}$$

$$\begin{aligned} \Pi = {} & \frac{2k_1}{L^2+(H-h)^2}v^2(v-H+h)^2 \\ & + \frac{k_2}{4(L^2+h^2)}(u+v)^2(u+v+2h)^2 + k_3\left(u-v\right)^2 - 2Fu \end{aligned} \tag{4.15}$$

4.2.4 Dimensionless potential

The potential Π is reduced to dimensionless form in order to reduce the number of independent system parameters. The potential is divided by an energy term k_3H^2. A dimensionless potential U is defined. This U is not the same as the in Equation 4.14.

$$U = \frac{\Pi}{k_3 H^2} \tag{4.16}$$

Quantities in are redefined in terms of dimensionless parameters:

$$\text{system (design) parameters:} \quad a = \frac{k_2}{4k_3}\frac{H^2}{L^2+H^2}, \quad b = \frac{2k_1}{k_3}\frac{H^2}{L^2+(H-h)^2}, \quad s = \frac{h}{H}, \quad r = \frac{H}{L} \tag{4.17}$$

$$\text{independent state parameters:} \quad x = \frac{u}{H}, \quad y = \frac{v}{H} \tag{4.18}$$

$$\text{control parameter:} \quad f = \frac{F}{k_3 H} \tag{4.19}$$

$$\text{dimensionless potential:} \quad U = \frac{\Pi}{k_3 H^2} \tag{4.20}$$

The system or design parameters a, b, s and r represent quantities that are fixed based on member stiffnesses and geometry. Variable s is the non-dimensional skewness. The aspect ratio r is the ratio of the height H to the length L. It does not show up in the dimensionless Green strain potential. As discussed, Green strain is the case when $r \to 0$. The independent state parameters x and y represent the displacements of the structure when the dimensionless force or control parameter f is applied. Using these definitions the dimensionless Green strain potential becomes

$$U = a(x+y)^2(x+y+2s)^2 + by^2(y-1+s)^2 + (x-y)^2 - 2fx \tag{4.21}$$

In the analysis of the Green strain formulation only rectangular structures will be examined closely. Therefore, the dimensional and dimensionless skewness are zero, $h = s = 0$. The overall dimensionless energy balance for rectangular unit-cells is

$$U = \underbrace{\frac{2k_1}{k_3}\frac{H^2}{L^2+H^2}}_{b}\underbrace{\left[\left(\frac{v}{H}\right)^2 - \frac{v}{H}\right]^2}_{(y^2-y)^2} + \underbrace{\frac{k_2}{4k_3}\frac{H^2}{L^2}}_{a}\underbrace{\left(\frac{u}{H}+\frac{v}{H}\right)^4}_{(x+y)^4} + \underbrace{\left(\frac{u}{H}-\frac{v}{H}\right)^2}_{(x-y)^2} - \underbrace{\frac{2F}{k_3 H}}_{2f}\underbrace{\frac{u}{H}}_{x} \tag{4.22}$$

Substituting terms, the dimensionless potential is a 4^{th} order polynomial

$$U = a(x+y)^4 + b\left(y^2-y\right)^2 + (x-y)^2 - 2fx \tag{4.23}$$

4.2.5 Force-response curves

Like the two-bar truss, the negative extensibility unit-cell structure undergoes several qualitatively distinct types of force-response curves depending on the values of the system parameters a, b and s. There are now two degrees of freedom. The external degree of freedom x is of primary interest and is the point where the load is applied. The strain of the structure can be defined

$$\varepsilon = 2x \tag{4.24}$$

Different from the truss, this two-degree-of-freedom unit-cell exhibits a new characteristic response where the structure contracts intermittently at a critical force during loading. This contraction corresponds to the forward phase transformation $A \rightarrow B$. This effect can be visualized by the 'pulling-back' of the middle bar as it rotates beyond a horizontal configuration. At this critical point of destabilization, a new equilibrium is reached but only after a discontinuous jump in both degrees of freedom. Interestingly, the external degree of freedom x contracts,

opposing the line of increasing external tension. Negative extensibility is associated with a pinched hysteresis loop. Over the region of pinched hysteresis, work is negative. If displacement opposes the applied tension then the system is doing work on the surroundings. The forward transformation $A \rightarrow B$ is a condensation reaction, and energy is released from the system to the surroundings.

During unloading, the structure may fully recover to its original state $B \rightarrow A$ or it may remain stuck in the deformed state. Therefore, these two additional hysteretic, bistable responses are termed negative extensibility of the superelastic type (NESE) and negative extensibility of the superplastic type (NESP). The five unique mechanical responses of the unit-cell are:

1. Monostability (MS)
2. Superelasticity (SE)
3. Superplasticity (SP)
4. Negative extensibility of the superelastic type (NESE)
5. Negative extensibility of the superplastic type (NESP)

They are graphed in Figure 5. In order to generate force-response curves requires that derivatives with respect to both degrees of freedom, x and y in the dimensionless potential, be equal to zero. Equilibrium conditions can be written

$$U'_x = g_1(x, y, f_c, a, b, r, s) = 0 \tag{4.25}$$

$$U'_y = g_2(x, y, f_c, a, b, r, s) = 0 \tag{4.26}$$

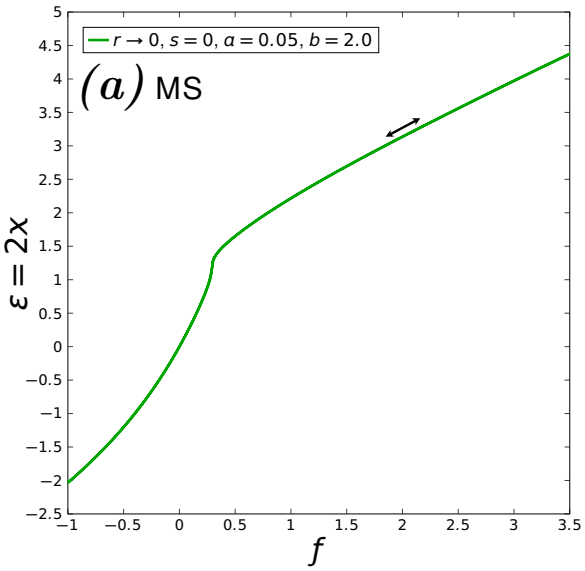
$r \to 0, s = 0, a = 0.05, b = 2.0$
(a) MS
$\varepsilon = 2x$
f

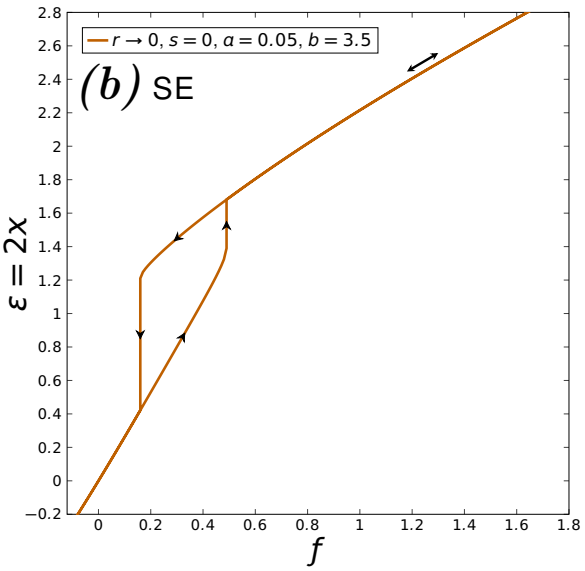
$r \to 0, s = 0, a = 0.05, b = 3.5$
(b) SE
$\varepsilon = 2x$
f

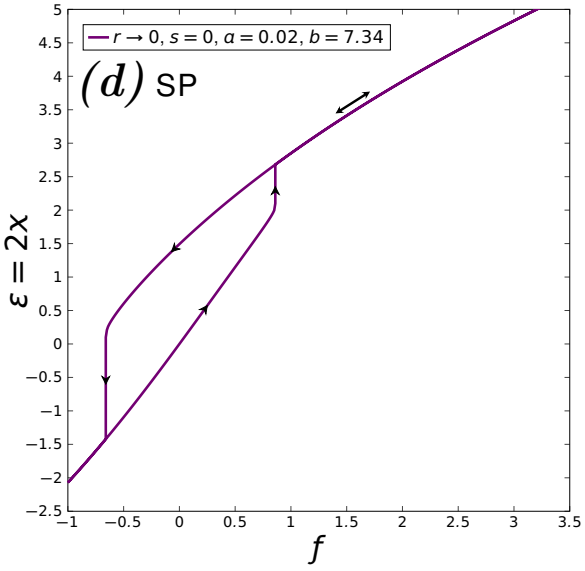
$r \to 0, s = 0, a = 0.02, b = 7.34$
(d) SP
$\varepsilon = 2x$
f

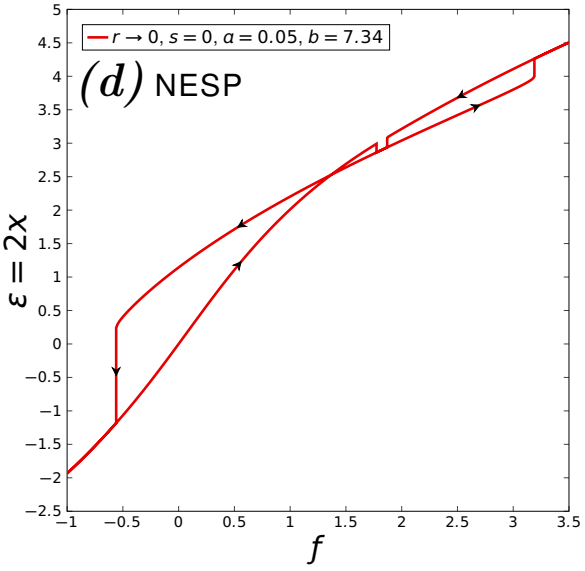
$r \to 0, s = 0, a = 0.05, b = 7.34$
(d) NESP
$\varepsilon = 2x$
f

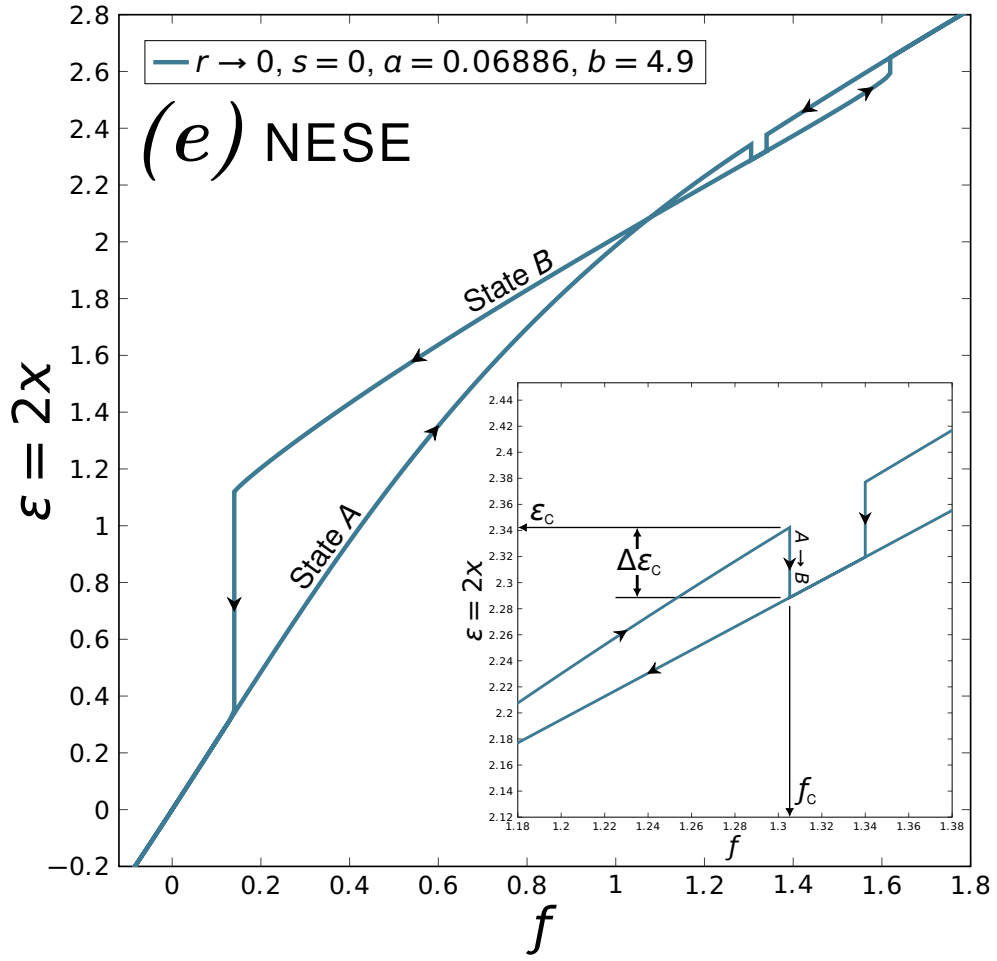

Figure 5: Five distinct mechanical responses for the unit-cell. (a): Monostability. The response while nonlinear remains smooth and continuous. (b): Superelasticity (SE). A single hysteresis loop exists in the tensile region. The forward transformation $A \to B$ is an extension. (c): Superplasticity. A single hysteresis loop is seen expanding over the regions of tension and compression. In order to restore the original configuration, the load must be reversed. (d): Negative extensibility of the superplastic type (NESP). Like the superplastic response, the hysteresis loop expands into the compressive (negative) region. However, the forward transformation $A \to B$ is a marked contraction. The hysteresis loop is 'pinched.' A secondary hysteresis loop in the tensile region is observed. This secondary loop is of the usual superelastic type. (e): Negative extensibility of the superelastic type (NESE). Zooming into the curve, at the critical force f_c and critical strain ε_c there is a forward phase transformation $A \to B$. The change in strain $\Delta\varepsilon_c$ is the degree of contraction. Similarly, there is a second hysteresis loop of the superelastic type in the tensile region. *[All graphs use the same axes scale, width:height=1.8:3]*

Prior to loading, the system parameters a, b are fixed. For the Green strain potential only zero skewness $s = 0$ is considered. The aspect ratio r is not present although it will be in the engineering potential. Defining equilibrium conditions U'_x and U'_y as the functions g_1 and g_2 will later be useful in developing more complex systems of equations. To simulate loading, the equilibrium conditions are used to solve for the displacements x and y using discrete values for the control parameter f by a Newton-Raphson numerical algorithm. The load is gradually incremented, using converged solutions from the previous step as the initial guess for the next step. After reaching the final forward phase transformation, the load is then decremented following the same numerical algorithm.

The five basic types of mechanical responses (Figure 5) are defined based on the primary tensile hysteresis loop only. In the next chapter, it will become more apparent that at certain combinations of design parameters there will be a secondary hysteresis loop in the tensile region. During a load-unload cycle, the existence of two hysteresis loops results in the four-fold switching pattern $A \to B \to A \to B \to A$. A systematic way of determining which sets of parameters lead to which mechanical response is the generation of a phase diagram where boundary lines represent the onset of a type of response. Computational methods are developed in Chapter 5 to construct these phase diagrams mathematically.

4.3 Engineering (true) potential

The true potential differs from the Green strain potential in that no approximations are used for the strain energy of the three bars. Consequently, there will be an additional independent design parameter in the dimensionless engineering formulation that was not present in the Green

strain potential. This is the ratio of the height H of the structure to its width L defined as the aspect ratio $r = H/L$. The additional parameter r adds another dimension to the design space. Also, in Chapter 5 the skewness s will be accounted for such that there is an even greater range of possibilities.

4.3.1 Strain energy of each element

The stored strain energy in the bars k_1 and k_2 and the spring k_3 is based off the simple linear elastic relation $U = \frac{1}{2}k\Delta l^2$

$$\pi_1 = \frac{1}{2}k_1\left(\sqrt{L^2 + (H - h - 2v)^2} - \sqrt{L^2 + (H - h)^2}\right)^2 \tag{4.27}$$

$$\pi_2 = \frac{1}{2}k_2\left(\sqrt{L^2 + (h + u + v)^2} - \sqrt{L^2 + h^2}\right)^2 \tag{4.28}$$

$$\pi_3 = \frac{1}{2}k_3\left(u - v\right)^2 \tag{4.29}$$

4.3.2 Balance of energy

The true potential is defined as the strain energies of elastic elements U minus the energy of the external load V

$$\Pi = U - V = \pi_1 + 2(\pi_2 + \pi_3 - Fu) \tag{4.30}$$

Substituting the strain energies π of each element, the fully dimensional engineering potential for the unit-cell is

$$\begin{aligned}\Pi = \frac{1}{2}k_1\left(\sqrt{L^2 + (H - h - 2v)^2} - \sqrt{L^2 + (H - h)^2}\right)^2 \\ + k_2\left(\sqrt{L^2 + (h + u + v)^2} - \sqrt{L^2 + h^2}\right)^2 + k_3\left(u - v\right)^2 - 2Fu\end{aligned} \tag{4.31}$$

4.3.3 Dimensionless potential

The potential Π is reduced to dimensionless form so as to reduce the number of independent system parameters. This is accomplished by dividing by the same energy term k_3H^2. The resulting dimensionless potential U is defined using the same dimensionless parameters as for the Green strain potential except with the addition of the aspect ratio r. The parameters are tabulated with a short description (Table 2). Use of the same parameters makes the process of non-dimensionalization quite tedious, however it will be essential in comparing the two potentials.

The substitution of these dimensionless parameters into the true potential (Equation 4.31) after non-dimensionalization requires extreme care. For a complete derivation see Appendix A. The final form of the dimensionless engineering potential is

$$\begin{aligned} U = {} & 4a\left(s^2+\frac{1}{r^2}\right)\left(\sqrt{\frac{1}{r^2}+(s+x+y)^2}-\sqrt{\frac{1}{r^2}+s^2}\right)^2 \\ & +\frac{b}{4}\left(s^2-2s+\frac{1}{r^2}+1\right)\left(\sqrt{\frac{1}{r^2}+(1-s-2y)^2}-\sqrt{\frac{1}{r^2}+(1-s)^2}\right)^2 \\ & +(x-y)^2-2fx \end{aligned} \tag{4.32}$$

This potential has the same five characteristic force-response curves, which are shown in Figure 5. The mechanical response depends on the values of the design parameters a, b, s and r. First, second and third derivatives of this potential with respect to each variable get quite tedious but the computer software Matlab® does these automatically. The ability to compute the analytical derivatives of the potential permits fast convergence when using a numerical method for optimization such as the Newton-Raphson root-finding method.

TABLE 2: Dimensionless parameters

	Definition	Description
Dimensionless potential	$U = \dfrac{\Pi}{k_3 H^2}$	Potential is divided by an energy term associated with the spring $k_3 H^2$
System (design) parameters	$a = \dfrac{k_2}{4k_3}\dfrac{H^2}{L^2}$	Dimensionless top and bottom bar stiffness scaled by geometry terms
	$b = \dfrac{k_1}{k_3}\dfrac{H^2}{L^2+H^2}$	Dimensionless middle bar stiffness scaled by geometry terms
	$s = \dfrac{h}{H}$	Skewness represents offset from the horizontal
	$r = \dfrac{H}{L}$	Aspect ratio defined as the ratio of height to length
Independent state parameters	$x = \dfrac{u}{H}$	Dimensionless displacement of the external degree of freedom u
	$y = \dfrac{v}{H}$	Dimensionless displacement of the internal degree of freedom v
Control parameter	$f = \dfrac{F}{k_3 H}$	Dimensionless load input into the system

CHAPTER 5

PHASE DIAGRAM CALCULATION

5.1 Phase diagrams in materials science

Ursula Kattner states that "Phase diagrams are visual representations of the state of a material as a function of temperature, pressure, and concentrations of the constituent components" [136]. Phase diagrams differ from normal graphs in which one variable is plotted as a function of another. In phase diagrams, the coordinate axes all represent independent variables and the coordinate space shows the state of the system at equilibrium [137]. Also, the points in between boundary lines have meaning whereas in a plot $f(x)$ only points on the curve have meaning. Phase diagrams are considered the blueprints for alloy design, development, processing, and understanding of material properties [136]. When developing multi-component, multi-phase materials such as alloys it is essential to know how processing affects microstructure and relative quantities of the phases present since this dictates the physical and mechanical properties of the material. Phase diagrams such as binary diagrams for steel or ternary diagrams for ceramics shed light on how composition and temperature affect phase equilibria.

Constructing phase diagrams empirically is an arduous process, requiring many experiments at different temperature and composition regimes. Starting in the 1970's, computational methods were developed for calculating phase diagrams as well as calculating thermodynamic properties of multi-component, multi-phase systems and simulations of more complex phenom-

ena such as diffusion and phase transformations [138]. These methods are based on numerical optimization or minimization of Gibbs energy equations, which are used to model the thermodynamic phases of materials [139].

The computational techniques implemented to generate phase diagrams in this manuscript are essentially no different than those in existing commercial thermodynamic software [137, 140, 141]. However, the fundamental difference is that in this manuscript the nonlinear mechanical response, which is a function of relative stiffnesses of members and dimensions becomes of key interest rather than the set of stable microstructural phases, which is a function of mass percents of chemical constituents, temperature and pressure. Regions of the diagram pertain to a specific mechanical behavior of the structure rather than a specific microstructural phase. The axes represent design parameters such as relative stiffnesses rather than thermodynamic quantities like temperature and mole fraction. At the most basic level, computing boundary lines for stability of thermodynamic phases and boundary lines for stability of a specific mechanical response both rely on the ability to compute a global energy minimum together with an additional set of constraints.

5.2 Stability diagram

The presentation of the phase diagrams and key findings in this manuscript should be prefaced with a discussion of stability diagrams, which are an important tool used in structural and thermodynamic systems. Stability diagrams reveal points of destabilization for a given set of system parameters. In structural analysis, one axis is the critical load f_c (or critical displacement

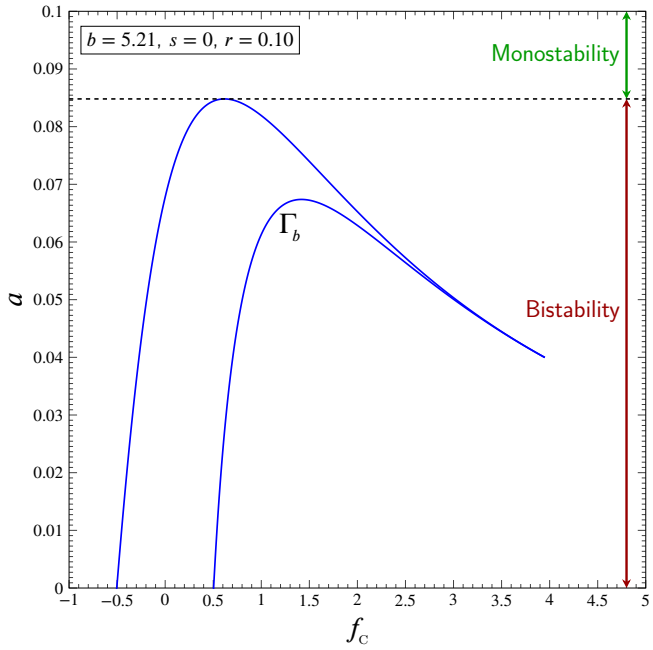

Figure 6: Stability diagram for the unit-cell. Parameters $b = 5.21$, $r = 0.10$, $s = 0$ are fixed while the critical force f_c and the system parameter a are varied. Points along the blue curves Γ_b are the points of destabilization. When $a > 0.085$ the structure is monostable. As a is decreased, the peaks of each of the curve are bifurcation points marking the onset of a hysteresis loop. Also, the point where the two curves meet at a sharp point is different type of cusp point. Below the sharp cusp singularity there is only one hysteresis loop or two-fold switching $A \to B \to A$ in a load-unload cycle. Above the sharp singularity there are two hysteresis loops or four-fold switching $A \to B \to A \to B \to A$.

x_c) and the other axis is a system parameter of interest. All other system parameters must be fixed. Thus, often it is a cross-section of a more complex higher dimensional surface.

For some combinations of the input load and system parameters there are points where equilibrium becomes unstable. These critical points are plotted parametrically as curves in the stability diagram. For the negative extensibility unit-cell, points of destabilization correspond to a polymorphic phase transformation and vertical discontinuity in the displacement. Once equilibrium is restored, the result is a new phase with a different effective stiffness than the

original configuration. A stability diagram for the unit-cell is shown in Figure 6. A shortcoming of stability diagrams is that the nature of the response in the bistable region, e.g., SE, SP, NESE, NESP is unknown. All that is known is the location of critical destabilizing loads leading to hysteretic bistability. Moreover, stability diagrams are limited because it is a single cross-section requiring all but two parameters to be fixed. If b is changed then an entire new diagram must be constructed.

In order to generate a curves in the stability diagram requires three conditions to be satisfied:

$$g_1(x, y, f_c, a, b, r, s) = U'_x = 0 \tag{5.1}$$

$$g_2(x, y, f_c, a, b, r, s) = U'_y = 0 \tag{5.2}$$

$$g_3(x, y, f_c, a, b, r, s) = \det H = 0 \tag{5.3}$$

The first two are conditions of equilibrium. The third condition is the requirement of the determinant of the Hessian matrix, a matrix of second-order derivatives, to be zero.

$$\det H = \begin{vmatrix} U''_{xx} & U''_{xy} \\ U''_{yx} & U''_{yy} \end{vmatrix} = U''_{xx}U''_{yy} - U''_{xy}U''_{yx} = 0 \tag{5.4}$$

When the determinant of the Hessian is zero and equilibrium conditions are satisfied in the vicinity of the critical point, these are the criteria for a point which is simultaneously an inflection point and a stationary point—i.e., a saddle point. Physically, this is a point of structural destabilization. To compute the diagram in Figure 6 the aspect ratio r, skewness s and design parameter b are fixed. The unknowns are then x, y, f_c and a. One of these parameters is used as a running variable in the numerical algorithm meaning that it is fixed

for each iteration. This leaves three unknowns to be solved by the three conditions. Points of destabilization are solved numerically by a Newton-Raphson scheme using either f_c or a as a running variable and then plotted parametrically on the (f_c, a)–stability diagram. Although not shown, it is possible to use a different system parameter on the y-axis such as b or use an independent state parameter on the x-axis such as x_c.

5.3 Phase diagram

Like the stability diagram, boundary lines in the phase diagram are defined by a set of constraints. The axes in the phase diagram are taken to be the system parameters a and b. The aspect ratio r and skewness s are fixed for a given diagram. The regions in the diagram are one of the five types of mechanical responses: MS, SE, SP, NESE or NESP. There are five boundary lines delineating the system response:

Γ_E: the boundary between superelasticity and superplasticity.

Γ_S: the boundary between monostability and bistability. Referred to as the cusp curve since these are conditions for a cusp singularity. A hysteresis loop is generated when passing over this boundary.

Γ_M: the boundary between elongation and contraction for the forward phase transformation $A \to B$. This curve separates the usual SE and SP responses from the more interesting NESE and NESP responses. Referred to as the NESE boundary.

Γ_N: the boundary between monostability and inaccessible bistability. Referred to as the nucleation curve. When passing over this boundary line, a second solution nucleates

although it cannot be accessed under normal loading conditions. The mechanical response remains monostable.

Γ_O: the boundary between monostability and NESE or NESP. Referred to as the coalescence curve. Below this boundary, the second solution which had nucleated earlier becomes accessible. The structure now exhibits the bistable NESE or NESP response.

Contours in the diagram show properties of the hysteretic response including

1. intensity of the strain change at the forward transformation
2. relative width of the primary hysteresis loop

5.3.1 Superelasticity-superplasticity curve

Conditions for the superelasticity-superplasticity curve Γ_E require the equilibrium and destabilization criteria be satisfied with the additional constraint that the critical force for the reverse transformation $B \rightarrow A$ is set at zero, $f_c = 0$. When the reverse critical force is zero, the structure is neither plastic nor elastic.

$$\Gamma_E : \qquad g_1(x, y, f_c = 0, a, b, r, s) = 0 \tag{5.5}$$

$$g_2(x, y, f_c = 0, a, b, r, s) = 0 \tag{5.6}$$

$$g_3(x, y, f_c = 0, a, b, r, s) = 0 \tag{5.7}$$

The additional constraint reduces the number of unknowns to 6. Always the aspect ratio r and skewness s are fixed for a given phase diagram. There are now 4 unknowns: x, y, a, b. Using one of these as a running variable reduces the number of unknowns to three. The three

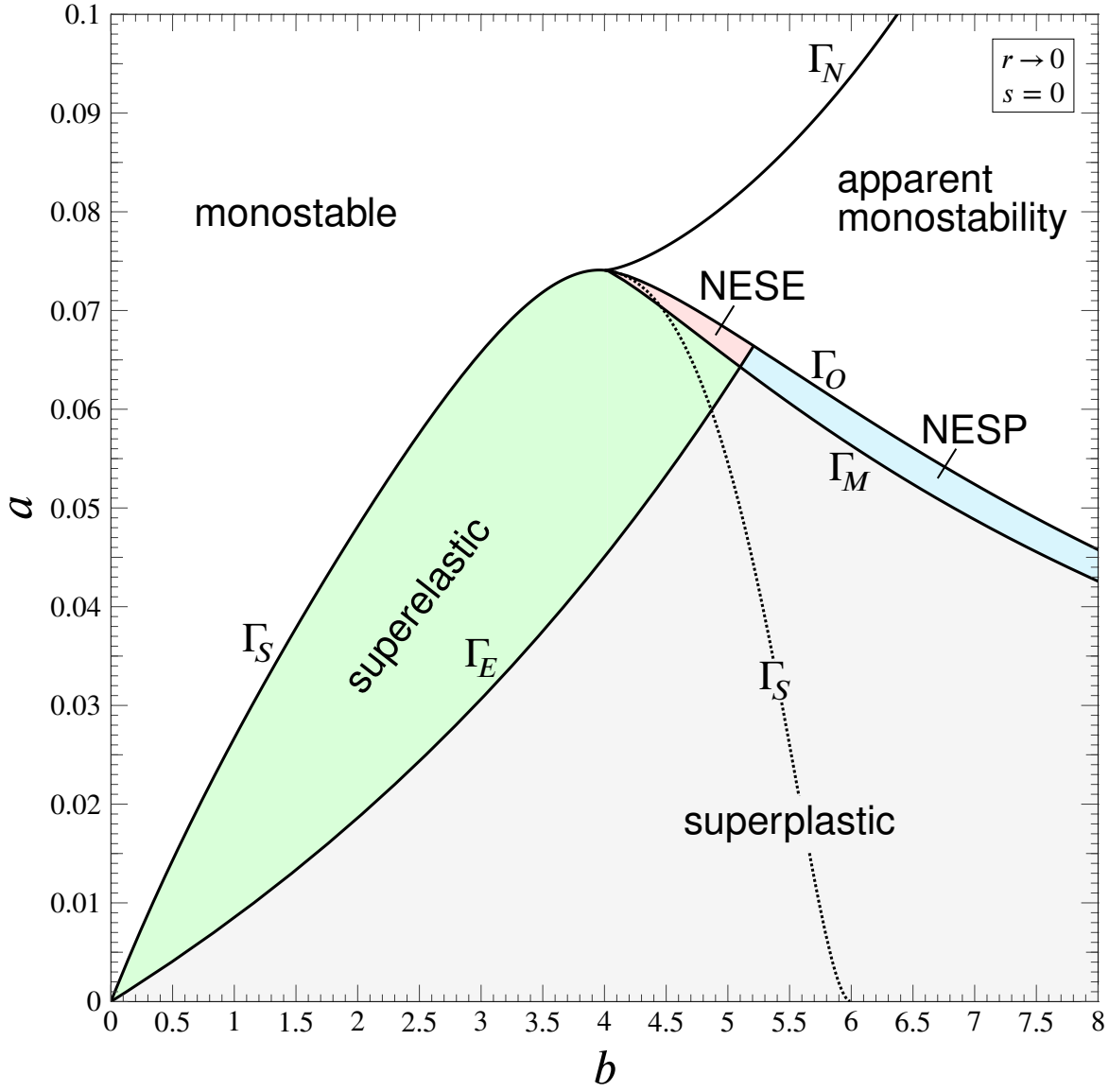

Figure 7: Green strain phase diagram showing what the different regions mean. The phase diagram is defined by five boundary lines Γ_E, Γ_S, Γ_M, Γ_N and Γ_O. The dotted Γ_S corresponds to the formation of a secondary tensile hysteresis loop. To the right of this curve all bistable regions have two tensile hysteresis loops.

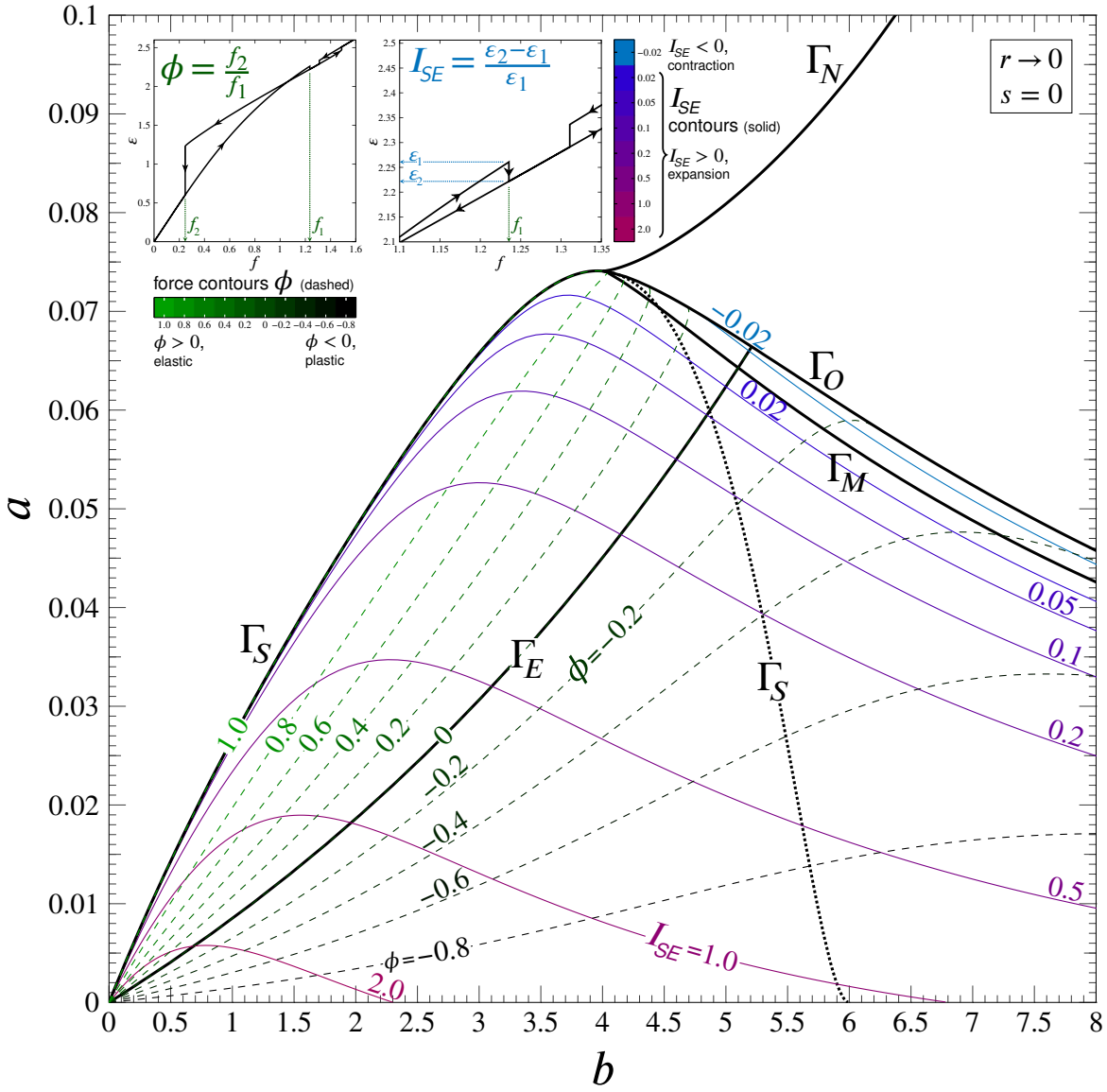

Figure 8: Green strain phase diagram with contours lines plotted. Dashed black and green contours are the ratio of the critical force at the reverse transformation f_2 to the critical force at the forward transformation f_1, $\phi = f_2/f_1$. The force ratio contours express the relative width of the hysteresis loop. Lower ϕ means a wider hysteresis loop. Positive values of ϕ are superelastic while negative values are superplastic. The solid purple and blue contours are the superelastic strain intensity contours I_{SE} at the forward transformation, where $I_{SE} = \frac{\varepsilon_2 - \varepsilon_1}{\varepsilon_1}$. Larger positive I_{SE} is a larger and sooner onset superelastic expansion. Negative I_{SE} is a contraction, which occurs in the NESE and NESP regions. I_{SE} approaches zero at Γ_M.

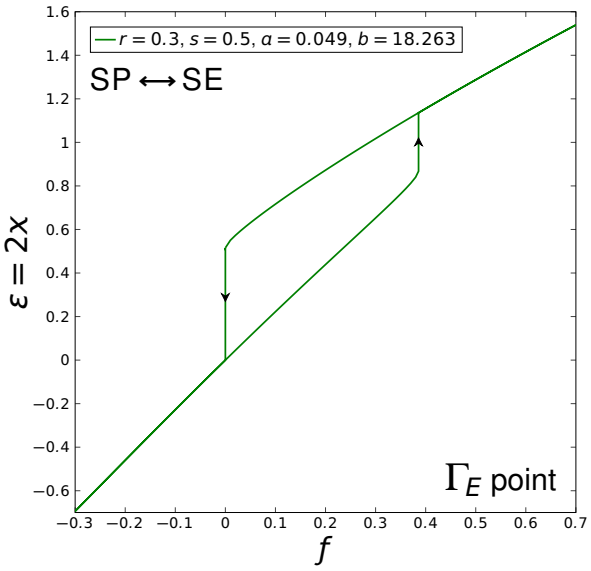

Figure 9: Force-response curve at the superelasticity-superplasticity boundary Γ_E. The reverse transformation $B \to A$ occurs at zero load $f_c = 0$. The response is neither definitively superelastic nor superplastic. The response will become SP if the parameter b is increased slightly or SE if the parameter b is decreased slightly.

equations are sufficient to generate Γ_E provided the initial guess to start the Newton-Raphson scheme leads to physical, non-negative solutions for the design parameters a and b.

5.3.2 Cusp curve

Conditions for the cusp curve Γ_S are the most intricate of all boundary lines. The algorithm converges to the exact point of hysteresis loop formation. Cusp points along Γ_S divide monostability from bistability. The conditions are based on two sets of destabilization criteria (6 total equations). Each set has different variables for the displacements x_1, y_1 and x_2, y_2. However, the critical force f_c is the same across all six equations. When a hysteresis loop initially forms, critical points of destabilization corresponding to the forward and the reverse transformations are nearly touching (the sides of the loop are nearly touching). Only at a cusp singularity will

the two points of destabilization meet exactly at a single critical force. At this particular cusp singularity, the hysteresis loop is reduced to a point. A bifurcation of this type occurs in one place in the cusp catastrophe, Figure 3 (b)—the sharp point of the bifurcation set where the top and bottom sheets split apart.

$$\Gamma_S: \quad g_1(x_1, y_1, f_{c1}, a, b) = 0 \tag{5.8}$$

$$g_2(x_1, y_1, f_{c1}, a, b) = 0 \tag{5.9}$$

$$g_3(x_1, y_1, f_{c1}, a, b) = 0 \tag{5.10}$$

$$g_1(x_2, y_2, f_{c2} = f_{c1}, a, b) = 0 \tag{5.11}$$

$$g_2(x_2, y_2, f_{c2} = f_{c1}, a, b) = 0 \tag{5.12}$$

$$g_3(x_2, y_2, f_{c2} = f_{c1}, a, b) = 0 \tag{5.13}$$

Aspect ratio and skewness are to be fixed and from now on will not be shown explicitly in the systems of equations. For the cusp conditions to work, a single running variable is taken, usually a or b, reducing the number of unknowns to 6: x_1, x_2, y_1, y_2, f_{c1} and either a or b. The system is fully specified. Figure 10 (a) shows a force-response curve generated at a converged Γ_S point. Figure 10 (b) is just inside the boundary of Γ_S. Hysteresis is now present.

The trial solution for the dimensionless displacements must be different. Either $x_1 \neq x_2$ or $y_1 \neq y_2$. Additionally, the trial guesses for the unknowns must ensure that solutions for the design parameters a and b end up in quadrant I. Results reveal that there are multiple Γ_S curves, each is associated with the generation of a different hysteresis loop. The secondary hysteresis loop in the tensile region forms at a Γ_S curve shown as a dotted line in the phase

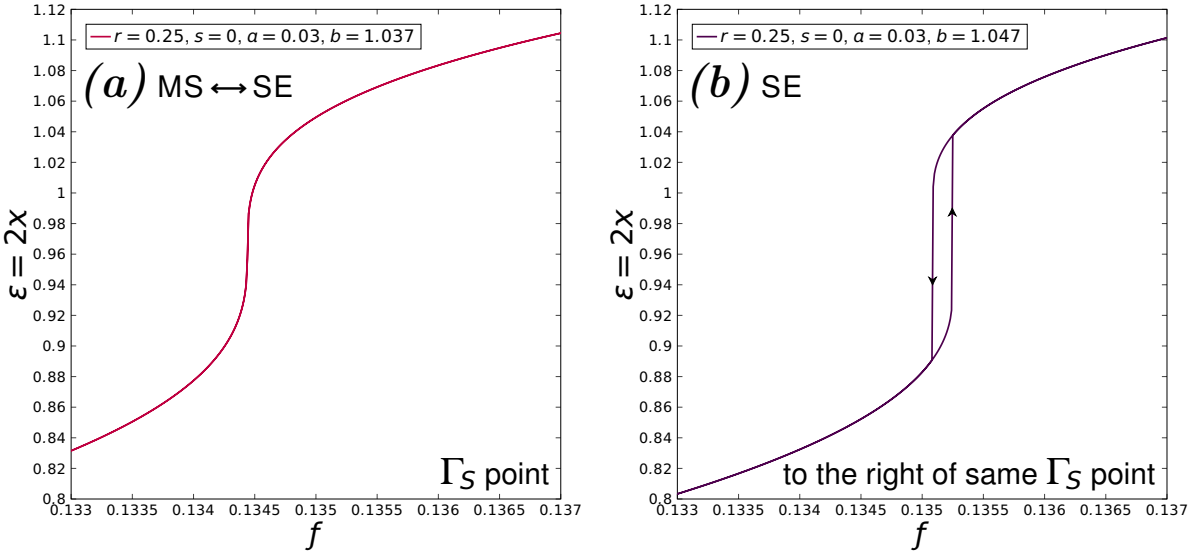

Figure 10: Cusp points defined by Γ_S are points of hysteresis formation. (a): Force-response curve at a converged Γ_S point. The response is the onset of bistability from monostability. (b): Force-response curve with b increased by 0.01 relative to the Γ_S point. The response is superelastic.

diagrams. While compressive loops exist in a mathematical sense, only hysteresis loops in the tensile region are considered physically significant. From an engineering standpoint, the cusp curve Γ_S conditions are extremely accurate in pinpointing the location of solution splitting. A deeper mathematical analysis is a topic for another paper.

5.3.3 Pinched hysteresis and fold-point conditions

The boundary lines Γ_M, Γ_N and Γ_O use the same set of conditions. The trial solution in the Newton-Raphson algorithm determines what curve will be accessed. The nature of the bifurcation associated with each boundary line is different. For Γ_M, the conditions specify the onset of a pinched hysteresis loop. This happens when a point of destabilization defined by g_1, g_2 and g_3 occurs at the same critical load and critical displacement as a stable solution of

equilibrium defined by g_1 and g_2. Therefore, $f_{c1} = f_{c2}$ and $x_1 = x_2$ where x_1, y_1 and f_{c1} are associated with a point of destabilization while the variables x_2, y_2 and f_{c2} are associated with a stable solution of equilibrium.

$$\Gamma_M,\ \Gamma_N,\ \Gamma_O: \qquad g_1(x_1, y_1, f_{c1}, a, b) = 0 \tag{5.14}$$

$$g_2(x_1, y_1, f_{c1}, a, b) = 0 \tag{5.15}$$

$$g_3(x_1, y_1, f_{c1}, a, b) = 0 \tag{5.16}$$

$$g_1(x_2 = x_1, y_2, f_{c2} = f_{c1}, a, b) = 0 \tag{5.17}$$

$$g_2(x_2 = x_1, y_2, f_{c2} = f_{c1}, a, b) = 0 \tag{5.18}$$

The onset of pinched hysteresis is illustrated when traversing across Γ_M (Figure 11). At a constant critical force f_c during the forward transformation $A \rightarrow B$, the system destabilizes and then re-equilibrates with no net change in the displacement, $x_2 = x_1$. There is still a large displacement jump in the internal degree of freedom y, $y_2 \neq y_1$. The boundary Γ_M divides the usual SE or SP responses from the NESE or NESP responses.

The coalescence curve Γ_O divides the regions of NESE and NESP from a region of apparent monostability. 'Apparent' monostability refers to the fact that in the region above Γ_O a second, mathematical solution of equilibrium exists but is not realized under normal loading conditions. Figure 12 shows that when crossing over Γ_O the two hysteresis loops merge. The response shifts abruptly to monostability. The reason the above conditions work for Γ_O is related to the merging of the two hysteresis loops. The initial point of destabilization at the negative extensibility transition $A \rightarrow B$ is stabilized when the two loops merge, $x_1\,(\text{unstable}) = x_2\,(\text{stable})$ at Γ_O.

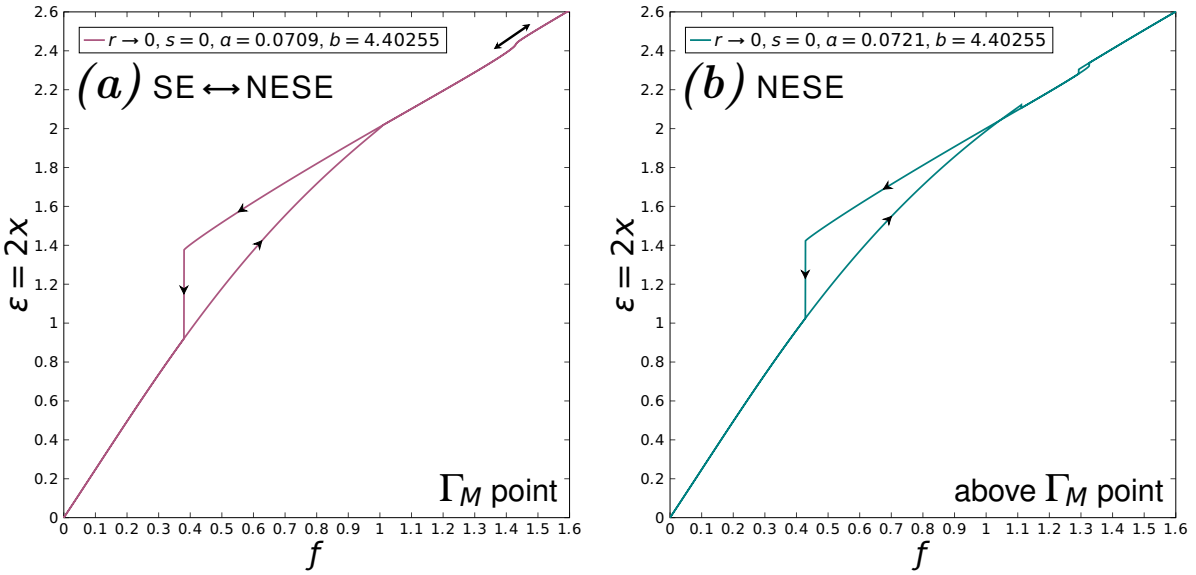

Figure 11: The NESE boundary Γ_M divides the usual SE or SP responses from the NESE or NESP responses. (a): Force-response curve at a Γ_M point. The response shows a single hysteresis loop but the forward transformation $A \rightarrow B$ results in no change in displacement for the external degree of freedom, $x_2 = x_1$. The internal degree of freedom y (not shown) experiences a discontinuous elongation at the critical load, $y_2 \neq y_1$. (b): Force-response curve when a is increased by 0.0012 from the original Γ_M point. The response is NESE with the characteristic pinched hysteresis. The dotted Γ_S boundary is also crossed causing a second hysteresis loop to form.

Coalescence points along Γ_O are singularities where a solution of equilibrium, which satisfies g_1, g_2, becomes a point of destabilization such that it now satisfies g_3 in addition to g_1 and g_2. This higher-order bifurcation causes two hysteresis loops to emerge in the force-response curve. This abrupt change in the behavior is analogous a fold-point in the cusp catastrophe, Figure 3 (b). At a fold-point a large hysteretic response emerges from a monostable response. The transition is non-smooth and abrupt. In the cusp catastrophe, fold-points lie along the bifurcation set. The sudden, discontinuous transition at a fold-point occurs when approaching the bifurcation set laterally, starting from a high point along the top sheet or low point along the bottom sheet.

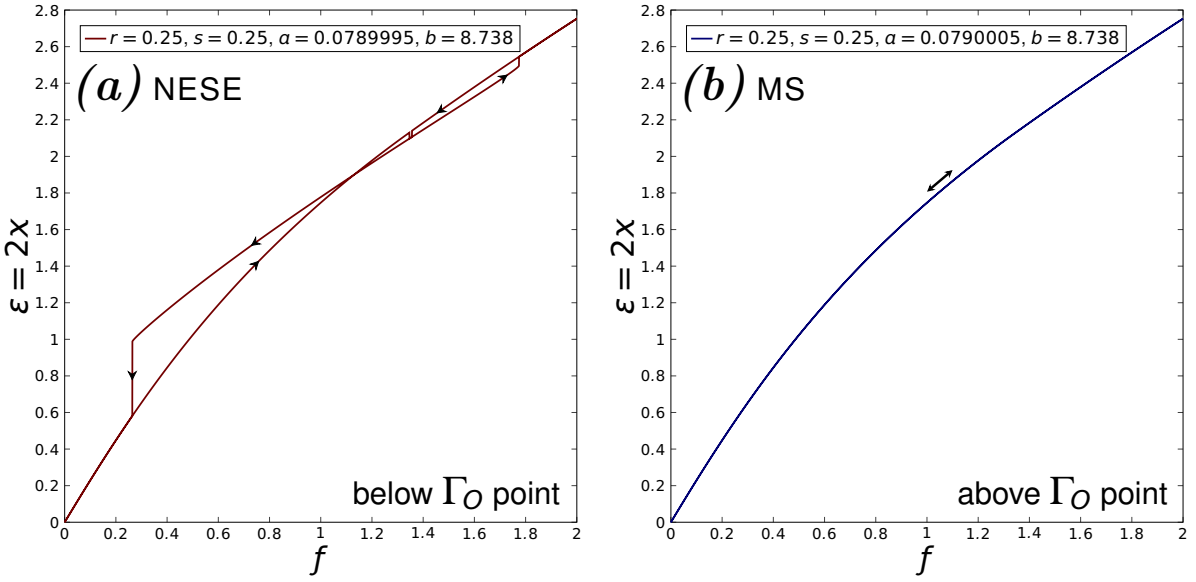

Figure 12: Coalescence points defined by Γ_O are points dividing NESE or NESP from monostability. (a): Force-response curve just below a Γ_O point. The response is NESE. The two hysteresis loops are nearly touching. (b): Force-response curve just above a Γ_O point. The response is monostable.

The nucleation curve Γ_N divides monostability from inaccessible bistability/apparent monostability. The logic in explaining why Γ_N uses the above set of conditions is identical to the logic in explaining why Γ_O uses them. A point of monostability, which has one solution of equilibrium satisfying only g_1 and g_2, shifts to a destabilization point such that now satisfies g_3 in addition to g_1 and g_2. Mathematically, a secondary solution bifurcates from this destabilization point although it cannot be accessed under physical loading. In other words, when crossing over Γ_N an inaccessible hysteresis loop develops. The inaccessible bistability is readily observed on the stability diagram. A comparison bewteen the stability and phase diagrams is shown in Figure 13. The peak of the top blue curve at the dashed line corresponds exactly to a point of Γ_N. The stability diagram is misleading because right below the dashed line is a region of inaccessible

bistability. As a is decreased, physical bistability occurs at Γ_O. A point of Γ_O is associated with the peak of the second, lower blue curve Γ_b. Bistability becomes accessible below this second peak. This particular stability diagram does not reveal a point of Γ_M, which divides NESE from SE. This is because Γ_M is different from the Γ_O and Γ_N fold-type bifurcations that separate monostability from bistability. Instead, Γ_M alters the nature of the already existing bistable response causing it to become pinched. A deeper discussion of the inaccessible region of bistability between Γ_N and Γ_O is based on the interaction between the internal and external degrees of freedom. This is not discussed.

5.3.4 Superelastic strain intensity contours

The superelastic intensity of the forward transformation $A \rightarrow B$ defined as the strain after the transformation ε_2 minus the critical strain at the onset of the transformation ε_1 normalized by the critical strain ε_1.

$$I_{SE} = \frac{\varepsilon_2 - \varepsilon_1}{\varepsilon_1} \tag{5.19}$$

The Green strain phase diagram inset (Figure 8) shows the NESE response with definition of the strain intensity contours. A larger positive I_{SE} means the discontinuous elongation is relatively more intense—i.e., it is associated with a sooner onset (lower critical strain ε_1) and a larger positive strain change $\Delta\varepsilon$ over the transformation. The strain intensity I_{SE} is negative in the NESE and NESP regions because the forward transformation is a contraction. Approaching Γ_O and moving into the NESP region, the negative strain intensity I_{SE} will increase in magnitude. That is, the intensity of the negative extension increases for increasing b and decreasing a within

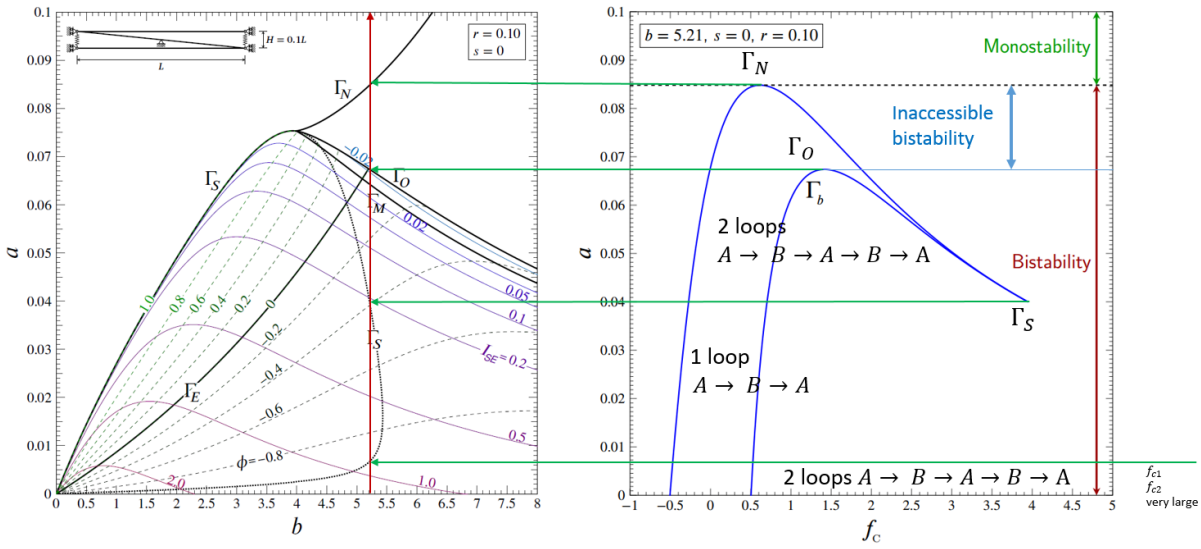

Figure 13: Relationships between the phase diagram (Left) and stability diagram (Right) for $r = 0.10$, $s = 0$. The stability diagram is at a constant $b = 5.21$, which corresponds to the vertical line on the phase diagram. In the stability diagram, the peak of the top blue curve corresponds to a point of Γ_N and the onset of a hysteresis loop. The hysteresis loop is inaccessible so below this point is inaccessible bistability. Bistability becomes accessible when reaching the second peak corresponding to a point of Γ_O. Γ_M is not defined in the stability diagram because Γ_M only changes the nature of an already existing hysteretic response causing it to become pinched. When traversing to lower a, a point of Γ_S is reached which marks the onset of a hysteresis loop. Below this point there is only 1 loop. However, if a is decreased to around 0.008, the secondary loop is generated again but at high, nonphysical critical forces f_c.

the NESE and NESP regions. At the intersection of Γ_E and Γ_O is where most negative I_{SE} occurs while still being NESE. This intersection point is referred to as the 'triple point.' The NESP response will be capable of achieving the most negative I_{SE}.

The strain intensity contours are related to the boundary Γ_M. For Γ_M the condition $x_2 = x_1$ defines zero net change in strain over the transformation. If the Equation 5.19 is solved for x_2, then the transformation can be defined by a pre-defined change in strain over the transformation:

$$x_2 = x_1(1 + I_{SE}) \tag{5.20}$$

The conditions are written as

$$I_{SE}: \qquad g_1(x_1, y_1, f_{c1}, a, b) = 0 \tag{5.21}$$

$$g_2(x_1, y_1, f_{c1}, a, b) = 0 \tag{5.22}$$

$$g_3(x_1, y_1, f_{c1}, a, b) = 0 \tag{5.23}$$

$$g_1(x_2 = x_1(1 + I_{SE}), y_2, f_{c2} = f_{c1}, a, b) = 0 \tag{5.24}$$

$$g_2(x_2 = x_1(1 + I_{SE}), y_2, f_{c2} = f_{c1}, a, b) = 0 \tag{5.25}$$

Usually, a or b is used as a running variable. The value of I_{SE} is fixed at the beginning of the program. It represents an added constraint reducing the number of unknowns. The five equations are sufficient to solve for the five unknowns: x_1, y_1, y_2, f_c and either a or b.

5.3.5 Force ratio contours

The force ratio contours are defined as the critical force for the reverse transformation $f_{B\to A} = f_2$ divided by the critical force for the forward transformation $f_{A\to B} = f_1$.

$$\phi = \frac{f_2}{f_1} \tag{5.26}$$

The subscripts 1 and 2 in this case do not correspond to a destabilization and re-stabilization point at a constant critical load like they do for Γ_M, Γ_N and Γ_O. Instead, the subscripts correspond to two separate critical destabilization points at the reverse and forward transformations. The reason the definition uses f_1 in the denominator is that it will always be larger than zero. In contrast, f_2 at the reverse transformation may shift to zero at Γ_E and then negative for superplastic responses. Positive ϕ means the response is superelastic. Approaching $\phi = 1$ the SE hysteresis loop shrinks in width. At $\phi = 1$ this is the same condition as Γ_S, when $f_2 = f_1$. At $\phi = 0$ this is when $f_2 = 0$ reducing the ϕ conditions to Γ_E. Negative ϕ are superplastic. As ϕ goes from 1 to 0 to negative values the load difference between the forward and reverse transformation increases. The most negative ϕ are the widest hysteresis loops.

The conditions for ϕ are related to Γ_S. Equation 5.26 is rearranged

$$f_2 = \phi f_1 \tag{5.27}$$

The conditions for the for force ratio contours are then

$$\phi: \quad g_1(x_1, y_1, f_{c1}, a, b) = 0 \tag{5.28}$$

$$g_2(x_1, y_1, f_{c1}, a, b) = 0 \tag{5.29}$$

$$g_3(x_1, y_1, f_{c1}, a, b) = 0 \tag{5.30}$$

$$g_1(x_2, y_2, f_{c2} = \phi f_{c1}, a, b) = 0 \tag{5.31}$$

$$g_2(x_2, y_2, f_{c2} = \phi f_{c1}, a, b) = 0 \tag{5.32}$$

$$g_3(x_2, y_2, f_{c2} = \phi f_{c1}, a, b) = 0 \tag{5.33}$$

The system parameters a and b are the phase diagram axes. They are frequently used as running variables. A value of ϕ is fixed at the beginning of the program reducing the number of unknowns. The six equations are sufficient to solve for the six unknowns: x_1, x_2, y_1, y_2, f_{c1} and either a or b.

5.4 Engineering potential phase diagrams

Complete phase diagrams for the engineering potential are created

1. $r = 0.10$, $s = 0$
2. $r = 0.25$, $s = 0$
3. $r = 0.25$, $s = 0.25$
4. $r = 0.30$, $s = 0.5$

The Green strain phase diagram is drawn with the same scale as the first three diagrams ($8b$ across and $0.10a$ tall). The diagram for $r = 0.30$, $s = 0.5$ shows significant stretching of the

NESE region so it is plotted with a different scale. The geometry of the unit-cell at $s = 0.5$ has nice symmetry since all the bars are of the same length. Negative skewness is possible for a single unit-cell. It may be difficult to structure multiple negative skewness cells into a periodic lattice. Positive skewness and zero skewness unit-cells are more readily fabricated into periodic lattices or materials.

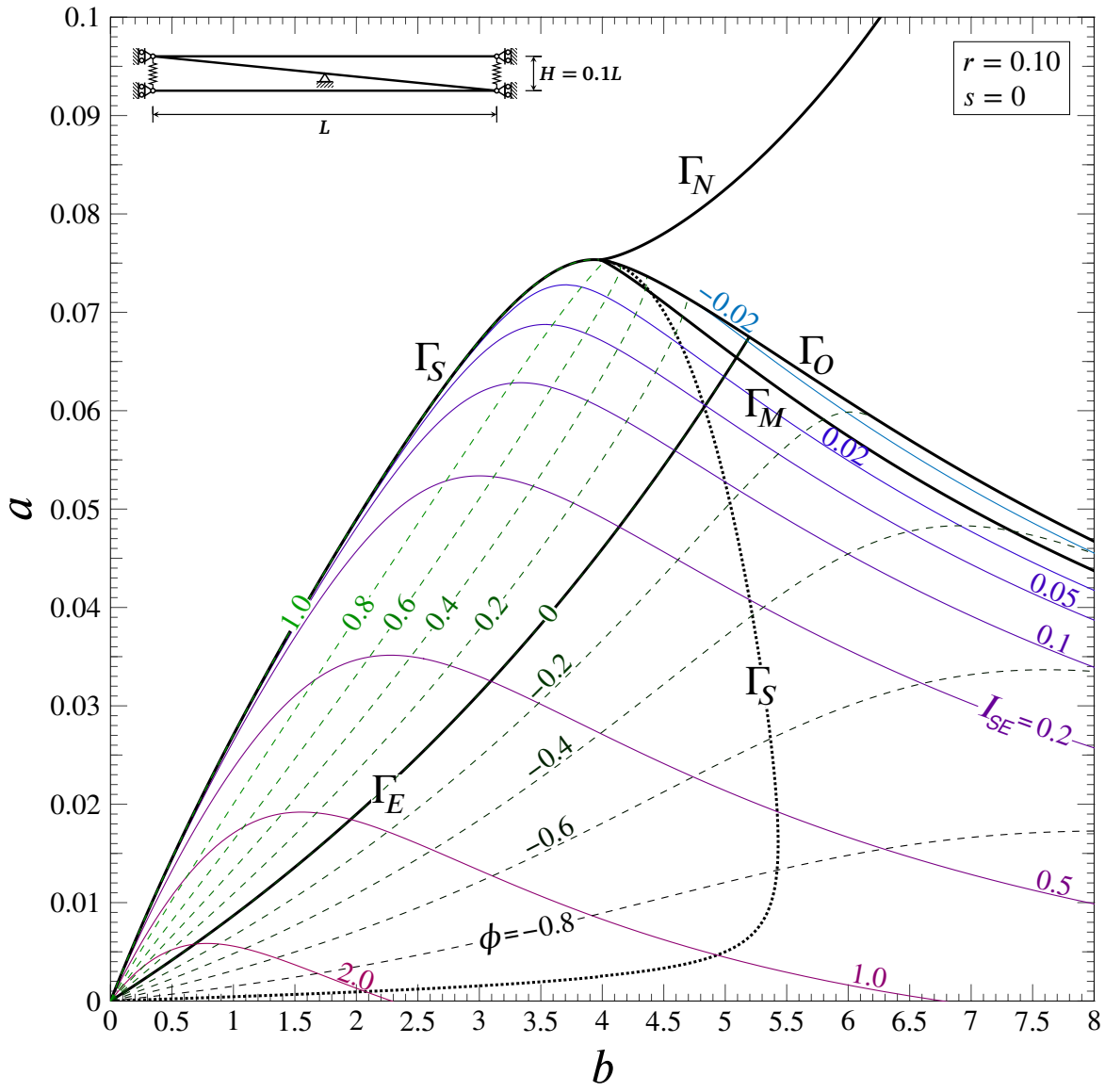

Figure 14: Phase diagram for $r = 0.10$, $s = 0$. The unit-cell is drawn to scale above. The bistability region is taller compared with the Green strain phase diagram. The boundary for the onset of the secondary tensile loop, the dotted Γ_S, goes to the origin. The maximal intensity of the contraction in the NESE region, which occurs at the triple point P_{EO}, is now less than the Green strain value due to nonzero aspect ratio r. For this unit-cell, at the triple point $(I_{NESE})_{\max} = -0.02897$.

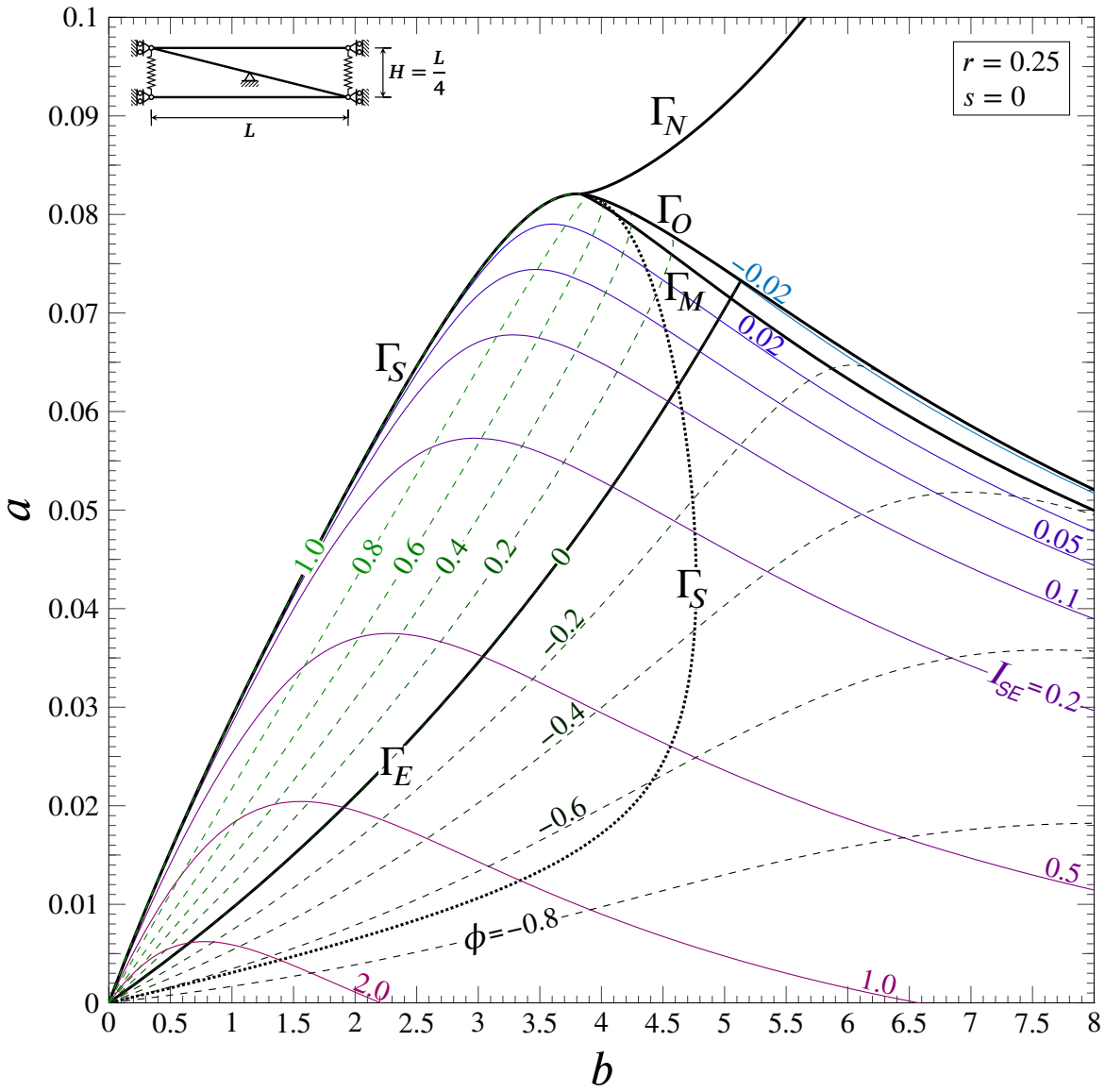

Figure 15: Phase diagram for $r = 0.25$, $s = 0$. The unit-cell is drawn to scale above. Qualitatively, it appears similar to the $r = 0.10$ case. The bistability region is even taller. The maximal intensity of I_{NESE} at P_{EO} is even less. For this unit-cell, $(I_{NESE})_{\max} = -0.02462$. Related to this effect is that the $I_{SE} = -0.02$ contour is shifted lower on the Γ_O curve.

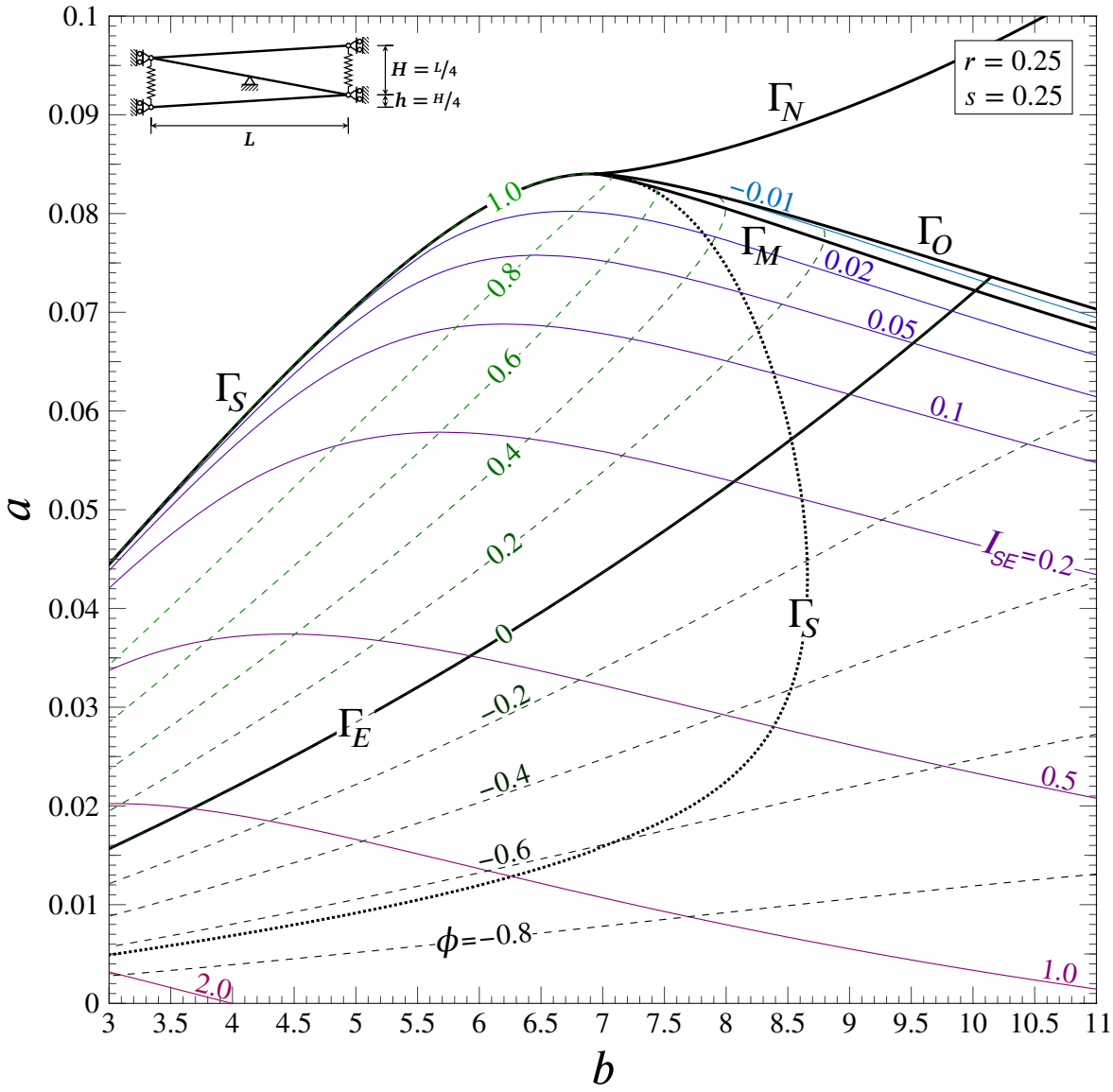

Figure 16: Phase diagram for $r = 0.25$, $s = 0.25$. The unit-cell is drawn to scale above. To capture the entire NESE region while maintaining the same axes scale, the b axis is shifted by 3. The nonzero skewness stretches the regions horizontally. The total area of the NESE region has doubled compared to the zero skewness case $r = 0.25$, $s = 0$. Positive skewness further decreases the maximal intensity of I_{NESE} at P_{EO}. For this unit-cell, $(I_{NESE})_{\max} = -0.02172$.

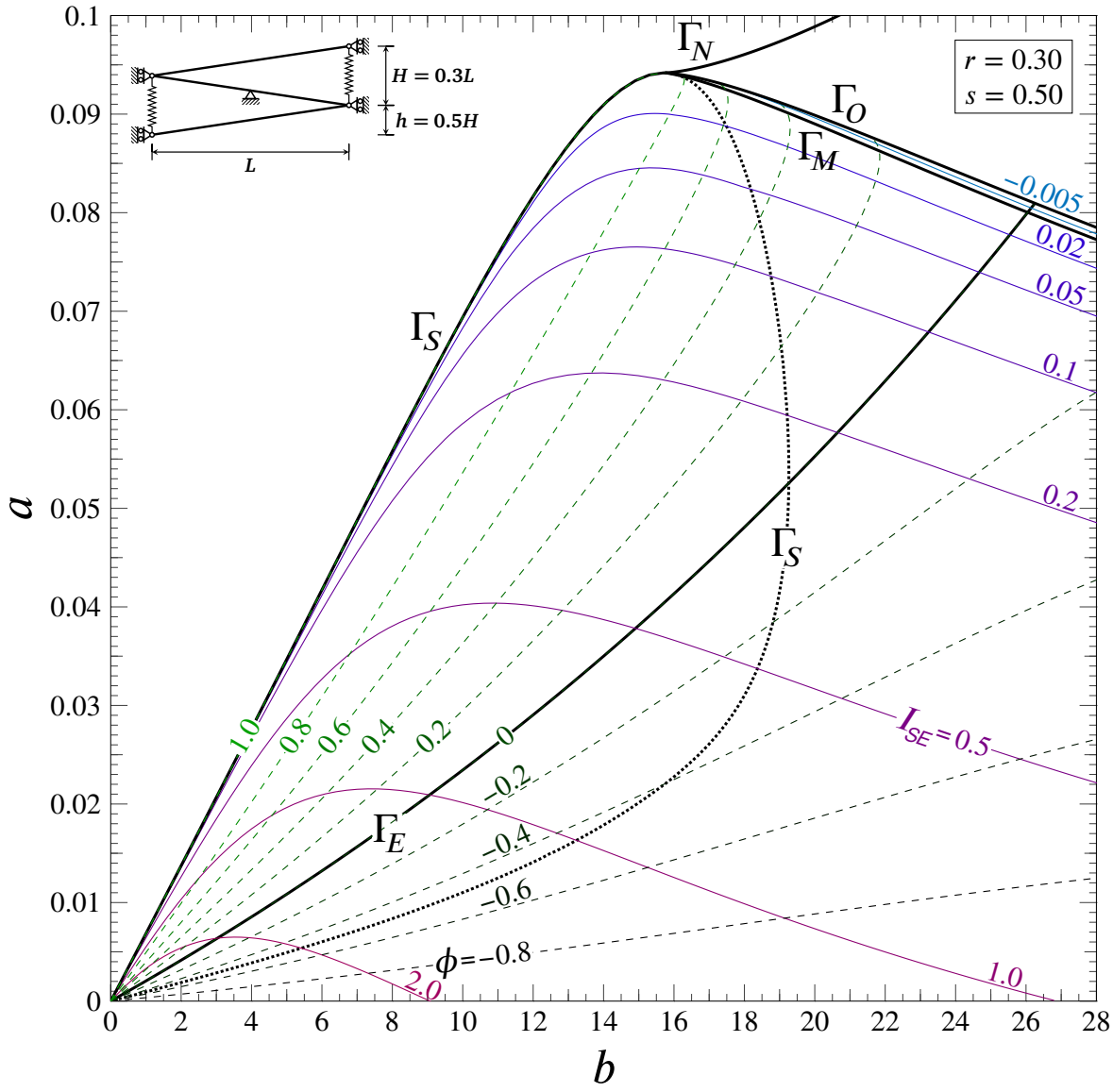

Figure 17: Phase diagram for $r = 0.30$, $s = 0.50$. The axes a and b are different from the previous four phase diagrams. The unit-cell is drawn to scale above. The three bars are all the same length using a skewness of 0.5. For this unit-cell, $(I_{NESE})_{\max} = -0.015076$.

5.4.1 Design example

To illustrate how to use the phase diagrams for the design of a unit-cell the following problem statement is given:

Design a unit-cell that has

- aspect ratio $r = 0.25$, skewness $s = 0.25$
- contraction of 5 mm with an intensity $I_{SE} = -0.01$,
- force ratio $\phi = f_2/f_1 = 0.2$ at a critical load $F_1 = 1000$ N

The intersection of $I_{SE} = -0.01$ and $\phi = 0.2$ could be calculated exactly using combined conditions for ϕ and I_{SE}. In the interest of time, each contour was least-squares fit to a polynomial only taking into account points near to the intersection. The intersection point of the two polynomials was calculated as $b = 8.78415$, $a = 0.078507$. This agrees with $\phi = 0.2$ and $I_{SE} = -0.01$ to 3 significant figures. Also at this point, $f_1 = 1.2371$, $\varepsilon_1 = 2.0219$ and $\varepsilon_2 = 2.00169$.

dimensional system parameters : $k_1, k_2, k_3, H, h, L, F_1, u_1, u_2$ (9 total)

known quantities : $r = 0.25$ (5.34)

$$s = 0.25 \tag{5.35}$$

$$a = 0.0.078507 \tag{5.36}$$

$$b = 8.78415 \tag{5.37}$$

$$F_1 = 1000 \text{ N} \tag{5.38}$$

$$f_1 = 1.2371 \tag{5.39}$$

$$\varepsilon_1 = 2.0219 \tag{5.40}$$

$$\varepsilon_2 = 2.0016 \tag{5.41}$$

$$\Delta u = 5 \text{ mm} \tag{5.42}$$

Equations:

$$r = \frac{H}{L} = 0.25 \tag{5.43}$$

$$s = \frac{h}{H} = 0.25 \tag{5.44}$$

$$a = \frac{k_2}{4k_3}\frac{H^2}{L^2} = 0.078507 \tag{5.45}$$

$$b = \frac{2k_1}{k_3}\frac{H^2}{H^2 + L^2} = 8.78415 \tag{5.46}$$

$$f_1 = \frac{F_1}{k_3 H} = 1.2371 \tag{5.47}$$

$$F = 1000 \text{ N} \tag{5.48}$$

$$\Delta u = u_1 - u_2 = 0.005 \text{ m} \tag{5.49}$$

$$\varepsilon_1 = \frac{u_1}{H} = 2.0219 \tag{5.50}$$

$$\varepsilon_2 = \frac{u_2}{H} = 2.0016 \tag{5.51}$$

The system is fully determined. There are 9 equations to solve for the 9 dimensional quantities.

Solution

Solving for u_1

$$u_1 = 0.005 \text{ m} + u_2 \tag{5.52}$$

Substitute for u_1 and solve for u_2 and H

$$\frac{0.005 \text{ m} + u_2}{H} = 2.0219 \tag{5.53}$$

$$\frac{u_2}{H} = 2.0016 \tag{5.54}$$

Displacement after the contraction u_2

$$u_2 = 0.4930 \text{ m} \tag{5.55}$$

Height H

$$H = 0.2463 \text{ m} \tag{5.56}$$

Displacement before the contraction u_1

$$u_1 = 2.0219H \tag{5.57}$$

$$= 0.4980 \text{ m} \tag{5.58}$$

Length L

$$L = \frac{H}{r} \tag{5.59}$$

$$= \frac{0.2463 \text{ m}}{0.25} \tag{5.60}$$

$$= 0.9852 \text{ m} \tag{5.61}$$

Skew offset h

$$h = sH \tag{5.62}$$

$$= 0.25 \cdot 0.2463 \text{ m} \tag{5.63}$$

$$= 0.061575 \text{ m} \tag{5.64}$$

Spring stiffness k_3

$$k_3 = \frac{F_1}{1.2371H} \tag{5.65}$$

$$= \frac{1000 \text{ N}}{1.2371 \cdot 0.2463 \text{ m}} \tag{5.66}$$

$$= 3281.94 \text{ N/m} \tag{5.67}$$

Middle bar stiffness k_1

$$k_1 = 8.78415 \cdot \frac{k_3}{2} \cdot \frac{H^2 + L^2}{H^2} \tag{5.68}$$

$$= 8.78415 \cdot \frac{3281.94 \text{ N/m}}{2} \cdot \frac{(0.2463 \text{ m})^2 + (0.9852 \text{ m})^2}{(0.2463 \text{ m})^2} \tag{5.69}$$

$$= 245,047 \text{ N/m} \tag{5.70}$$

Top and bottom bar stiffness k_2

$$k_2 = 0.078507 \cdot \frac{4k_3L^2}{H^2} \tag{5.71}$$

$$= 0.078507 \cdot \frac{4(3281.94 \text{ N/m})(0.9852 \text{ m})^2}{(0.2463 \text{ m})^2} \tag{5.72}$$

$$= 16,490 \text{ N/m} \tag{5.73}$$

The requirements: $r = 0.25$, skewness $s = 0.25$, $\Delta u = 5$ mm, $I_{SE} = -0.01$, $\phi = 0.2$ and $F_1 = 1000$ N are realized with the following unit-cell properties:

$H = 0.2463$ m, $L = 0.9852$ m, $h = 0.061575$ m,

$k_1 = 245,047$ N/m, $k_2 = 16,490$ N/m, $k_3 = 3281.94$ N/m

5.4.2 Triple point

The phase diagrams possess a singular point, which will be defined as the 'triple point.' The triple point P_{EO} marks the intersection of Γ_E and Γ_O. The coalescence curve Γ_O divides monostability from NESE or NESP. The superelasticity-superplasticity curve Γ_E divides NESP from NESE (or SP from SE). At the triple point the structure holds conditions for NESE, NESP and MS. To arrive mathematically at the triple point, a system of equations is set up using the three Γ_E conditions and the five Γ_O conditions. The system parameters a and b are the same across all equations. The point P_{EO} has an a and b that satisfy the conditions:

$$\underline{P_{EO}}$$

$$\Gamma_O: \quad g_1(x_1, y_1, f_{c1}, a, b) = 0 \tag{5.74}$$

$$g_2(x_1, y_1, f_{c1}, a, b) = 0 \tag{5.75}$$

$$g_3(x_1, y_1, f_{c1}, a, b) = 0 \tag{5.76}$$

$$g_1(x_2 = x_1, y_2, f_{c2} = f_{c1}, a, b) = 0 \tag{5.77}$$

$$g_2(x_2 = x_1, y_2, f_{c2} = f_{c1}, a, b) = 0 \tag{5.78}$$

$$\Gamma_E: \quad g_1(x_E, y_E, f_E = 0, a, b) = 0 \tag{5.79}$$

$$g_2(x_E, y_E, f_E = 0, a, b) = 0 \tag{5.80}$$

$$g_3(x_E, y_E, f_E = 0, a, b) = 0 \tag{5.81}$$

A force-response curve approaching this point from the NESE region is graphed in Figure 18 (a). Approaching P_{EO}, the intensity of the superelastic contraction is a maximum when con-

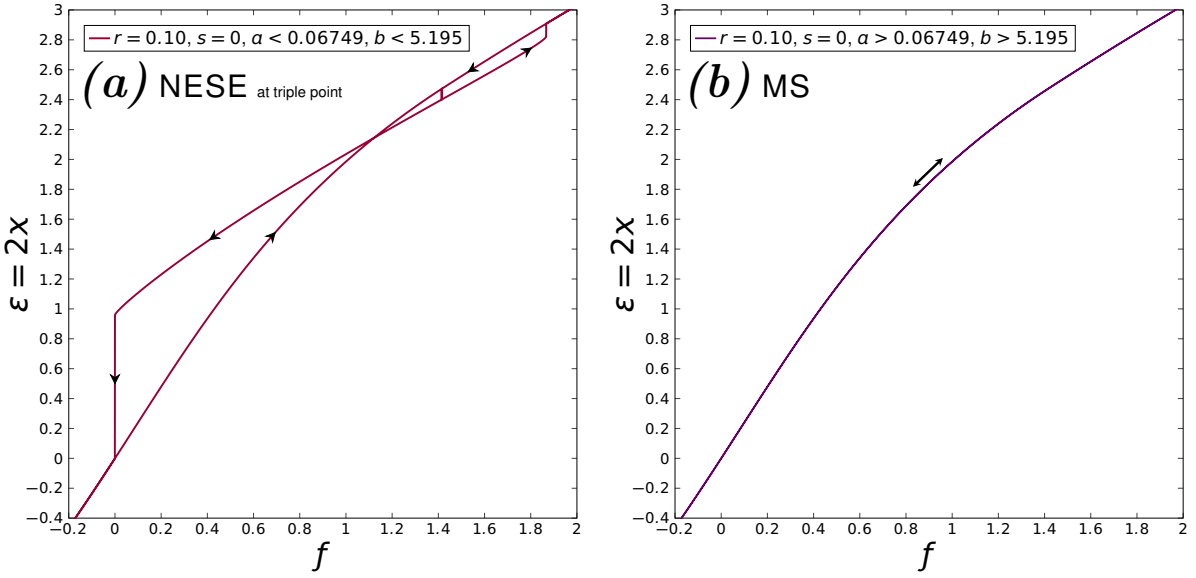

Figure 18: Triple point force-response curves for $r = 0.10$, $s = 0$. (a): Negative extensibility response is achieved when subtracting $1e{-}9$ from design parameters a and b at the triple point, $P_{EO} = (a = 0.06749, b = 5.195)$. The triple point is the maximal intensity for the superelastic contraction in the NESE region $(I_{NESE})_{\max}$. (b): Monostable response is achieved if the design parameters a and b at the triple point are each increased by $1e{-}9$.

sidering only the NESE response. More intense contractions are possible for NESP, especially when close to Γ_O with decreasing a. I_{NESE} is the same definition as I_{SE}. The subscript implies that only force-response curves in the NESE region are considered.

$$\text{at } P_{EO}: \quad I_{NESE} = (I_{NESE})_{\max} \tag{5.82}$$

The maximum intensity of I_{NESE} is used as a metric for comparing phase diagrams of different aspect ratio and skewness. Table 3 shows when $s = 0$, the Green strain case $r \to 0$ has the greatest magnitude I_{NESE} at the triple point. Using the Green strain approximation leads to a structure with small height compared to length. This flat structure is impractical. Nevertheless, it is useful as the theoretical limit by which to compare other unit-cell arrangements.

TABLE 3: I_{NESE} AT P_{EO}

r	s	I_{NESE} at triple point
$\to 0$	0	–0.0297439
0.0035	0	–0.0297430
0.01	0	–0.0297363
0.025	0	–0.0296963
0.05	0	–0.0295527
0.1	0	–0.0289693
0.25	0	–0.0246221
0.5	0	–0.0103181
0.7	0	–0.0013443

The effect of varying aspect ratio and skewness on I_{NESE} at the triple point is visualized in Figure 19. For skewness around $s = 0$, the maximum I_{NESE} is achieved as aspect ratio approaches zero. The plane curves in Figure 19 (left) are cross-sections of the three-dimensional r-s-I_{NESE} surface (right). Negative skewness alters the behavior at the triple point. The maximum intensity (a minimum in the plane curves) is achieved at an aspect ratio greater than zero.

The generation of the plane curves and the three-dimensional surface requires calculating the triple point as s and r are varied. Converged variables for the triple point define a critical load and a displacement. However, they will not show a difference between displacements x_1 and x_2 since $x_1 = x_2$ in the Γ_O conditions. Monostability merges with bistability at this fold-point. The exact triple point is not a NESE response. Moving infinitesimally towards the NESE region from the triple point there will be the maximum I_{NESE} effect. To get I_{NESE} at P_{EO}, a fraction $1e{-}9$ is subtracted off of P_{EO} design parameters a and b. A partial force-response curve is then generated near the critical load $f_{c,A\to B}$ at an extremely small step size Δf. The difference in the strain $\Delta\varepsilon_{A\to B}$ is then stored so as to calculate I_{NESE}. The entire process of calculating the s-r-I_{NESE} surface requires extreme attention to detail. The triple point conditions are highly

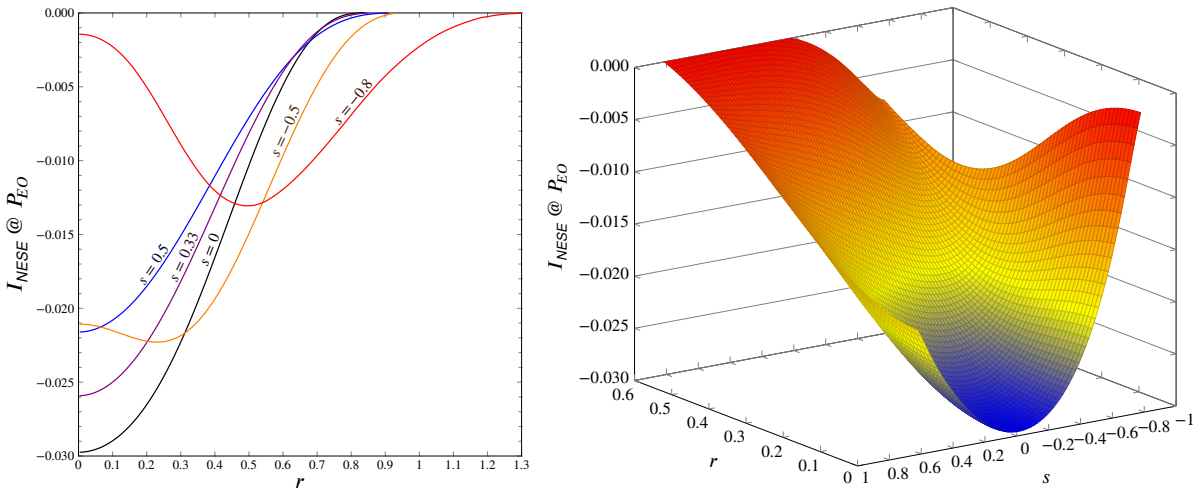

Figure 19: Intensity of superelastic strain I_{NESE} at triple point P_{EO} varying aspect ratio and skewness. (Left): plane curves of constant skewness showing how I_{NESE} changes with aspect ratio. (Right): Three-dimensional s-r-I_{NESE} surface. Unit-cells with skewness around $s = 0$ and low aspect ratio see the most pronounced I_{NESE}.

accurate. However, the values of I_{NESE} are calculated at a point extremely close to P_{EO} rather than the true converged triple point.

5.4.3 NESE region

The NESE region is defined by the boundaries Γ_O, Γ_M and Γ_E. At the branching region, Γ_M actually forms an extremely fine parabola, changes slope from negative to positive and then merges with Γ_S and Γ_O. The coalescence curve Γ_O is continuous with the NESE boundary Γ_M. Three intersection points are defined: the triple point P_{EO}, the simultaneous onset of NESE, NESP from SE, SP—the point P_{EM}, and the simultaneous formation and critical collapse of a NESE hysteresis loop—the point P_{OS}. In some phase diagrams, Γ_M intersects with the dotted Γ_S towards the top part of the NESE region. In these diagrams there exists a small region of NESE where there is a single NESE hysteresis loop with two-fold $A \to B \to A$ switching.

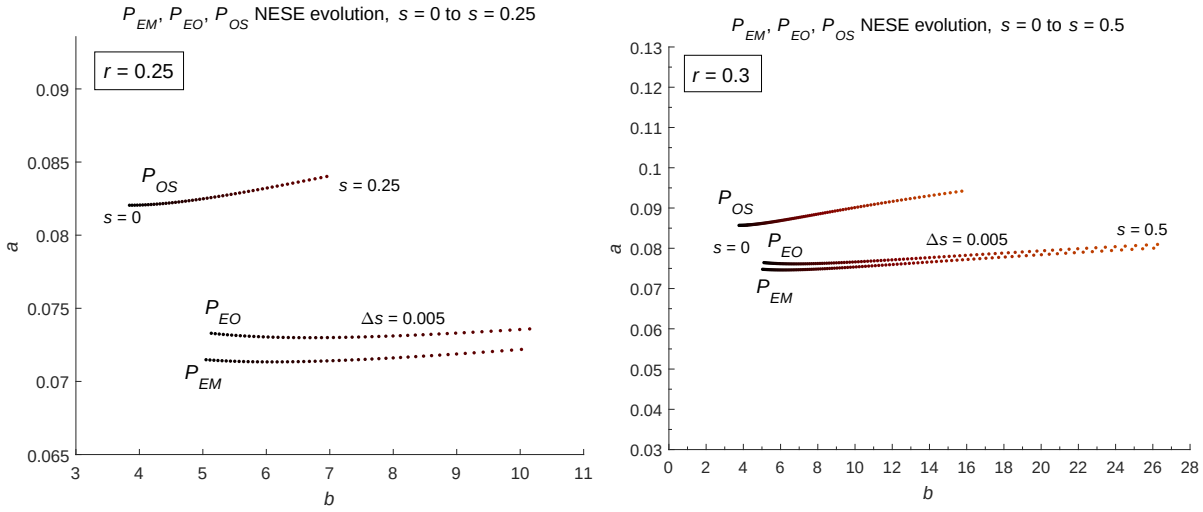

Figure 20: The NESE region is tracked by varying s. (Left): The change in the three points P_{EM}, P_{EO} and P_{OS} as s goes from 0 to 0.25 at constant $r = 0.25$. Complete phase diagrams are shown at each extreme. (Right): Change in the NESE region as s is increased from 0 to 0.5. A complete phase diagram is given for the skewed structure. Skewness causes significant distortion of the NESE region. *[Both graphs use the same axes ratio].*

However, for the skewed unit-cells the secondary hysteresis loop is always is present alongside pinched hysteresis. Therefore, only the three points are used to track the NESE region.

Conditions to calculate P_{EM} are identical to P_{EO}. Whether P_{EM} or P_{EO} is reached depends on the initial guess for the unknowns. The conditions for P_{OS} are combined conditions for Γ_O (5 equations) and Γ_S (6 equations). The parameters a and b are the same across all equations.

$\underline{P_{OS}}$

$$\Gamma_O: \quad g_1(x_1, y_1, f_{c1}, a, b) = 0 \tag{5.83}$$

$$g_2(x_1, y_1, f_{c1}, a, b) = 0 \tag{5.84}$$

$$g_3(x_1, y_1, f_{c1}, a, b) = 0 \tag{5.85}$$

$$g_1(x_2 = x_1, y_2, f_{c2} = f_{c1}, a, b) = 0 \tag{5.86}$$

$$g_2(x_2 = x_1, y_2, f_{c2} = f_{c1}, a, b) = 0 \tag{5.87}$$

$$\Gamma_S: \quad g_1(x_{1S}, y_{1S}, f_{1S}, a, b) = 0 \tag{5.88}$$

$$g_2(x_{1S}, y_{1S}, f_{1S}, a, b) = 0 \tag{5.89}$$

$$g_3(x_{1S}, y_{1S}, f_{1S}, a, b) = 0 \tag{5.90}$$

$$g_1(x_{2S}, y_{2S}, f_{2S} = f_{1S}, a, b) = 0 \tag{5.91}$$

$$g_2(x_{2S}, y_{2S}, f_{2S} = f_{1S}, a, b) = 0 \tag{5.92}$$

$$g_3(x_{2S}, y_{2S}, f_{2S} = f_{1S}, a, b) = 0 \tag{5.93}$$

Once a solution is found for an intersection point there is less trial and error if the same type of intersection point is desired for different r and s. An iterative program was constructed to gradually increment r and s using the converged solutions from the previous iteration as the initial guess for a new r and s. Using this technique, the evolution of the NESE region with changing r and s is possible to track. The drift of the NESE region as a function of s at

constant r is shown in Figure 20. The effect of negative skewness and the effect changing r at constant s are shown in Figure 21.

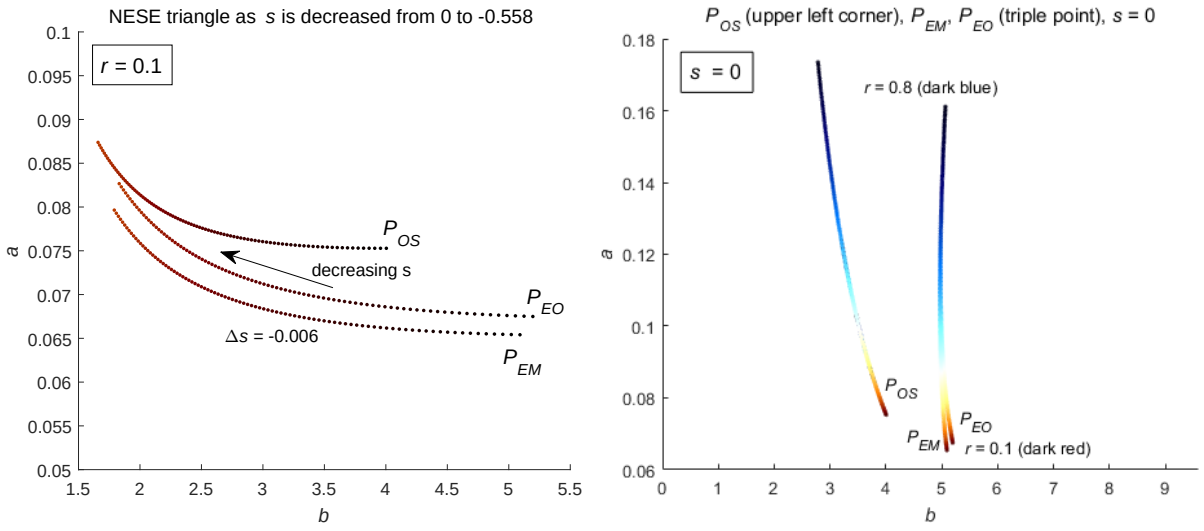

Figure 21: Drift of the NESE region. (Left): Effect of negative skewness on the NESE region at constant $r = 0.10$. (Right): Change in the NESE region as r is increased from 0 to 0.5. The effect of aspect ratio is a vertical shift and thinning of the NESE region. *[Both graphs use the same axes ratio, 8b:0.1a].*

CHAPTER 6

MATERIALS

Two- and three-dimensional arrays of elastic elements are now being referred to as materials [46,142]. Advances in rapid prototyping allow for the fabrication of elastic structures composed of spring and bar elements. In general, the term 'material' is used as a way of denoting a structure with specific mechanical properties derived from its unit-cell structure [143]. The negative extensibility unit-cell structure can be organized into a periodic array. Periodic (Born–von Karmon) boundary conditions are to be applied. The unit-cell response is defined by the system parameters a, b, r and s. A periodic structure composed of multiple unit-cell structures is shown to exhibit a similar response as its unit-cell constituent.

6.0.1 Two unit-cell structure

In lattice mechanics, the convention is adopted where the nodal column index $i = 1, 2 \dots M$ and the nodal row index $j = 1, 2 \dots N$. Nodes are labeled $i.j$ where i is the column and j is the row index. Figure 22 is a two unit-cell structure with periodic boundary conditions applied. Independent displacement degrees of freedom are shown below. There is a new translational degree of freedom u_{21}, which was not present in the single unit-cell. This type of horizontal degree of freedom will be more prevalent in larger structures. It may be problematic to achieving a uniform NESE effect. As discussed by Lakes [94], there must be sufficient constraint to facilitate negative incremental stiffness in foam cells and rubber tubes. When multiple cells are taken

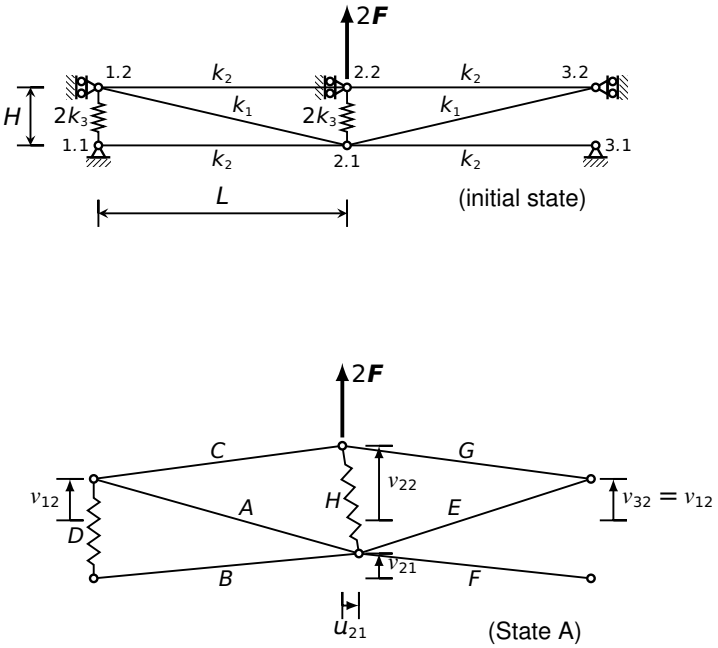

Figure 22: Two unit-cells $M = 3$ nodal columns, $N = 2$ nodal rows. Periodic boundary conditions are applied.

together the constraint becomes insufficient. A similar phenomenon may occur for large arrays of negative extensibility unit-cells.

For the two unit-cell structure, the response is similar to its constituent $r = 0.25$, $s = 0$ unit-cell. Figure 23 is the force-response curve of the two-unit cell structure when inputting parameters a and b near to the triple point for its constituent unit-cell. In other words, elastic member stiffness and geometry for the structure are defined based on the unit-cell phase diagram. The force-response curve is fully dimensional. The strain ε, which is a function of the external degrees of freedom, is normalized so that it is comparable to a single unit-cell. Since there are 3 nodal columns $M = 3$ strain is $\varepsilon = 2(v_{12} + v_{22})/(3H)$.

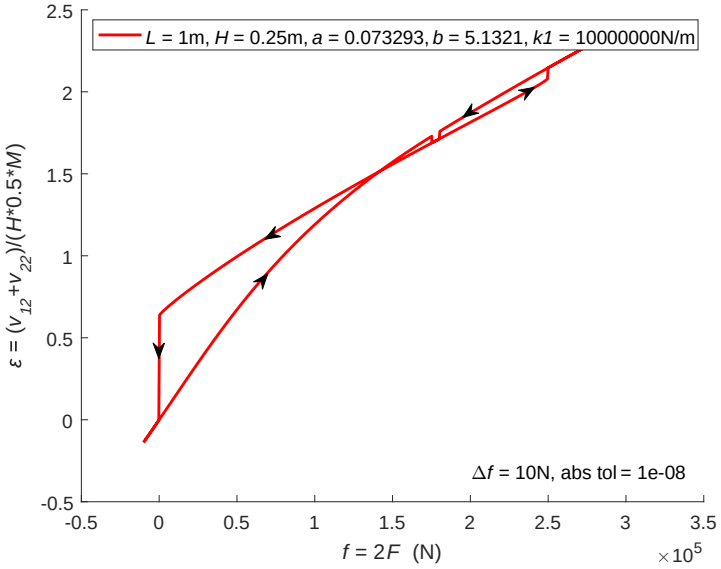

Figure 23: Force-response curve for the two unit-cell structure. The response is the same as the constituent unit-cell. System parameters are $r = 0.25$, $s = 0$, $a = a^{PEO} - 1e{-}7$ and $b = b^{PEO} - 1e{-}3$. A fraction is subtracted from each of the triple point system parameters. This is below and to the left of the triple point in the $r = 0.25$, $s = 0$ phase diagram. The point is inside the NESE region.

When using the dimensional quantities there are free variables to be fixed. The length was taken to be $L = 1$ m and the middle bar stiffness $k_1 = 1e7$ N/m. All other parameters are then defined based on $r = 0.25$, $s = 0$, a and b. The strain energy stored each of the elements are defined

$$P_A = \frac{k_1}{2}\left(\sqrt{(L+u_{21})^2 + (H + v_{12} - v_{21})^2} - \sqrt{L^2+H^2}\right)^2 \tag{6.1}$$

$$P_B = \frac{k_2}{2}\left(\sqrt{(L+u_{21})^2 + (v_{21})^2} - L\right)^2 \tag{6.2}$$

$$P_C = \frac{k_2}{2}\left(\sqrt{L^2 + (v_{22} - v_{12})^2} - L\right)^2 \tag{6.3}$$

$$P_D = k_3(v_{12})^2 \tag{6.4}$$

$$P_E = \frac{k_1}{2}\left(\sqrt{(L-u_{21})^2 + (H + v_{32} - v_{21})^2} - \sqrt{L^2+H^2}\right)^2 \tag{6.5}$$

$$P_F = \frac{k_2}{2}\left(\sqrt{(L-u_{21})^2 + (v_{21})^2} - L\right)^2 \tag{6.6}$$

$$P_G = \frac{k_2}{2}\left(\sqrt{L^2 + (v_{32} - v_{22})^2} - L\right)^2 \tag{6.7}$$

$$P_H = k_3\left(\sqrt{(u_{21})^2 + (H + v_{22} - v_{21})^2} - H\right)^2 \tag{6.8}$$

Finally, the total potential takes into account the strain energy less the energy of the external load

$$\Pi = P_A + P_B + P_C + P_D + P_E + P_F + P_G + P_H - 2Fv_{22} \tag{6.9}$$

The degrees of freedom are defined component-wise. At node 2.1, there is a vertical and horizontal degree of freedom v_{21} and u_{21}. There are two more independent vertical displacements, v_{22} and v_{12}. The degree of freedom $v_{32} = v_{12}$ as a result of the periodic boundary requirement.

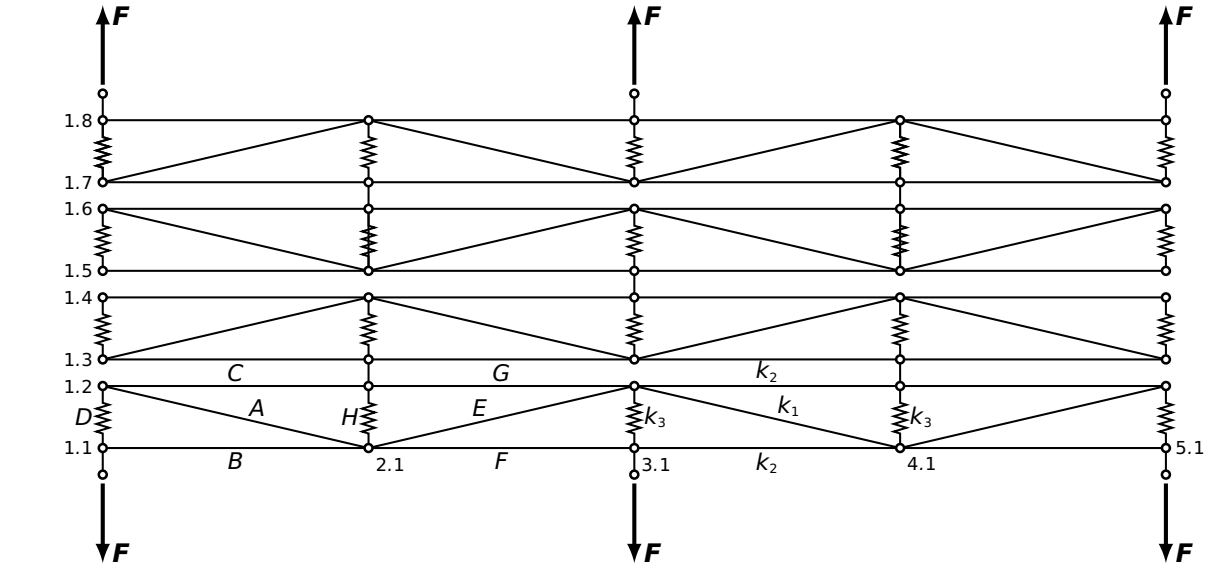

(a)

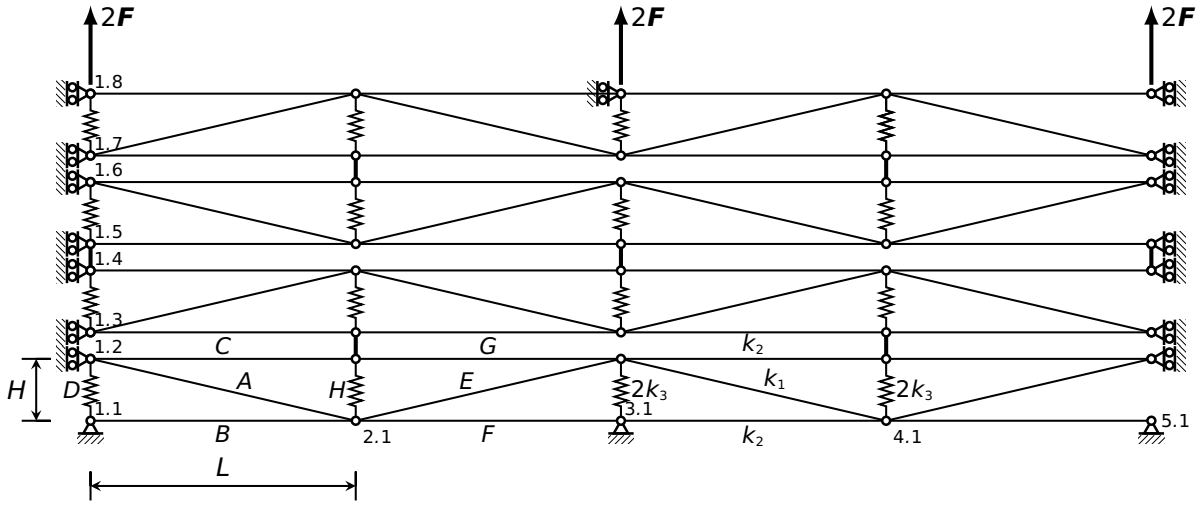

(b)

Figure 24: Array $M = 5$ nodal columns across and $N = 8$ nodal rows tall. There are 16 unit-cell structures. (a): Force boundary conditions applied on either end of the material. (b): Periodic boundary conditions. Rigid connections are between unit-cells layers.

6.0.2 Potential for periodic array

The two-unit cell potential and boundary conditions can be derived from more general statements which apply to periodic arrays with an odd number of column indices, M = odd. From the larger periodic array $M = 5$, $N = 8$ in Figure 24, the potentials A–H of eight elastic members are defined component-by-component

$$P_A = \frac{k_1}{2}\left(\sqrt{(L + u_{i+1,j} - u_{i,j+1})^2 + (H + v_{i,j+1} - v_{i+1,j})^2} - \sqrt{L^2 + H^2}\right)^2$$

$$P_B = \frac{k_2}{2}\left(\sqrt{(L + u_{i+1,j} - u_{i,j})^2 + (v_{i+1,j} - v_{i,j})^2} - L\right)^2$$

$$P_C = \frac{k_2}{2}\left(\sqrt{(L + u_{i+1,j+1} - u_{i,j+1})^2 + (v_{i+1,j+1} - v_{i,j+1})^2} - L\right)^2$$

$$P_D = k_3\left(\sqrt{(u_{i,j+1} - u_{i,j})^2 + (H + v_{i,j+1} - v_{i,j})^2} - H\right)^2$$

$$P_E = \frac{k_1}{2}\left(\sqrt{(L + u_{i+2,j+1} - u_{i+1,j})^2 + (H + v_{i+2,j+1} - v_{i+1,j})^2} - \sqrt{L^2 + H^2}\right)^2$$

$$P_F = \frac{k_2}{2}\left(\sqrt{(L + u_{i+2,j} - u_{i+1,j})^2 + (v_{i+2,j} - v_{i+1,j})^2} - L\right)^2$$

$$P_G = \frac{k_2}{2}\left(\sqrt{(L + u_{i+2,j+1} - u_{i+1,j+1})^2 + (v_{i+2,j+1} - v_{i+1,j+1})^2} - L\right)^2$$

$$P_H = k_3\left(\sqrt{(u_{i+1,j+1} - u_{i+1,j})^2 + (H + v_{i+1,j+1} - v_{i+1,j})^2} - H\right)^2$$

The potential energy due to external forces for this set of eight strain energy functions is

$$V = -6Fv_{1,8} \tag{6.10}$$

The total potential will be

$$\Pi = U - V$$

6.0.3 Periodic boundary conditions

The following periodic boundary conditions work for an odd number of columns $M = \text{odd}$.

1. Fixed degrees of freedom
   - left and right columns vertical rollers
   - bottom row, odd columns are pinned
   - top row, odd columns vertical rollers
2. The leftmost and rightmost columns have equal displacements for a given row
3. Nodes at rigid connections have identical displacements
4. Nodes with applied external forces all have equal vertical displacements

For $M = 5$ columns and $N = 8$ rows the following boundary conditions are generated

$$\begin{pmatrix} 0 & u_{2,8} & 0 & u_{4,8} & 0 \\ 0 & u_{2,6} & u_{3,7} & u_{4,6} & 0 \\ 0 & u_{2,6} & u_{3,6} & u_{4,6} & 0 \\ 0 & u_{2,5} & u_{3,4} & u_{4,5} & 0 \\ 0 & u_{2,4} & u_{3,4} & u_{4,4} & 0 \\ 0 & u_{2,2} & u_{3,3} & u_{4,2} & 0 \\ 0 & u_{2,2} & u_{3,2} & u_{4,2} & 0 \\ 0 & u_{2,1} & 0 & u_{4,1} & 0 \end{pmatrix} \quad \begin{pmatrix} v_{1,8} & v_{2,8} & v_{1,8} & v_{4,8} & v_{1,8} \\ v_{1,7} & v_{2,6} & v_{3,7} & v_{4,6} & v_{1,7} \\ v_{1,6} & v_{2,6} & v_{3,6} & v_{4,6} & v_{1,6} \\ v_{1,4} & v_{2,5} & v_{3,4} & v_{4,5} & v_{1,4} \\ v_{1,4} & v_{2,4} & v_{3,4} & v_{4,4} & v_{1,4} \\ v_{1,3} & v_{2,2} & v_{3,3} & v_{4,2} & v_{1,3} \\ v_{1,2} & v_{2,2} & v_{3,2} & v_{4,2} & v_{1,2} \\ 0 & v_{2,1} & 0 & v_{4,1} & 0 \end{pmatrix}$$

In the future, a program will be developed to set up independent degrees of freedom, boundary conditions and the necessary equations based on an arbitrary number of rows and columns of nodes.

6.1 Conclusion

Fabrication of materials that retain the property of negative extension may be impractical due to several factors. There will always be imperfections and variations in materials. Variability or imperfection may suppress the energetic driving force for the contraction. A large NESE region may be able to compensate for some degree of variation in elastic member properties. A major factor that would hinder the NESE response in a periodic structure is the loss of constraint. Stacking more and more unit-cells vertically and horizontally adds additional, undesirable degrees of freedom that are not associated with a contraction. Additional translational degrees of freedom and possibly other modes in real materials like bending or twisting may render the concept physically unattainable. The goal is to have all constituent units in the structure move in a concerted fashion. This seems unlikely. An expected outcome is that some of the unit-cells may destabilize and contract prematurely while others may destabilize and re-equilibrate too late. The contraction would behave in a step-like pattern.

Acknowledging potential shortcomings, there are certainly many upsides. Many of the analytical techniques developed here are transferable to other mechanical, material, structural and thermodynamic systems. The principles discussed here are integral to dynamic, nonlinear systems, especially those systems with multiple stable states [144, 145]. Dynamic analysis including the effect of damping, switching wave propagation, relaxation transients, and the effect of boundary conditions on the unit-cell may be a worthwhile pursuit. The ability to isolate regions of monostability from those of bistability is applicable to many situations. Catastrophe theory is a powerful predictive tool. In the unit-cell structure, the transition to bistability

may be smooth. A smooth transition from the region of monostability to bistability occurs when crossing over Γ_S. With increasing b, the hysteresis loop starts off from a point and grows wider. Similarly, the transition across Γ_M from the SE bistable region and into the NESE region is smooth. Approaching Γ_M from the SE region, the intensity of the superelastic strain I_{SE} at the forward transformation $A \rightarrow B$ gradually decreases to zero and then goes increasingly negative once inside the NESE region. The hysteresis loop slowly pinches in on itself. However, when crossing over Γ_O from the NESE or NESP regions, the response switches suddenly to monostability. This a catastrophic change in the equilibrium response.

A significant result is the visualization of the mechanical response of the structure in the form of a phase diagram. The development of physical relationships based on dimensionless quantities is widespread across engineering [146]. The Buckingham π theorem provides a systematic way of computing dimensionless parameters. An example is given in Appendix B. Later studies will apply the methods developed here to other mechanical and material systems. Tetragonal or diamond-shaped structures are strong candidates for unit-cell structures capable of exhibiting a contraction. Previous work on tetragonal networks of beams showed negative compressibility in certain dimensions [100, 147]. Cubic crystal structures in general have the most exotic effects such as the most negative and the most positive Poisson's effects [21, 118].

APPENDICES

Appendix A

NON-DIMENSIONALIZATION OF THE ENGINEERING (TRUE) POTENTIAL

A.1 Strain energy of each element

Bar 1

$$l_0 = \sqrt{L^2 + (H-h)^2}$$

$$l_f = \sqrt{L^2 + (H-h-2v)^2}$$

$$\Delta l_1 = \sqrt{L^2 + (H-h-2v)^2} - \sqrt{L^2 + (H-h)^2}$$

$$\pi_1 = \frac{1}{2}k_1 \Delta l_1^2 = \frac{1}{2}k_1 \left(\sqrt{L^2 + (H-h-2v)^2} - \sqrt{L^2 + (H-h)^2} \right)^2 \tag{A.1}$$

Bar 2

$$l_0 = \sqrt{L^2 + h^2}$$

$$l_f = \sqrt{L^2 + (h+u+v)^2}$$

$$\Delta l_2 = \sqrt{L^2 + (h+u+v)^2} - \sqrt{L^2 + h^2}$$

$$\pi_2 = \frac{1}{2}k_2 \Delta l_2^2 = \frac{1}{2}k_2 \left(\sqrt{L^2 + (h+u+v)^2} - \sqrt{L^2 + h^2} \right)^2 \tag{A.2}$$

Appendix A (Continued)

Spring 3

$$l_0 = H$$

$$l_f = H + u - v$$

$$\Delta l_3 = u - v$$

$$\pi_3 = \frac{1}{2} k_3 \Delta l_3^2 = \frac{1}{2} k_3 (u - v)^2 \tag{A.3}$$

The stored strain energy in the bars k_1 and k_2 and the spring k_3

$$\pi_1 = \frac{1}{2} k_1 \left(\sqrt{L^2 + (H - h - 2v)^2} - \sqrt{L^2 + (H - h)^2} \right)^2 \tag{A.4}$$

$$\pi_2 = \frac{1}{2} k_2 \left(\sqrt{L^2 + (h + u + v)^2} - \sqrt{L^2 + h^2} \right)^2 \tag{A.5}$$

$$\pi_3 = \frac{1}{2} k_3 (u - v)^2 \tag{A.6}$$

A.2 Balance of energy

Fully dimensional potential

$$\Pi = U - V = \pi_1 + 2(\pi_2 + \pi_3 - Fu) \tag{A.7}$$

$$\begin{aligned} \Pi = {} & \frac{1}{2} k_1 \left(\sqrt{L^2 + (H - h - 2v)^2} - \sqrt{L^2 + (H - h)^2} \right)^2 \\ & + k_2 \left(\sqrt{L^2 + (h + u + v)^2} - \sqrt{L^2 + h^2} \right)^2 + k_3 (u - v)^2 - 2Fu \end{aligned} \tag{A.8}$$

Appendix A (Continued)

A.3 Non-dimensionalization

The following dimensionless parameters are used

system (design) parameters: $a = \frac{k_2}{4k_3}\frac{H^2}{L^2+H^2}, \quad b = \frac{2k_1}{k_3}\frac{H^2}{L^2+(H-h)^2},$

$r = \frac{H}{L}, \quad s = \frac{h}{H}$

independent state parameters: $x = \frac{u}{H}, \quad y = \frac{v}{H}$

control parameter: $f = \frac{F}{k_3 H}$

dimensionless potential: $U = \frac{\Pi}{k_3 H^2}$

Appendix A (Continued)

Non-dimensionalize the first term corresponding to π_1

$$\pi_1 = \frac{1}{2}k_1\left(\sqrt{L^2+(H-h-2v)^2}-\sqrt{L^2+(H-h)^2}\right)^2 \tag{A.9}$$

$$\phi_1 = \frac{\pi_1}{k_3H^2} \tag{A.10}$$

$$= \frac{1}{2}\frac{k_1}{k_3H^2}\left(\sqrt{L^2+(H-h-2v)^2}-\sqrt{L^2+(H-h)^2}\right)^2 \tag{A.11}$$

$$= \frac{k_1}{2k_3H^2}\left(\sqrt{H^2\frac{L^2}{H^2}+H^2\left(\frac{H}{H}-\frac{h}{H}-2\frac{v}{H}\right)^2}-\sqrt{H^2\frac{L^2}{H^2}+H^2\left(\frac{H}{H}-\frac{h}{H}\right)^2}\right)^2 \tag{A.12}$$

$$= \frac{k_1H^2}{2k_3H^2}\left(\sqrt{\frac{L^2}{H^2}+\left(1-\frac{h}{H}-2\frac{v}{H}\right)^2}-\sqrt{\frac{L^2}{H^2}+\left(1-\frac{h}{H}\right)^2}\right)^2 \tag{A.13}$$

$$= \frac{k_1}{2k_3}\left(\frac{4H^2}{4H^2}\right)\left(\frac{L^2+(H-h)^2}{L^2+(H-h)^2}\right) \times\left(\sqrt{\frac{L^2}{H^2}+\left(1-\frac{h}{H}-2\frac{v}{H}\right)^2}-\sqrt{\frac{L^2}{H^2}+\left(1-\frac{h}{H}\right)^2}\right)^2 \tag{A.14}$$

$$= \left(\frac{2k_1}{k_3}\frac{H^2}{(L^2+(H-h)^2}\right)\left(\frac{L^2+(H-h)^2}{4H^2}\right) \times\left(\sqrt{\frac{L^2}{H^2}+\left(1-\frac{h}{H}-2\frac{v}{H}\right)^2}-\sqrt{\frac{L^2}{H^2}+\left(1-\frac{h}{H}\right)^2}\right)^2 \tag{A.15}$$

$$= \left(\frac{2k_1}{k_3}\frac{H^2}{(L^2+(H-h)^2}\right)\frac{1}{4}\left(\frac{h^2}{H^2}-2\frac{h}{H}+\frac{L^2}{H^2}+1\right) \times\left(\sqrt{\frac{L^2}{H^2}+\left(1-\frac{h}{H}-2\frac{v}{H}\right)^2}-\sqrt{\frac{L^2}{H^2}+\left(1-\frac{h}{H}\right)^2}\right)^2 \tag{A.16}$$

Substitute the dimensionless parameters

$$\boxed{\phi_1 = \frac{b}{4}\left(s^2-2s+\frac{1}{r^2}+1\right)\left(\sqrt{\frac{1}{r^2}+(1-s-2y)^2}-\sqrt{\frac{1}{r^2}+(1-s)^2}\right)^2} \tag{A.17}$$

which is equivalent to

$$\phi_1 = \frac{b}{4r^2}\left(s^2-2s+\frac{1}{r^2}+1\right)\left(\sqrt{1+(r-sr-2ry)^2}-\sqrt{1+(r-sr)^2}\right)^2 \tag{A.18}$$

Appendix A (Continued)

Non-dimensionalize the second term corresponding to π_2

$$2\pi_2 = k_2\left(\sqrt{L^2+(h+u+v)^2}-\sqrt{L^2+h^2}\right)^2 \tag{A.19}$$

$$\phi_2 = \frac{2\pi_2}{k_3H^2} \tag{A.20}$$

$$= \frac{k_2}{k_3H^2}\left(\sqrt{H^2\frac{L^2}{H^2}+H^2\left(\frac{h}{H}+\frac{u}{H}+\frac{v}{H}\right)^2}-\sqrt{H^2\frac{L^2}{H^2}+H^2\frac{h^2}{H^2}}\right)^2 \tag{A.21}$$

$$= \frac{k_2H^2}{k_3H^2}\left(\sqrt{\frac{L^2}{H^2}+\left(\frac{h}{H}+\frac{u}{H}+\frac{v}{H}\right)^2}-\sqrt{\frac{L^2}{H^2}+\frac{h^2}{H^2}}\right)^2 \tag{A.22}$$

$$= \frac{k_2}{k_3}\left(\frac{4H^2}{4H^2}\right)\left(\frac{L^2+h^2}{L^2+h^2}\right)\left(\sqrt{\frac{L^2}{H^2}+\left(\frac{h}{H}+\frac{u}{H}+\frac{v}{H}\right)^2}-\sqrt{\frac{L^2}{H^2}+\frac{h^2}{H^2}}\right)^2 \tag{A.23}$$

$$= \left(\frac{k_2}{4k_3}\frac{H^2}{L^2+h^2}\right)\left(\frac{4\left(L^2+h^2\right)}{H^2}\right)\left(\sqrt{\frac{L^2}{H^2}+\left(\frac{h}{H}+\frac{u}{H}+\frac{v}{H}\right)^2}-\sqrt{\frac{L^2}{H^2}+\frac{h^2}{H^2}}\right)^2 \tag{A.24}$$

$$= 4\left(\frac{k_2}{4k_3}\frac{H^2}{L^2+h^2}\right)\left(\frac{h^2}{H^2}+\frac{L^2}{H^2}\right)\left(\sqrt{\frac{L^2}{H^2}+\left(\frac{h}{H}+\frac{u}{H}+\frac{v}{H}\right)^2}-\sqrt{\frac{L^2}{H^2}+\frac{h^2}{H^2}}\right)^2 \tag{A.25}$$

Substitute dimensionless parameters

$$\boxed{\phi_2 = 4a\left(s^2+\frac{1}{r^2}\right)\left(\sqrt{\frac{1}{r^2}+(s+x+y)^2}-\sqrt{\frac{1}{r^2}+s^2}\right)^2} \tag{A.26}$$

which is equivalent to

$$\phi_2 = \frac{4a}{r^2}\left(s^2+\frac{1}{r^2}\right)\left(\sqrt{1+(sr+xr+yr)^2}-\sqrt{1+s^2r^2}\right)^2 \tag{A.27}$$

Non-dimensionalize the second term corresponding to π_3

$$2\pi_3 = k_3(u-v)^2 \tag{A.28}$$

$$\phi_3 = \frac{2\pi_3}{k_3H^2} \tag{A.29}$$

$$= \frac{k_3H^2}{k_3H^2}\left(\frac{u}{H}-\frac{v}{H}\right)^2 \tag{A.30}$$

Appendix A (Continued)

Substitute dimensionless parameters

$$\boxed{\phi_3 = (x-y)^2} \tag{A.31}$$

Non-dimensionalize the fourth term corresponding to the control parameter f

$$2Fu = 2F\frac{u}{H}H \tag{A.32}$$

$$\phi_4 = 2\frac{F}{k_3 H}\frac{u}{H} \tag{A.33}$$

Substitute dimensionless parameters

$$\boxed{\phi_4 = 2fx} \tag{A.34}$$

The dimensionless terms are

$$\phi_1 = \frac{b}{4}\left(s^2 - 2s + \frac{1}{r^2} + 1\right)\left(\sqrt{\frac{1}{r^2} + (1-s-2y)^2} - \sqrt{\frac{1}{r^2} + (1-s)^2}\right)^2 \tag{A.35}$$

$$= \frac{b}{4r^2}\left(s^2 - 2s + \frac{1}{r^2} + 1\right)\left(\sqrt{1 + (r-sr-2ry)^2} - \sqrt{1 + (r-sr)^2}\right)^2 \tag{A.36}$$

$$\phi_2 = 4a\left(s^2 + \frac{1}{r^2}\right)\left(\sqrt{\frac{1}{r^2} + (s+x+y)^2} - \sqrt{\frac{1}{r^2} + s^2}\right)^2 \tag{A.37}$$

$$= \frac{4a}{r^2}\left(s^2 + \frac{1}{r^2}\right)\left(\sqrt{1 + (sr+xr+yr)^2} - \sqrt{1 + s^2r^2}\right)^2 \tag{A.38}$$

$$\phi_3 = (x-y)^2 \tag{A.39}$$

$$\phi_4 = 2fx \tag{A.40}$$

Appendix A (Continued)

A.4 Dimensionless Balance of energy

$$
\begin{aligned}
U = {} & 4a\left(s^2+\frac{1}{r^2}\right)\left(\sqrt{\frac{1}{r^2}+(s+x+y)^2}-\sqrt{\frac{1}{r^2}+s^2}\right)^2 \\
& +\frac{b}{4}\left(s^2-2s+\frac{1}{r^2}+1\right)\left(\sqrt{\frac{1}{r^2}+(1-s-2y)^2}-\sqrt{\frac{1}{r^2}+(1-s)^2}\right)^2 \\
& +(x-y)^2-2fx
\end{aligned}
\tag{A.41}
$$

Compared to the dimensional balance of energy below

$$
\begin{aligned}
\Pi = {} & \frac{1}{2}k_1\left(\sqrt{L^2+(H-h-2v)^2}-\sqrt{L^2+(H-h)^2}\right)^2 \\
& +k_2\left(\sqrt{L^2+(h+u+v)^2}-\sqrt{L^2+h^2}\right)^2+k_3\left(u-v\right)^2-2Fu
\end{aligned}
\tag{A.42}
$$

Appendix B

DIMENSIONAL ANALYSIS

B.1 Buckingham Pi Theorem

B.1.1 Definitions and problem statement

Balance of energy:

$$\begin{aligned}\Pi &= U - V \\ &= \pi_1 + 2(\pi_2 + \pi_3 - Fu) \\ &= \frac{1}{2}k_1\left(\sqrt{L^2 + (H-h-2v)^2} - \sqrt{L^2 + (H-h)^2}\right)^2 \\ &\quad + k_2\left(\sqrt{L^2 + (h+u+v)^2} - \sqrt{L^2 + h^2}\right)^2 + k_3\left(u - v\right)^2 - 2Fu\end{aligned} \tag{B.1}$$

The total potential Π can be expressed as

$$\Pi = \phi_1(k_1, k_2, k_3, L, H, h, u, v, F)$$

or

$$0 = \phi(\Pi, k_1, k_2, k_3, L, H, h, u, v, F) \tag{B.2}$$

There are 10 variables of interest in the problem. The dimensions in the problem are mass, length and time (M, L and T) or alternatively force, length and time (F, L and T) can be used.

Appendix B (Continued)

Energy, Π $\left[\frac{\text{kg}\cdot\text{m}^2}{\text{s}^2}\right]$, ML^2T^{-2} or FL

Stiffness, k $\left[\frac{\text{kg}}{\text{s}^2}\right]$, MT^{-2} or FL^{-1}

Distance, H, L, h, u, v $[\text{m}]$, L

Force, F $\left[\frac{\text{kg}\cdot\text{m}}{\text{s}^2}\right]$, MLT^{-2} or F

1ST π THEOREM:

The **m** variables in the problem can be redefined in terms of **m**−**n** dimensionless parameters or π groups. The quantity **n** is the set of SI base units (such as mass, length and time) needed to express the **m** variables.

2ND π THEOREM:

The dimensionless groups π are functions of both the **n** repeating or governing variables and the original variables **n**.

B.1.2 Determination of repeating variables

Rules are as follows:

1. There can be **n** repeating variables.
2. In combination, the repeating variables consist of all SI base units (MLT or FLT). Individual repeating variables do not have to contain all dimensions.
3. The repeating variables when combined cannot form a dimensionless group.
4. Repeating variables are not required to show up in each π group.

Appendix B (Continued)

5. Repeating variables represent essential design parameters and should be measurable through experiment.

B.1.3 Pi groups in the problem

The balance of energy

$0 = \phi(\Pi, k_1, k_2, k_3, L, H, h, u, v, F)$

Only force F and length L, $\mathbf{n} = 2$, are taken as the dimensions needed to reproduce the repeating variables. Time (or mass) does not show up explicitly in the potential because the analysis is quasistatic. The number of dimensional variables is $\mathbf{m} = 10$ so there are $\mathbf{m}-\mathbf{n} = 8$ π groups.

$$\phi(\pi_1, \pi_2, \pi_3, \pi_4, \pi_5, \pi_6, \pi_7, \pi_8) = 0 \tag{B.3}$$

Choose stiffness $\boldsymbol{k_3}$ and height $\boldsymbol{H}$ as the repeating variables. Seven groups are formed

$$\pi_1 = k_3^{a_1} H^{b_1} \Pi \tag{B.4}$$

$$\pi_2 = k_3^{a_2} H^{b_2} k_1 \tag{B.5}$$

$$\pi_3 = k_3^{a_3} H^{b_3} k_2 \tag{B.6}$$

$$\pi_4 = k_3^{a_4} H^{b_4} L \tag{B.7}$$

$$\pi_5 = k_3^{a_5} H^{b_5} u \tag{B.8}$$

$$\pi_6 = k_3^{a_6} H^{b_6} v \tag{B.9}$$

$$\pi_7 = k_3^{a_7} H^{b_7} F \tag{B.10}$$

$$\pi_8 = k_3^{a_8} H^{b_8} h \tag{B.11}$$

All π groups are dimensionless $F^0 L^0$. π group dimensions are related using the principal of dimensional homogeneity.

Appendix B (Continued)

Below is an example for developing the first π group

$\underline{\pi_1}$

$\pi_1 = k_3^{a_1} H^{b_1} \Pi$

SI units

$1 = \left(\mathrm{N} \cdot \mathrm{m}^{-1}\right)^{a_1} (\mathrm{m})^{b_1} (\mathrm{N} \cdot \mathrm{m})$

in terms of dimensions

$F^0 L^0 = \left(FL^{-1}\right)^{a_1} (L)^{b_1} (FL)$

for F : $\quad 0 = a_1 + 1$

for L : $\quad 0 = -a_1 + b_1 + 1$

$a_1 = -1, \quad b_1 = -2$

The first π group is

$$\pi_1 = k_3^{-1} H^{-2} \Pi = \frac{\Pi}{k_3 H^2} \tag{B.12}$$

Appendix B (Continued)

Overall, the π groups are defined as

$$\pi_1 = \frac{\Pi}{k_3 H^2} \tag{B.13}$$

$$\pi_2 = \frac{2k_1}{k_3}\frac{H^2}{L^2 + (H-h)^2} \tag{B.14}$$

$$\pi_3 = \frac{k_2}{4k_3}\frac{H^2}{L^2 + H^2} \tag{B.15}$$

$$\pi_4 = \frac{L}{H} \tag{B.16}$$

$$\pi_5 = \frac{u}{H} \tag{B.17}$$

$$\pi_6 = \frac{v}{H} \tag{B.18}$$

$$\pi_7 = \frac{F}{k_3 H} \tag{B.19}$$

$$\pi_8 = \frac{h}{H} \tag{B.20}$$

The original expression can be written in terms of the 7 dimensionless π groups

$$0 = \phi(\Pi, k_1, k_2, k_3, L, H, u, v, F, h) \tag{B.21}$$

$$0 = \phi(\pi_1, \pi_2, \pi_3, \pi_4, \pi_5, \pi_6, \pi_7, \pi_8) \tag{B.22}$$

$$0 = \phi\left(\frac{\Pi}{k_3 H^2}, \frac{2k_1}{k_3}\frac{H^2}{L^2 + (H-h)^2}, \frac{k_2}{4k_3}\frac{H^2}{L^2 + H^2}, \frac{H}{L}, \frac{u}{H}, \frac{v}{H}, \frac{F}{k_3 H}, \frac{h}{H}\right) \tag{B.23}$$

Assigning π groups to variables

$$0 = \phi\left(U, b, a, r, x, y, f, s\right) \tag{B.24}$$

Appendix B (Continued)

The π groups are

$$
\begin{aligned}
U = \pi_1 &= \frac{\Pi}{k_3 H^2} \\
b = \pi_2 &= \frac{k_2}{4k_3}\frac{H^2}{L^2+H^2} \\
a = \pi_3 &= \frac{2k_1}{k_3}\frac{H^2}{L^2+(H-h)^2} \\
r = \pi_4 &= \frac{H}{L} \\
x = \pi_5 &= \frac{u}{H} \\
y = \pi_6 &= \frac{v}{H} \\
f = \pi_7 &= \frac{F}{k_3 H} \\
s = \pi_8 &= \frac{h}{H}
\end{aligned}
\tag{B.25}
$$

Since there are **m**= 10 dimensional variables and **n**= 8 π groups, two dimensional quantities must be fixed before the system is fully dimensional. In the design example, the critical force $f_1 = 1000$ N and the change in strain $\Delta\varepsilon_c = 1$ mm were fixed. A similar situation was encountered when using the fully dimensional potential for the two unit-cell structure. Here the length $L = 1$ m and the stiffness $k_1 = 1\text{e}7$ N/m were fixed before generating the force-response curve.

CITED LITERATURE

[1] Viktor G Veselago. The electrodynamics of substances with simultaneously negative values of ε and μ. *Soviet physics uspekhi*, 10(4):509, 1968.

[2] JB Pendry, AJ Holden, WJ Stewart, and I Youngs. Extremely low frequency plasmons in metallic mesostructures. *Physical review letters*, 76(25):4773, 1996.

[3] JB Pendry, AJ Holden, DJ Robbins, and WJ Stewart. Low frequency plasmons in thin-wire structures. *Journal of Physics: Condensed Matter*, 10(22):4785, 1998.

[4] Richard A Shelby, David R Smith, and Seldon Schultz. Experimental verification of a negative index of refraction. *Science*, 292(5514):77–79, 2001.

[5] David R Smith, John B Pendry, and Mike CK Wiltshire. Metamaterials and negative refractive index. *Science*, 305(5685):788–792, 2004.

[6] David R Smith, Willie J Padilla, DC Vier, Syrus C Nemat-Nasser, and Seldon Schultz. Composite medium with simultaneously negative permeability and permittivity. *Physical review letters*, 84(18):4184, 2000.

[7] John Brian Pendry. Negative refraction makes a perfect lens. *Physical review letters*, 85(18):3966, 2000.

[8] John B Pendry, David Schurig, and David R Smith. Controlling electromagnetic fields. *science*, 312(5781):1780–1782, 2006.

[9] Tolga Ergin, Nicolas Stenger, Patrice Brenner, John B Pendry, and Martin Wegener. Three-dimensional invisibility cloak at optical wavelengths. *Science*, 328(5976):337–339, 2010.

[10] David Schurig, JJ Mock, BJ Justice, Steven A Cummer, John B Pendry, AF Starr, and DR Smith. Metamaterial electromagnetic cloak at microwave frequencies. *Science*, 314(5801):977–980, 2006.

[11] Ricardo Marqués, Francisco Mesa, Jesus Martel, and Francisco Medina. Comparative analysis of edge-and broadside-coupled split ring resonators for metamaterial

design-theory and experiments. *IEEE Transactions on Antennas and Propagation*, 51(10):2572–2581, 2003.

[12] Peter W Milonni. *Fast light, slow light and left-handed light*. CRC Press, 2004.

[13] Christophe Caloz and Tatsuo Itoh. *Electromagnetic metamaterials: transmission line theory and microwave applications*. John Wiley & Sons, 2005.

[14] AV Kabashin, P Evans, S Pastkovsky, W Hendren, GA Wurtz, R Atkinson, R Pollard, VA Podolskiy, and AV Zayats. Plasmonic nanorod metamaterials for biosensing. *Nature materials*, 8(11):867–871, 2009.

[15] Yang Wang, Tianyi Sun, Trilochan Paudel, Yi Zhang, Zhifeng Ren, and Krzysztof Kempa. Metamaterial-plasmonic absorber structure for high efficiency amorphous silicon solar cells. *Nano letters*, 12(1):440–445, 2011.

[16] DR Smith, DC Vier, Th Koschny, and CM Soukoulis. Electromagnetic parameter retrieval from inhomogeneous metamaterials. *Physical review E*, 71(3):036617, 2005.

[17] R Liu, C Ji, JJ Mock, JY Chin, TJ Cui, and DR Smith. Broadband ground-plane cloak. *Science*, 323(5912):366–369, 2009.

[18] Th Koschny, P Markoš, Eleftherios N Economou, DR Smith, DC Vier, and CM Soukoulis. Impact of inherent periodic structure on effective medium description of left-handed and related metamaterials. *Physical Review B*, 71(24):245105, 2005.

[19] Ari Sihvola. Metamaterials in electromagnetics. *Metamaterials*, 1(1):2–11, 2007.

[20] EA Friis, RS Lakes, and JB Park. Negative poisson's ratio polymeric and metallic foams. *Journal of Materials Science*, 23(12):4406–4414, 1988.

[21] Ray H Baughman, Justin M Shacklette, Anvar A Zakhidov, and Sven Stafström. Negative poisson's ratios as a common feature of cubic metals. *Nature*, 392(6674):362–365, 1998.

[22] Jensen Li and CT Chan. Double-negative acoustic metamaterial. *Physical Review E*, 70(5):055602, 2004.

[23] HH Huang, CT Sun, and GL Huang. On the negative effective mass density in acoustic metamaterials. *International Journal of Engineering Science*, 47(4):610–617, 2009.

[24] Laurent Nicolas, M Furstoss, and Marie-Annick Galland. Analogy electromagnetism-acoustics: Validation and application to local impedance active control for sound absorption. *The European Physical Journal Applied Physics*, 4(1):95–100, 1998.

[25] Y Cheng, JY Xu, and XJ Liu. One-dimensional structured ultrasonic metamaterials with simultaneously negative dynamic density and modulus. *Physical Review B*, 77(4):045134, 2008.

[26] Zixian Liang and Jensen Li. Extreme acoustic metamaterial by coiling up space. *Physical review letters*, 108(11):114301, 2012.

[27] Roderic S Lakes, T Lee, A Bersie, and YC Wang. Extreme damping in composite materials with negative-stiffness inclusions. *Nature*, 410(6828):565–567, 2001.

[28] T Jaglinski, D Kochmann, D Stone, and RS Lakes. Composite materials with viscoelastic stiffness greater than diamond. *Science*, 315(5812):620–622, 2007.

[29] Zhengyou Liu, Xixiang Zhang, Yiwei Mao, YY Zhu, Zhiyu Yang, Che Ting Chan, and Ping Sheng. Locally resonant sonic materials. *science*, 289(5485):1734–1736, 2000.

[30] Ping Sheng, Rongfu Xiao, Weijia Wen, and Zheng You Liu. Composite materials with negative elastic constants, June 10 2003. US Patent 6,576,333.

[31] Jensen Li, Lee Fok, Xiaobo Yin, Guy Bartal, and Xiang Zhang. Experimental demonstration of an acoustic magnifying hyperlens. *Nature materials*, 8(12):931–934, 2009.

[32] Jie Zhu, Johan Christensen, Jesper Jung, Luis Martin-Moreno, X Yin, Lee Fok, Xiang Zhang, and FJ Garcia-Vidal. A holey-structured metamaterial for acoustic deep-subwavelength imaging. *Nature physics*, 7(1):52–55, 2011.

[33] Steven A Cummer and David Schurig. One path to acoustic cloaking. *New Journal of Physics*, 9(3):45, 2007.

[34] Mohamed Farhat, Stefan Enoch, Sébastien Guenneau, and AB Movchan. Broadband cylindrical acoustic cloak for linear surface waves in a fluid. *Physical review letters*, 101(13):134501, 2008.

[35] Z Yang, HM Dai, NH Chan, GC Ma, and Ping Sheng. Acoustic metamaterial panels for sound attenuation in the 50–1000 hz regime. *Applied Physics Letters*, 96(4):041906, 2010.

[36] Zhiyu Yang, Jun Mei, Min Yang, NH Chan, and Ping Sheng. Membrane-type acoustic metamaterial with negative dynamic mass. *Physical review letters*, 101(20):204301, 2008.

[37] Stéphane Brûlé, EH Javelaud, Stefan Enoch, and Sébastien Guenneau. Experiments on seismic metamaterials: Molding surface waves. *Physical review letters*, 112(13):133901, 2014.

[38] Kenneth E Evans and Andrew Alderson. Auxetic materials: functional materials and structures from lateral thinking! *Advanced materials*, 12(9):617–628, 2000.

[39] Zachary G Nicolaou and Adilson E Motter. Mechanical metamaterials with negative compressibility transitions. *Nature materials*, 11(7):608–613, 2012.

[40] Zachary G Nicolaou and Adilson E Motter. Longitudinal inverted compressibility in super-strained metamaterials. *Journal of Statistical Physics*, 151(6):1162–1174, 2013.

[41] Jae-Hwang Lee, Jonathan P Singer, and Edwin L Thomas. Micro-/nanostructured mechanical metamaterials. *Advanced materials*, 24(36):4782–4810, 2012.

[42] Tiemo Bückmann, Nicolas Stenger, Muamer Kadic, Johannes Kaschke, Andreas Frölich, Tobias Kennerknecht, Christoph Eberl, Michael Thiel, and Martin Wegener. Tailored 3d mechanical metamaterials made by dip-in direct-laser-writing optical lithography. *Advanced Materials*, 24(20):2710–2714, 2012.

[43] Roderic Lakes. Foam structures with a negative poisson's ratio. *Science*, 235:1038–1041, 1987.

[44] Jin-Wu Jiang and Harold S Park. Negative poisson's ratio in single-layer black phosphorus. *arXiv preprint arXiv:1403.4326*, 2014.

[45] D Prall and RS Lakes. Properties of a chiral honeycomb with a poisson's ratio of1. *International Journal of Mechanical Sciences*, 39(3):305–314, 1997.

[46] Muamer Kadic, Tiemo Bückmann, Nicolas Stenger, Michael Thiel, and Martin Wegener. On the practicability of pentamode mechanical metamaterials. *Applied Physics Letters*, 100(19):191901, 2012.

[47] T Bückmann, M Thiel, M Kadic, R Schittny, and M Wegener. An elasto-mechanical unfeelability cloak made of pentamode metamaterials. *Nature communications*, 5, 2014.

[48] M Gorkunov and M Lapine. Tuning of a nonlinear metamaterial band gap by an external magnetic field. *Physical Review B*, 70(23):235109, 2004.

[49] AQ Liu, WM Zhu, DP Tsai, and Nikolay I Zheludev. Micromachined tunable metamaterials: a review. *Journal of Optics*, 14(11):114009, 2012.

[50] Scott Waitukaitis, Rémi Menaut, Bryan Gin-ge Chen, and Martin van Hecke. Origami multistability: From single vertices to metasheets. *Physical review letters*, 114(5):055503, 2015.

[51] Zhiyan Y Wei, Zengcai V Guo, Levi Dudte, Haiyi Y Liang, and L Mahadevan. Geometric mechanics of periodic pleated origami. *Physical review letters*, 110(21):215501, 2013.

[52] Charlotte Py, Paul Reverdy, Lionel Doppler, José Bico, Benoît Roman, and Charles N Baroud. Capillary origami: spontaneous wrapping of a droplet with an elastic sheet. *Physical review letters*, 98(15):156103, 2007.

[53] Marcelo A Dias, Levi H Dudte, L Mahadevan, and Christian D Santangelo. Geometric mechanics of curved crease origami. *Physical review letters*, 109(11):114301, 2012.

[54] Paul M Chaikin and Tom C Lubensky. *Principles of condensed matter physics*. Cambridge university press, 2000.

[55] Jesse L Silverberg, Arthur A Evans, Lauren McLeod, Ryan C Hayward, Thomas Hull, Christian D Santangelo, and Itai Cohen. Using origami design principles to fold reprogrammable mechanical metamaterials. *science*, 345(6197):647–650, 2014.

[56] Jungwook Kim, James A Hanna, Myunghwan Byun, Christian D Santangelo, and Ryan C Hayward. Designing responsive buckled surfaces by halftone gel lithography. *Science*, 335(6073):1201–1205, 2012.

[57] S Felton, M Tolley, E Demaine, D Rus, and R Wood. A method for building self-folding machines. *Science*, 345(6197):644–646, 2014.

[58] Ramses V Martinez, Carina R Fish, Xin Chen, and George M Whitesides. Elastomeric origami: programmable paper-elastomer composites as pneumatic actuators. *Advanced functional materials*, 22(7):1376–1384, 2012.

[59] H Okuzaki, T Saido, H Suzuki, Y Hara, and H Yan. A biomorphic origami actuator fabricated by folding a conducting paper. In *Journal of Physics: Conference Series*, volume 127, page 012001. IOP Publishing, 2008.

[60] JG Cai, YX Xu, J Feng, and J Zhang. Mechanical behaviour of bistable struts. *Proceedings of the Institution of Mechanical Engineers, Part C: Journal of Mechanical Engineering Science*, 226(5):1321–1325, 2012.

[61] Tyge Schioler and Sergio Pellegrino. Space frames with multiple stable configurations. *AIAA journal*, 45(7):1740–1747, 2007.

[62] Martin Hoffmann, Peter Kopka, and Edgar Voges. All-silicon bistable micromechanical fiber switch based on advanced bulk micromachining. *IEEE Journal of selected topics in quantum electronics*, 5(1):46–51, 1999.

[63] BD Jensen, LL Howell, and LG Salmon. Design of two-link, in-plane, bistable compliant micro-mechanisms. *Journal of Mechanical Design*, 121(3):416–423, 1999.

[64] Mattias Vangbo. An analytical analysis of a compressed bistable buckled beam. *Sensors and Actuators A: Physical*, 69(3):212–216, 1998.

[65] Samuel C Stanton, Clark C McGehee, and Brian P Mann. Nonlinear dynamics for broadband energy harvesting: Investigation of a bistable piezoelectric inertial generator. *Physica D: Nonlinear Phenomena*, 239(10):640–653, 2010.

[66] Kyung T Park. Piezoelectric snap action switch, May 24 1994. US Patent 5,315,204.

[67] A David Johnson and Curtis A Ray. Shape memory alloy film actuated microvalve, July 5 1994. US Patent 5,325,880.

[68] Bernhard Winzek, Sam Schmitz, Holger Rumpf, Tobias Sterzl, Ralf Hassdorf, Sigurd Thienhaus, Jürgen Feydt, Michael Moske, and Eckhard Quandt. Recent developments in shape memory thin film technology. *Materials Science and Engineering: A*, 378(1):40–46, 2004.

[69] Mauro Dolce and Donatello Cardone. Mechanical behaviour of shape memory alloys for seismic applications 1. martensite and austenite niti bars subjected to torsion. *International Journal of Mechanical Sciences*, 43(11):2631–2656, 2001.

[70] Gangbing Song, N Ma, and H-N Li. Applications of shape memory alloys in civil structures. *Engineering structures*, 28(9):1266–1274, 2006.

[71] Jordi Ortın and Lucas Delaey. Hysteresis in shape-memory alloys. *International Journal of Non-Linear Mechanics*, 37(8):1275–1281, 2002.

[72] Kazuhiro Otsuka and Clarence Marvin Wayman. *Shape memory materials*. Cambridge university press, 1999.

[73] L Catherine Brinson. One-dimensional constitutive behavior of shape memory alloys: thermomechanical derivation with non-constant material functions and redefined martensite internal variable. *Journal of intelligent material systems and structures*, 4(2):229–242, 1993.

[74] S Saadat, J Salichs, M Noori, Z Hou, H Davoodi, I Bar-On, Y Suzuki, and A Masuda. An overview of vibration and seismic applications of niti shape memory alloy. *Smart materials and structures*, 11(2):218, 2002.

[75] AJ Barnes. Superplastic forming 40 years and still growing. *Journal of Materials Engineering and Performance*, 16(4):440–454, 2007.

[76] Z Horita, M Furukawa, M Nemoto, AJ Barnes, and TG Langdon. Superplastic forming at high strain rates after severe plastic deformation. *Acta Materialia*, 48(14):3633–3640, 2000.

[77] Ying Zhao, Minoru Taya, Yansheng Kang, and Akira Kawasaki. Compression behavior of porous niti shape memory alloy. *Acta materialia*, 53(2):337–343, 2005.

[78] SX McFadden, Rajiv S Mishra, RZ Valiev, AP Zhilyaev, and AK Mukherjee. Low-temperature superplasticity in nanostructured nickel and metal alloys. *Nature*, 398(6729):684–686, 1999.

[79] Tai-Gang Nieh, Jeffrey Wadsworth, and Oleg D Sherby. *Superplasticity in metals and ceramics*. Cambridge university press, 2005.

[80] Wei Yang and Hongtao Wang. Mechanics modeling for deformation of nano-grained metals. *Journal of the Mechanics and Physics of Solids*, 52(4):875–889, 2004.

[81] Lian Lu, ML Sui, and Ke Lu. Superplastic extensibility of nanocrystalline copper at room temperature. *Science*, 287(5457):1463–1466, 2000.

[82] Yinmin Wang, Mingwei Chen, Fenghua Zhou, and En Ma. High tensile ductility in a nanostructured metal. *Nature*, 419(6910):912–915, 2002.

[83] Larry A Danso and Eduard G Karpov. Cusp singularity-based bistability criterion for geometrically nonlinear structures. *Extreme Mechanics Letters*, 2017.

[84] RI Leine and DH Van Campen. Discontinuous fold bifurcations in mechanical systems. *Archive of Applied Mechanics*, 72(2):138–146, 2002.

[85] E Christopher Zeeman. Catastrophe theory. *Scientific American*, 234(4):65–83, 1976.

[86] René Thom. Structural stability and morphogenesis, 1976.

[87] James AC Knowles, Mark H Lowenberg, Simon A Neild, and Bernd Krauskopf. A bifurcation study to guide the design of a landing gear with a combined uplock/downlock mechanism. In *Proc. R. Soc. A*, volume 470. The Royal Society, 2014.

[88] Claudio A Cañizares. Calculating optimal system parameters to maximize the distance to saddle-node bifurcations. *IEEE Transactions on Circuits and Systems I: Fundamental Theory and Applications*, 45(3):225–237, 1998.

[89] Olivier Thual and James C Mcwilliams. The catastrophe structure of thermohaline convection in a two-dimensional fluid model and a comparison with low-order box models. *Geophysical & Astrophysical Fluid Dynamics*, 64(1-4):67–95, 1992.

[90] John B Collings. Bifurcation and stability analysis of a temperature-dependent mite predator-prey interaction model incorporating a prey refuge. *Bulletin of mathematical biology*, 57(1):63–76, 1995.

[91] FE McCaughan. Bifurcation analysis of axial flow compressor stability. *SIAM Journal on Applied Mathematics*, 50(5):1232–1253, 1990.

[92] B Moore, T Jaglinski, DS Stone, and RS Lakes. Negative incremental bulk modulus in foams. *Philosophical magazine letters*, 86(10):651–659, 2006.

[93] R Lakes, P Rosakis, and A Ruina. Microbuckling instability in elastomeric cellular solids. *Journal of materials science*, 28(17):4667–4672, 1993.

[94] RS Lakes. Extreme damping in compliant composites with a negative-stiffness phase. *Philosophical Magazine Letters*, 81(2):95–100, 2001.

[95] Andrew B Cairns and Andrew L Goodwin. Negative linear compressibility. *Physical Chemistry Chemical Physics*, 17(32):20449–20465, 2015.

[96] Ray H Baughman, Sven Stafström, Changxing Cui, and Socrates O Dantas. Materials with negative compressibilities in one or more dimensions. *Science*, 279(5356):1522–1524, 1998.

[97] RS Lakes. Extreme damping in composite materials with a negative stiffness phase. *Physical review letters*, 86(13):2897, 2001.

[98] Rod Lakes and KW Wojciechowski. Negative compressibility, negative poisson's ratio, and stability. *physica status solidi (b)*, 245(3):545–551, 2008.

[99] Yuan-cheng Fung. *Foundations of solid mechanics*. Prentice Hall, 1965.

[100] DL Barnes, W Miller, Kenneth E Evans, and Arnaud Marmier. Modelling negative linear compressibility in tetragonal beam structures. *Mechanics of Materials*, 46:123–128, 2012.

[101] Andrew L Goodwin, David A Keen, and Matthew G Tucker. Large negative linear compressibility of ag3 [co (cn) 6]. *Proceedings of the National Academy of Sciences*, 105(48):18708–18713, 2008.

[102] A Dominic Fortes, Emmanuelle Suard, and Kevin S Knight. Negative linear compressibility and massive anisotropic thermal expansion in methanol monohydrate. *Science*, 331(6018):742–746, 2011.

[103] Lellis F Braganza and David L Worcester. Structural changes in lipid bilayers and biological membranes caused by hydrostatic pressure. *Biochemistry*, 25(23):7484–7488, 1986.

[104] AM Skvortsov, LI Klushin, and FAM Leermakers. Negative compressibility and nonequivalence of two statistical ensembles in the escape transition of a polymer chain. *The Journal of chemical physics*, 126(2):024905, 2007.

[105] Sarah A Hodgson, Jasper Adamson, Sarah J Hunt, Matthew J Cliffe, Andrew B Cairns, Amber L Thompson, Matthew G Tucker, Nicholas P Funnell, and Andrew L Goodwin. Negative area compressibility in silver (i) tricyanomethanide. *Chemical Communications*, 50(40):5264–5266, 2014.

[106] E As Evans, R Waugh, and L Melnik. Elastic area compressibility modulus of red cell membrane. *Biophysical Journal*, 16(6):585–595, 1976.

[107] Joseph N Grima and Roberto Caruana-Gauci. Mechanical metamaterials: materials that push back. *Nature materials*, 11(7):565–566, 2012.

[108] BD Caddock and KE Evans. Microporous materials with negative poisson's ratios. i. microstructure and mechanical properties. *Journal of Physics D: Applied Physics*, 22(12):1877, 1989.

[109] Carl T Herakovich. Composite laminates with negative through-the-thickness poisson's ratios. *Journal of Composite Materials*, 18(5):447–455, 1984.

[110] F Homand-Etienne and R Houpert. Thermally induced microcracking in granites: characterization and analysis. In *International Journal of Rock Mechanics and Mining Sciences & Geomechanics Abstracts*, volume 26, pages 125–134. Elsevier, 1989.

[111] Amir Yeganeh-Haeri, Donald J Weidner, and John B Parise. Elasticity of or-cristobalitez a silicon dioxide with a negative poissons ratio. *Science*, 257:31, 1992.

[112] KE Evans, MA Nkansah, and IJ Hutchinson. Auxetic foams: modelling negative poisson's ratios. *Acta metallurgica et materialia*, 42(4):1289–1294, 1994.

[113] Ken E Evans. Auxetic polymers: a new range of materials. *Endeavour*, 15(4):170–174, 1991.

[114] Stephen Timoshenko, S Timoshenko, and JN Goodier. *Theory of Elasticity, by S. Timoshenko and JN Goodier,...* McGraw-Hill book Company, 1951.

[115] RS Lakes. Design considerations for materials with negative poisson's ratios. *TRANSACTIONS-AMERICAN SOCIETY OF MECHANICAL ENGINEERS JOURNAL OF MECHANICAL DESIGN*, 115:696–696, 1993.

[116] Roderic Lakes. Advances in negative poisson's ratio materials. *Advanced Materials*, 5(4):293–296, 1993.

[117] KL Alderson and KE Evans. The fabrication of microporous polyethylene having a negative poisson's ratio. *Polymer*, 33(20):4435–4438, 1992.

[118] Ray H Baughman. Auxetic materials: Avoiding the shrink. *Nature*, 425(6959):667–667, 2003.

[119] Roderic S Lakes. *Viscoelastic materials*. Cambridge University Press, 2009.

[120] Ray H Baughman and Douglas S Galvão. Crystalline networks with unusual predicted mechanical and thermal properties. *Nature*, 365(6448):735, 1993.

[121] Lorna J Gibson and Michael F Ashby. *Cellular solids: structure and properties*. Cambridge university press, 1999.

[122] Taeyong Lee and RS Lakes. Anisotropic polyurethane foam with poisson's ratio greater than 1. *Journal of materials science*, 32(9):2397–2401, 1997.

[123] Sachinath Mitra. *High Pressure Geochemistry & Mineral Physics: Basics for Planetology and Geo-Material Science*, volume 9. Elsevier, 2004.

[124] James K Knowles. On saint-venant's principle in the two-dimensional linear theory of elasticity. *Archive for Rational Mechanics and Analysis*, 21(1):1–22, 1966.

[125] MJ Folkes and RGC Arridge. The measurement of shear modulus in highly anisotropic materials: the validity of st. venant's principle. *Journal of Physics D: Applied Physics*, 8(9):1053, 1975.

[126] I Choi and CO Horgan. Saint-venant end effects for plane deformation of sandwich strips. *International Journal of Solids and Structures*, 14(3):187–195, 1978.

[127] CO Horgan. Saint-venant's principle and end effects in anisotropic elasticity. *Journal of Applied Mechanics*, page 425, 1977.

[128] Cornelius O Horgan. Saint-venant end effects in composites. *Journal of Composite Materials*, 16(5):411–422, 1982.

[129] RGC Arridge and MJ Folkes. Effect of sample geometry on the measurement of mechanical properties of anisotropic materials. *Polymer*, 17(6):495–500, 1976.

[130] CO Horgan. Recent developments concerning saint-venant's principle: Second update. *Applied Mechanics Reviews*, 49:S101–S111, 1996.

[131] RS Lakes. Saint-venant end effects for materials with negative poisson's ratios. *TRANSACTIONS-AMERICAN SOCIETY OF MECHANICAL ENGINEERS JOURNAL OF APPLIED MECHANICS*, 59:744–744, 1992.

[132] Eduard G Karpov. Structural metamaterials with saint-venant edge effect reversal. *Acta Materialia*, 123:245–254, 2017.

[133] Norman A Fleck and XinMing Qiu. The damage tolerance of elastic–brittle, two-dimensional isotropic lattices. *Journal of the Mechanics and Physics of Solids*, 55(3):562–588, 2007.

[134] A Srikantha Phani and Norman A Fleck. Elastic boundary layers in two-dimensional isotropic lattices. *Journal of Applied Mechanics*, 75(2):021020, 2008.

[135] V Ivančo. Nonlinear finite element analysis. *University of Applied Sciences–Technology, Business and Design, Wismar*, 2006.

[136] Ursula R Kattner. The thermodynamic modeling of multicomponent phase equilibria. *JOM Journal of the Minerals, Metals and Materials Society*, 49(12):14–19, 1997.

[137] Hans Leo Lukas, Suzana G Fries, and Bo Sundman. *Computational thermodynamics: the Calphad method*, volume 131. Cambridge university press Cambridge, 2007.

[138] Larry Kaufman and Harold Bernstein. *Computer calculation of phase diagrams.* Academic Press, 1970.

[139] Guillermo Bozzolo, Ronald D Noebe, and Phillip B Abel. *Applied computational materials modeling: theory, simulation and experiment.* Springer Science & Business Media, 2007.

[140] Nigel Saunders and A Peter Miodownik. *CALPHAD (calculation of phase diagrams): a comprehensive guide*, volume 1. Elsevier, 1998.

[141] Jan-Olof Andersson, Thomas Helander, Lars Höglund, Pingfang Shi, and Bo Sundman. Thermo-calc & dictra, computational tools for materials science. *Calphad*, 26(2):273–312, 2002.

[142] Corentin Coulais, Dimitrios Sounas, and Andrea Alù. Static non-reciprocity in mechanical metamaterials. *Nature*, 542(7642):461–464, 2017.

[143] Xiaoyu Zheng, Howon Lee, Todd H Weisgraber, Maxim Shusteff, Joshua DeOtte, Eric B Duoss, Joshua D Kuntz, Monika M Biener, Qi Ge, Julie A Jackson, et al. Ultralight, ultrastiff mechanical metamaterials. *Science*, 344(6190):1373–1377, 2014.

[144] James V Carroll and Raman K Mehra. Bifurcation analysis of nonlinear aircraft dynamics. *Journal of Guidance, Control, and Dynamics*, 5(5):529–536, 1982.

[145] S Shankar Sastry. *Nonlinear systems: analysis, stability, and control*, volume 10. Springer Science & Business Media, 2013.

[146] Yunus A Cengel, Robert H Turner, John M Cimbala, and Mehmet Kanoglu. *Fundamentals of thermal-fluid sciences*. McGraw-Hill New York, NY, 2008.

[147] Daphne Attard, Roberto Caruana-Gauci, Ruben Gatt, and Joseph N Grima. Negative linear compressibility from rotating rigid units. *physica status solidi (b)*, 253(7):1410–1418, 2016.

[148] ML Chen and EG Karpov. Bistability and thermal coupling in elastic metamaterials with negative compressibility. *Physical Review E*, 90(3):033201, 2014.

[149] Eduard G Karpov. Bistability, autowaves and dissipative structures in semiconductor fibers with anomalous resistivity properties. *Philosophical Magazine*, 92(10):1300–1316, 2012.

[150] Wei Yang, Zhong-Ming Li, Wei Shi, Bang-Hu Xie, and Ming-Bo Yang. Review on auxetic materials. *Journal of materials science*, 39(10):3269–3279, 2004.

[151] F Scarpa and PJ Tomlin. On the transverse shear modulus of negative poissons ratio honeycomb structures. *Fatigue & Fracture of Engineering Materials & Structures*, 23(8):717–720, 2000.

[152] F Scarpa, LG Ciffo, and JR Yates. Dynamic properties of high structural integrity auxetic open cell foam. *Smart Materials and Structures*, 13(1):49, 2003.

[153] Joseph N Grima, Roberto Caruana-Gauci, Krzysztof W Wojciechowski, and Kenneth E Evans. Smart hexagonal truss systems exhibiting negative compressibility through constrained angle stretching. *Smart Materials and Structures*, 22(8):084015, 2013.

[154] Sicong Shan, Sung H Kang, Zhenhao Zhao, Lichen Fang, and Katia Bertoldi. Design of planar isotropic negative poissons ratio structures. *Extreme Mechanics Letters*, 4:96–102, 2015.

[155] Sicong Shan, Sung H Kang, Jordan R Raney, Pai Wang, Lichen Fang, Francisco Candido, Jennifer A Lewis, and Katia Bertoldi. Multistable architected materials for trapping elastic strain energy. *Advanced Materials*, 27(29):4296–4301, 2015.

[156] Robert Gilmore. *Catastrophe theory for scientists and engineers*. Courier Corporation, 1993.

[157] Peter Timothy Saunders. *An introduction to catastrophe theory*. Cambridge University Press, 1980.

[158] Vladimir I Arnol'd. *Catastrophe theory*. Springer Science & Business Media, 2003.

[159] Steven H Strogatz. *Nonlinear dynamics and chaos: with applications to physics, biology, chemistry, and engineering*. Westview press, 2014.

[160] Costas M Soukoulis and Martin Wegener. Past achievements and future challenges in the development of three-dimensional photonic metamaterials. *Nature Photonics*, 5(9):523–530, 2011.

[161] Zubin Jacob, J-Y Kim, Gururaj V Naik, Alexandra Boltasseva, Evgenii E Narimanov, and Vladimir M Shalaev. Engineering photonic density of states using metamaterials. *Applied Physics B: Lasers and Optics*, 100(1):215–218, 2010.

[162] Harish NS Krishnamoorthy, Zubin Jacob, Evgenii Narimanov, Ilona Kretzschmar, and Vinod M Menon. Topological transitions in metamaterials. *Science*, 336(6078):205–209, 2012.

[163] Vladimir M Shalaev. Optical negative-index metamaterials. *Nature photonics*, 1(1):41–48, 2007.

[164] DR Smith, S Schultz, P Markoš, and CM Soukoulis. Determination of effective permittivity and permeability of metamaterials from reflection and transmission coefficients. *Physical Review B*, 65(19):195104, 2002.

[165] Huanyang Chen and CT Chan. Acoustic cloaking in three dimensions using acoustic metamaterials. *Applied physics letters*, 91(18):183518, 2007.

[166] Ying Wu, Yun Lai, and Zhao-Qing Zhang. Elastic metamaterials with simultaneously negative effective shear modulus and mass density. *Physical Review Letters*, 107(10):105506, 2011.

[167] Graeme W Milton and Andrej V Cherkaev. Which elasticity tensors are realizable? *Journal of engineering materials and technology*, 117(4):483–493, 1995.

[168] Sam Hyeon Lee, Choon Mahn Park, Yong Mun Seo, Zhi Guo Wang, and Chul Koo Kim. Acoustic metamaterial with negative density. *Physics letters A*, 373(48):4464–4469, 2009.

[169] Johan Christensen and F Javier García de Abajo. Anisotropic metamaterials for full control of acoustic waves. *Physical review letters*, 108(12):124301, 2012.

[170] Winston E Kock. Metallic delay lenses. *Bell Labs Technical Journal*, 27(1):58–82, 1948.

[171] John D Busch and Alfred D Johnson. Shape-memory alloy micro-actuator, October 29 1991. US Patent 5,061,914.

[172] Remco Leine and Henk Nijmeijer. *Dynamics and bifurcations of non-smooth mechanical systems*, volume 18. Springer Science & Business Media, 2013.

[173] JMT Thompson. Stability predictions through a succession of folds. *Philosophical Transactions of the Royal Society of London A: Mathematical, Physical and Engineering Sciences*, 292(1386):1–23, 1979.

VITA

John Klein

2610 Walnut Ave. – Evanston, IL – 60201
☎ +1 (847) 345 3770 | ✉ jklein27@uic.edu

Summary

Applying for the PhD program in Materials Engineering at UIC for next semester, Fall 2017. Seeking further specialization in computational research related to materials science and mechanics.

Education

University of Illinois at Chicago — **Chicago, IL**
MS Materials Engineering, 4.00 graduate GPA — *2016–present*
Expected date of master's thesis defense: July 2017

University of Colorado Boulder — **Boulder, CO**
BA Molecular, Cellular and Developmental Biology — *2009–2013*

Research Experience

UIC — **Chicago, IL**
Master's thesis research — *2017*

- Work in Professor Karpov's lab as a computer programmer
- Write code to study the behavior of mechanical metamaterials
- Develop numerical algorithms used in nonlinear analysis and computational mechanics
- Create journal-quality figures and graphs for the visualization of scientific data

Argonne National Laboratory — **Lemont, IL**
Guest Graduate Researcher — *Summer 2016*

- Interned with the Environmental Science Group led by Dr. William L. Ebert
- Electrochemical testing of stainless steels and zirconium alloys
- Interpreted electrochemical impedance spectroscopy (EIS) and potentiodynamic (PD) data

Computer Skills

Matlab: Working knowledge
ANSYS: Working knowledge
Python: Working knowledge
Java: Working knowledge
Fortran: Working knowledge
MS Excel: Working knowledge
LaTeX: Working knowledge
SolidWorks: Working knowledge
HTML, CSS, Javascript: Designed websites

Achievements

- Dean's List for College of Engineering — Fall 2014, Spring 2015, Spring 2016
- Tau Beta Pi Engineering Honors Society — Fall 2015
- UIC Honors College Merit Tuition Award — Spring 2014
- UIC Honors College essay contest winner — Spring 2014
- CU-Boulder Dean's List — Fall 2011, Spring 2012, Fall 2012, Spring 2013
- CU-Boulder Chancellor's Achievement Scholarship — 2009-2013

Interests

- Accomplished pianist and music producer
- Fitness, waterskiing, wakeboarding, snowboarding, tennis, rowing, running, biking and nutrition